Seismic Modelling of the Stratigraphic Architecture of Syn-rift Gilbert Delta Bottomset and Deepwater-fans of the West Xylokastro Fault Block, Corinth Rift

Victoria Gajos Hamre

Department of Earth Science

University of Bergen

June 2022

Abstract

The stratigraphy of rift basins records complex interactions of earth surface processes, palaeoclimate, and tectonics in active margins, and in some regions, hosts important hydrocarbon reservoirs and potential CO_2 storage sites. Nevertheless, coarse-grained syn-rift deep-water depositional systems remain relatively poorly understood and are not well documented in the literature. Detailed characterization of accessible outcropping systems like these is necessary to improve understanding of stratigraphic architecture and depositional processes, which can have direct applications towards estimation of hydrocarbon volumes, reservoir architecture and potential traps in the subsurface systems. This study aims to investigate the seismic expression of deep-water syn-rift depositional systems by generating 2D synthetic seismic images through the 2(3)D point spread function convolution method from two digital outcrop analogues composed of syn-rift Plio-Pleistocene Gilbert-delta bottomset and deep-water fan deposits from the Gulf of Corinth, Greece. The application of 2D seismic modelling of well-constrained outcrop architectures can help constrain the typical seismic signature related to depositional elements of these systems, which can be used to predict possible sub-seismic heterogeneity/ geology.

By interpreting these virtual outcrop models, in combination with previous field observations, down to bed and bed-set scales, realistic geological models are constructed to be used as input for the seismic modelling. The geological models are assigned elastic properties (velocity and density) obtained from well data from an analogous subsurface setting in the Norwegian Sea, The Fenja Field, allowing for seismic modelling with realistic subsurface elastic properties. The results in this study reveal that the seismic expression of the architectural elements appears relatively simplistic in the seismic images, however, the complex heterogeneity of these deposits will generate subtle amplitude variability affecting the resulting seismic. The dominant frequency is the geophysical parameter influencing the resolution of the 2D seismic images the most, where low-resolution seismic (20 Hz) images only the significant changes in dominant lithologies, whilst high-resolution seismic (140 Hz) exposes a higher amount of the internal heterogeneity. The outcome of this study illustrates that the key architectural elements of the deposits within these systems will, in many instances, fall below seismic resolution, hence, a depositional element interpretation would require integration of well-based observations from core or wireline in the subsurface to place confidence on depositional element interpretation.

Acknowledgements

Table of Contents

1 Introduction

1.1 Background and Rationale

The stratigraphy of rift basins record complex interactions of earth surface processes, palaeoclimate, and tectonics in active margins, and in some regions hosts important hydrocarbon reservoirs (e.g., Jones et al., 2021) and potential CO_2 storage sites (e.g., Wu et al., 2021). However, their deep-water depositional system still remains poorly characterized in comparison to those on passive margins or foreland basins (Strachan et al., 2013). These systems are typically smaller and with complex depositional elements which are highly variable in terms of size, geometries, and stratigraphic character (Strachan et al., 2013). Detailed characterization of accessible outcropping systems like these is necessary to improve understanding of stratigraphic architecture and depositional processes, which can have direct applications towards estimation of hydrocarbon volumes, reservoir architecture and potential traps in the subsurface systems (e.g., Bakke et al., 2008; Falivene et al., 2010). Seismic images provide useful data from large areas, but due to resolution limitations, the internal stratigraphic and structural heterogeneity of such systems are in many instances not possible to image (Howell et al., 2014; Manzocchi et al., 2008). Geological outcrops in deep-water syn-rift systems provide useful information on sedimentary architecture to support reservoir modelling and characterization and offer potential 'fill-the-gap' in the subsurface. Hence, the application of 2D seismic modelling of well-constrained outcrop architectures can help understand the seismic signature related to these systems, which can be used to predict possible sub-seismic heterogeneity/ geology (Howell et al., 2014). Coarse-grained syn-rift deep-water depositional systems are generally poorly understood and are not well documented in the literature compared to larger finer-grained systems located in passive margins. This study aims to investigate the seismic expression of deep-water syn-rift depositional systems by generating 2D synthetic seismic images through the 2(3)D point spread function (PSF) convolution method (Lecomte et al., 2015; Lecomte et al., 2016) from two digital outcrop analogues composed of Gilbert-delta bottomset and deep-water fan deposits from the Gulf of Corinth, Greece. The Gulf of Corinth, Greece, is an active rift that originate due to back-arc extension generated by the subduction of the African plate under the Anatolian and European plates (Armijo et al., 1996; Gawthorpe et al., 2018; Papanikolaou and Royden, 2007). The 'Olive Grove' and 'Stomio' outcrop models used in this study are located in the southern flank of the Gulf of Corinth, characterized by uplifted and incised normal fault blocks. The outcrops expose syn-rift deep-water Plio-Pleistocene deposits (Cullen et al., 2020; Gawthorpe et al., 2018; Gobo et al., 2015;

Rohais et al., 2008). The outcrops are situated within the Rethi Dendro Formation (RDF) composed of lacustrine, deep-water stratigraphy, where 'Olive Grove' is composed of proximal bottomset deposits and 'Stomio' model is composed of distal bottomset deposits (Cullen, 2020). The setting of the deposits exposed in these outcrops provides useful analogues to investigate coarse-grained syn-rift deep-water depositional systems.

1.2 Aims and Objectives

The study aims to address the following research questions:

1. What is the seismic signature of coarse-grained deep-water syn-rift deposits in proximal and distal domains, and can difference in their architecture be reliably determined from seismic?

2. Which scales of heterogeneity produce reflectivity within low resolution (e.g., deep or explorations seismic) and high resolution (e.g., shallow/near surface seismic) seismic datasets?

3. Which geophysical parameters have the strongest influence upon the detectability of complex stratigraphy architectures in seismic datasets in deep-water syn-rift systems?

By interpreting these virtual outcrop models, in combination with previous field observations, down to bed and bed-set scales realistic geological models are constructed to be used as input for the seismic modelling. The geomodels are assigned elastic properties (velocity and density) obtained from well data from a similar setting in the Norwegian Sea, i.e., The Fenja Field, which allows for seismic modelling with realistic subsurface elastic properties. The seismic images were generated through the 2(3)D convolution method that allows for investigation of seismic expression of the geological models by changing geophysical parameters and elastic properties.

2 Geological setting

2.1 Regional Tectonic Framework

The Gulf of Corinth is an East-West striking active rift, characterized with a north dipping normal fault system, both onshore and offshore (Figure 2.1) (Ford et al., 2017; Gawthorpe et al., 2018; Leeder et al., 2012; Rohais et al., 2007). The rift originated between the North Anatolian Fault and the Kefalonia fault/ Hellenic subduction zone (Gawthorpe et al., 2018) where subduction of the African plate under the Anatolian and European plates produces NE-SW back-arc extension (Armijo et al., 1996; Papanikolaou and Royden, 2007).

The onset of rifting is radiometrically dated to approximately 5 Ma, in the latest Miocene or early Pleistocene (Gawthorpe et al., 2018). The stratigraphy and evolution of the rifting can be split into two main phases: Phase 1 from 5,0-3,6 Ma to 2,2-2,8 Ma and Phase 2 from 2.2.-1.8 Ma to present (Gawthorpe et al., 2018). Through Phase 1, a 20-30 km-wide network of distributed normal faulting evolved, composing a graben-like structure with tilted, North- and South- dipping, normal fault blocks (Gawthorpe et al., 2018). Several depocenters fed by alluvial and fluvial systems developed into a central Lake-Corinth (Gawthorpe et al., 2018). The transition to Phase 2 marks a 15-30 km northward shift in the locus of rifting, equal to its current location of extension below the Gulf of Corinth (Ford et al., 2017; Gawthorpe et al., 2018). In this phase, giant coarse-grained Gilbert-type deltas built out on the west-central part of the developing southern border normal-fault system (Cullen et al., 2020; Gawthorpe et al., 2018; Muravchik et al., 2020). Lake Corinth was gradually destroyed by tectonic uplift (Gawthorpe et al., 2017; Gawthorpe et al., 2018) whilst the main focus of rifting activity migrated northwards to the area near the present day coastline. Episodic marine connection through both the Corinth Isthmus (east) and Rion Strait (west) has connected the Gulf of Corinth to the Mediterranean, with periodic periods of isolation related to Quaternary eustatic variability (Gawthorpe et al., 2022; McNeill et al., 2019).
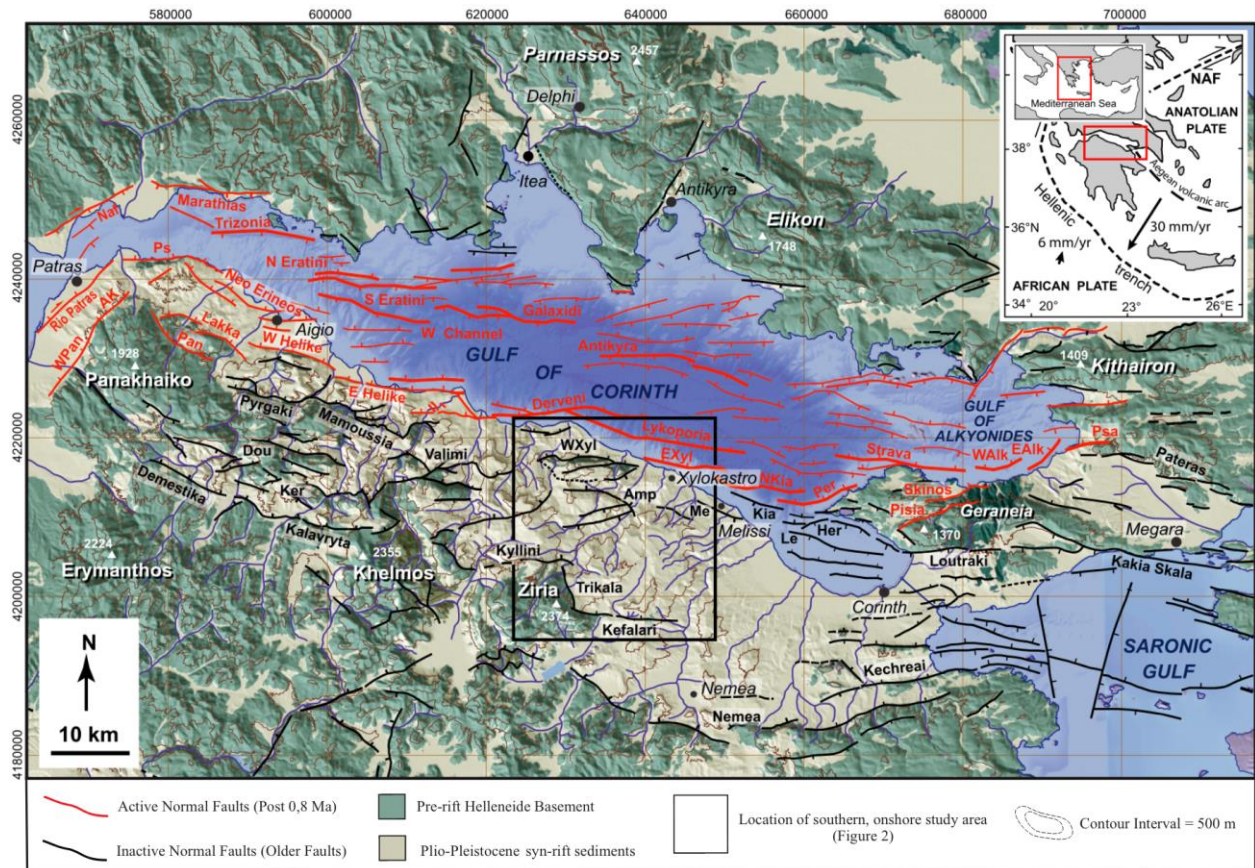
Figure 2. 1: Regional map of the Corinth rift, including general topography and geology. Figure modified from Gawthorpe et al. (2018).

2.2 Study Area

The study area focuses on the southern flank of the Gulf of Corinth, where 5-15 km-wide inactive fault blocks have been uplifted and incised, exposing deltaic and deep-water Plio-Pleistocene syn-rift outcrops (Figure 2.2a, b) (Cullen et al., 2020; Gawthorpe et al., 2018; Gobo et al., 2015; Muravchik et al., 2020; Rubi et al., 2018). The syn-rift succession reaches up to 3 km in thickness (Gawthorpe et al., 2018; Rohais et al., 2007; Rubi et al., 2018).

The outcrop models used in this study, referred to herein as 'Olive Grove' and 'Stomio', are located in the West Xylokastro fault block (WXFB) in the hanging wall of the West Xylokastro Fault (Figure 2.2 b) (Cullen et al., 2020; Gawthorpe et al., 2018). The West Xylokastro fault was primarily active from 1,5 Ma to 0,7 – 0,6 Ma, contemporaneous with the development of the Evrostini and Ilias Gilbert-type fan deltas fed by the Olvios river catchment at the western edge of the West Xylokastro Fault (Cullen et al., 2020; Cullen et al., 2021; Gawthorpe et al., 2018; Gobo et al., 2014; Rohais et al., 2008; Rohais et al., 2007). The deltas have foresets between 200-400 m high indicating progradation in a deep-water body (Lake Corinth) with turbidite channel and lobe complexes of the Rethi-Dendro Formation (RDF) developed

4

basinward of these deltas (Figure 2.3) (Cullen, 2020; Gawthorpe et al., 2018; Muravchik et al., 2020; Rohais et al., 2008). The RDF comprises lacustrine, deep-water stratigraphy in the region of the southern margin to the west of Xylokastro, where the oldest parts (~3,3-1,8 Ma) of the RDF are within the Amphithea Fault Block (Gawthorpe et al., 2018; Muravchik et al., 2020), and the younger parts (~1,8-0,6 Ma) of the RDF are within the WXFB (Cullen et al., 2021; Gawthorpe et al., 2018). Within the WXFB, several exposures of the Rethi-Dendro formation mark a deep-water fan fed by the Ilias delta. The exposures in this thesis focus on proximal bottomset deposits at Olive Grove (Gobo et al., 2015; Rohais et al., 2007; Rubi et al., 2018) and distal bottomset, basin floor deposits at Stomio (Figure 2.3, 2.4) (Cullen et al., 2020).
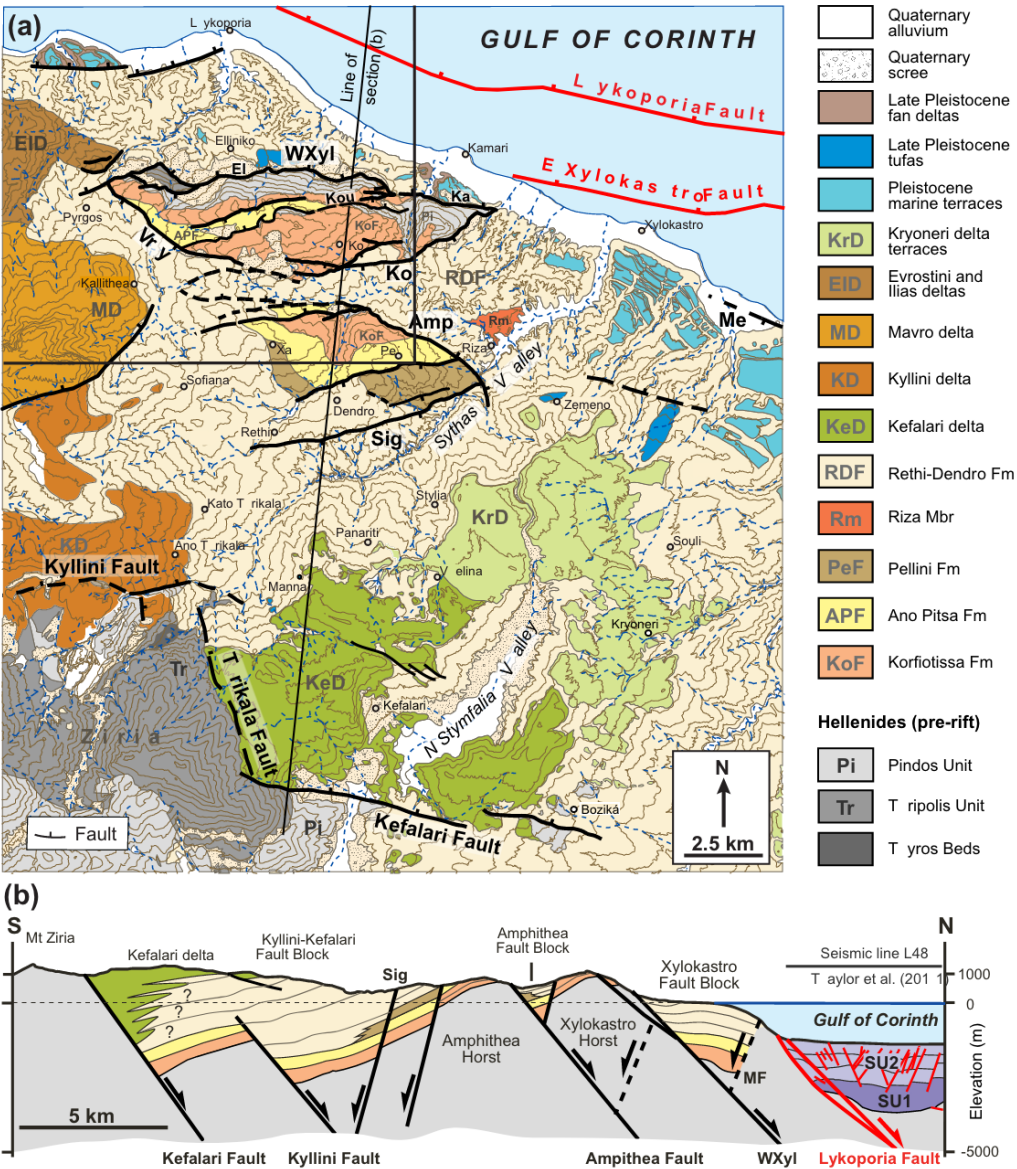
Figure 2. 2: a) Detailed map of the geology in the central Onshore Corinth Rift. Location of relevant stratigraphic and structural elements is marked in upper, left corner (Figure 3). B) Representative cross-section of the uplifted inactive normal faults exposing syn-rift Plio-Pleistoce deposits on the Southern margin of the Gulf of Corinth. Fault abbreviations: Amp = Amphithea fault, Ko = Koutsa fault, Me = Melissi Fault, Sig = Sigeritsa fault, Vry = Vryssoules fault, WXyl = West Xylocastro fault. Figure modified from Gawthorpe et al. (2018).
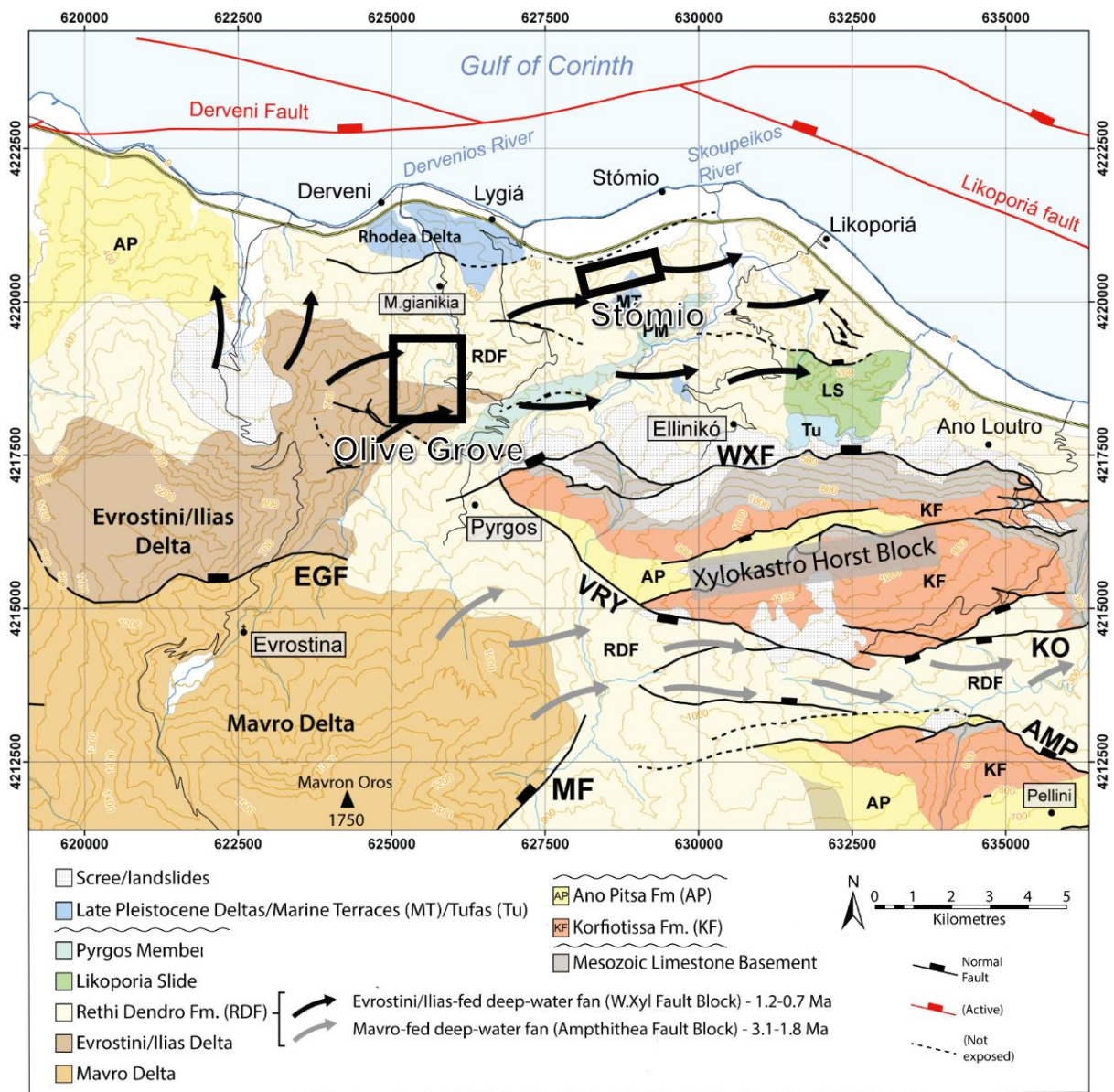
Figure 2. 3: Map of the study area on the southern margin of the Gulf of Corinth. Outcrop models (Olive Grove and Stomio) are marked in relation to the feeding system. Figure modified from Cullen et al. (2020).

The Olive Grove and Stomio outcrops sit within the Rethi Dendro Formation (RDF) (Figure 2.3) (Cullen et al., 2020; Gawthorpe et al., 2018). Cullen et al. (2020) described 10 sub-units of the younger RDF in the WXFB, including the numbered WX1-8 units, the Pyrgos Member, and the Likporià Slide (Figure 2.4). Distal WX1-5 units are present within the Stomio outcrop, and proximal WX5-7 units are present within the Olive Grove outcrop (Figure 2.3, 2.4) (Cullen et al., 2020)
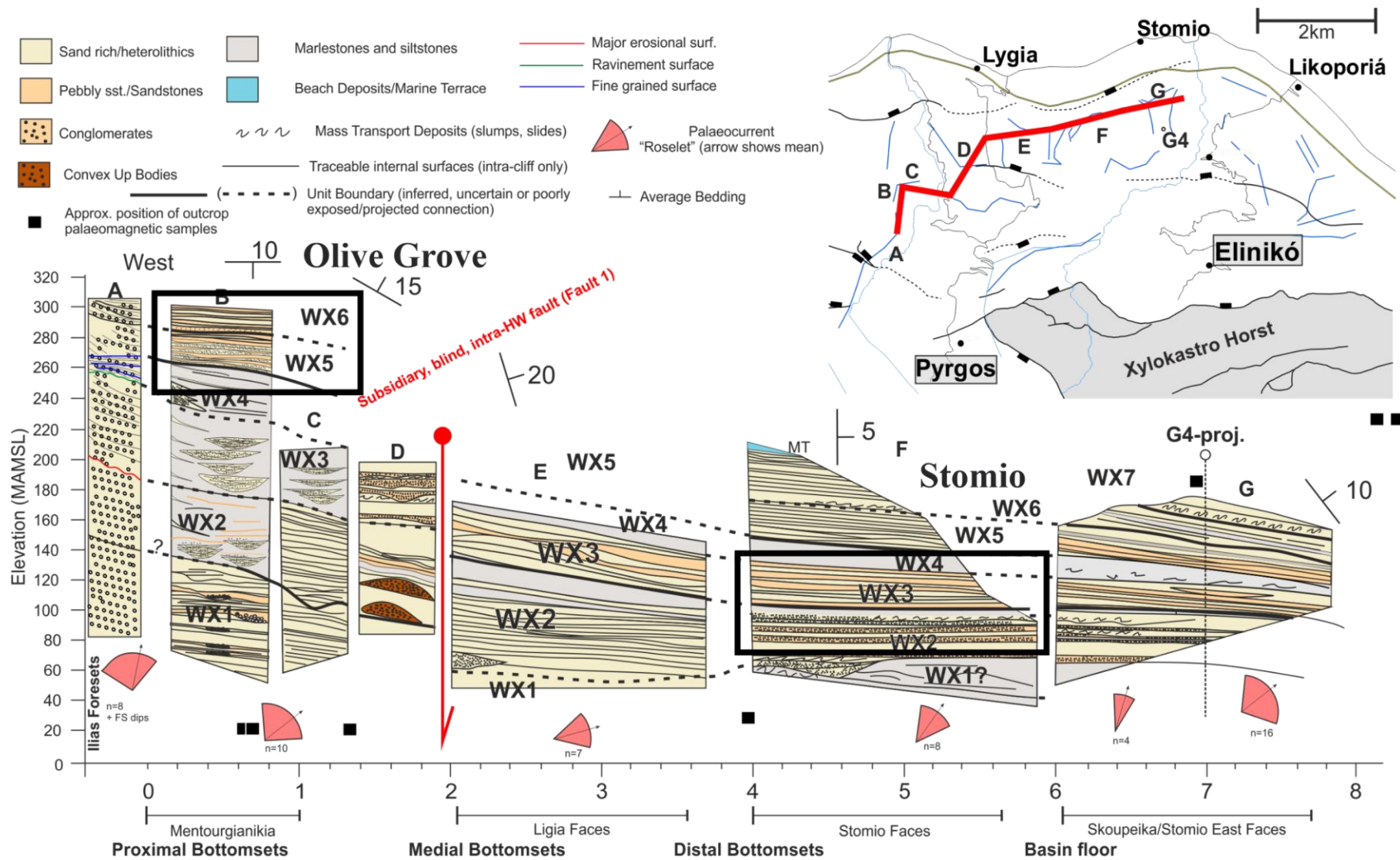
Figure 2. 4: Stratigraphic correlation panel of the Ilias delta, from the distal bottomsets to the basing floor. Both sub-units and outcrop models marked. Figure modified from Cullen et al. (2020).

Distal WX1 deposits comprise marlstones with sheet-like heterolithic deposits or conglomeratic sheets (Cullen et al., 2020). Sheet-like heterolithics are broadly referred to as laterally extensive packages comprising both tabular and non-tabular beds of massive gravel-rich or normal graded coarse to fine sandstones which can also contain some localised conglomeratic or pebbly sandstone beds, interbedded with mudstones (Cullen et al., 2020). The medial parts of WX2 comprise conglomeratic and sand-rich sheets, and sheet-like and complex heterolithics (Cullen et al., 2020). Down-dip of the medial deposits, at Stomio, WX2 is dominated by conglomeratic sheets, with minor sand-rich, but heterolithic intervals and capped by a 5-8 m thick mudstone (Cullen et al., 2020). Conglomeratic sheets fine and thin down-dip in an eastwards direction, but also pinch out up-dip, westwards towards the slope of Ligia (Cullen et al., 2020). WX3 deposits at Stomio comprise a highly variable succession comprising sand-rich sheets and heterolithic deposits interbedded with mudstones and mass transport deposits (Cullen et al., 2020). WX4 is composed of a regionally extensive marlstone-dominated unit that gradually thins eastwards (Cullen et al., 2020). The thicknesses of WX4 is measured ~45-50 m in the immediate bottomset region and ~10 m in the distal bottomset/ basin floor (Cullen et al., 2020). WX5 is a highly variable unit that majorly comprise conglomerate and sand-rich deposits (Cullen et al., 2020). At Stomio and near Skoupeika/ Kalithea, the transition from WX4 to WX5 is marked by a stratigraphic change from mudstone dominated in WX4 to sheet-like heterolithics in WX5 (Cullen et al., 2020). WX4 represents a temporary shut-down of sediment supply to the WXFB (Cullen et al., 2021), and produces a marked change in the architectural style and dominant lithofacies of the stratigraphy. Stratigraphy above WX4 is dominated by sand-rich heterolithics with conglomerates only localised within more channelised parts of the stratigraphy proximal to the fault scarp, rather than the widespread conglomerate deposition which dominate the lower part of the stratigraphy (Cullen et al., 2020; Cullen et al., 2021).

In the proximal exposures at Olive Grove, in the foreset-bottomset transition of the Ilias Delta, WX5 comprise interbedded lens-shaped conglomerates and minor heterolithic, but generally sand-rich intervals (Cullen et al., 2020). The WX5 and WX6 transition is recognized by an erosional surface in the proximal bottomset, increasing the proportion of conglomerates, and changing the architectural style to be dominated by more tabular, massive conglomerates becoming increasingly stratified upwards (Cullen et al., 2020). WX7 is broadly composed of massive conglomerates with a fining- and thinning-upwards trend (Cullen et al., 2020).

3 Deep-Water Processes and Depositional Systems

This chapter summarises literature on deep-water sedimentary processes and their deposits, as well as the morphology and architectural elements of deep-water sedimentary fan systems to provide a background and context to the work carried out in this thesis. This thesis will focus on deep-water processes including gravity flows, mass transport processes and hemipelagic/ hemilimnic fall-out. To simplify, gravity flows will be used as a collective term for turbidity currents and debris flows, and mass transport processes will be used as a collective term for slumps and slides.

Classification of Gravity Flows

The classification of gravity flows is a matter of contentious discussion in the literature and has produced various classification schemes based on characteristics such as flow state, dominant sediment support mechanism, flow rheology, often interpreted from deposits (Talling et al., 2012). This thesis uses the deposit-based classification scheme derived by Talling et al. (2012) as a basis (Figure 3.1 and 3.2) since the available data to be reviewed are deposits preserved in outcrops. The Talling et al. (2012) classification distinguishes broadly between flow types where deposition is interpreted to occur incrementally (turbidity currents) or in a quasi-instantaneous deposition of the flow *en masse* (debris flow). A sedimentary deposit will record the near-bed sedimentation processes as sediments settle out from the flow (Talling et al., 2012). However, the characteristics of a flow can be hard to interpret from deposits due to the complexity associated with gravity flows, as well as the impact of post-depositional consolidation and soft-sediment deformation (Mulder and Alexander, 2001)

Flow type terminology		Sediment support mechanism (s)
DEBRIS AVALANCHE	Debris avalanche deposit	Particle collisions; Matrix strength
SLUMP OR SLIDE	Slump or slide deposit	Matrix strength, Excess pore pressure
GRANULAR AVALANCHE	Grain-flow deposit	Particle collisions

SUBAQUEOUS SEDIMENT DENSITY FLOW — SUBAQUEOUS SEDIMENT DENSITY FLOW DEPOSIT OR DENSITE

DEBRIS FLOW / DEBRITE — EN-MASSE CONSOLIDATION (AND ABRUPT FREEZING) — LAMINAR (OR ALMOST LAMINAR)

NON-COHESIVE — NON-COHESIVE DEBRIS FLOW (*Very clean sand debrite*)	D_{VCS}	Mainly excess pore pressure such that flow is fully or partly liquefied. No cohesive strength but margins can freeze as pore pressure dissipates
POORLY COHESIVE — POORLY COHESIVE DEBRIS FLOW (*Clean sand debrite*)	D_{CS}	Cohesive strength allows sand to partly or fully settle out (sometimes very slowly). Excess pore pressure, bouyancy and grain to grain interaction help to support sand
COHESIVE DEBRIS FLOW — HIGH STRENGTH (*High strength muddy debrite*)	D_{M-2}	
MODERATE STRENGTH (*Moderate strength muddy debrite*)		Cohesive strength of matrix is enough to prevent sand settling, but support can also occur by excess pore pressure, buoyancy (clast verses matrix density), and grain to grain interactions.
LOW STRENGTH (*Low strength muddy debrite*)	D_{M-1}	

TURBIDITY CURRENT / TURBIDITE — SIZE-SEGREGATING SETTLING AND LAYER-BY-LAYER DEPOSITION — Damped Turbulent / TURBULENT

HIGH DENSITY (SANDY) TURBIDITY CURRENT (*High density turbidite*)	T_{B-3} T_{A} T_{B-2}	Turbulence damped and settling of grains hindered. Grain support via combination of damped turbulence, grain to grain interactions, and to a lesser extent excess pore pressure. Grains can be reworked in denser near bed traction carpet.
LOW DENSITY (SANDY) TURBIDITY CURRENT (*Low density turbidite*)	T_{B-1} T_{C} T_{D}	Fluid turbulence (with grains reworked as bedload)
MUD DENSITY FLOW (*Densite mud*)	T_{E-1} T_{E-2}	Fluid turbulence
	T_{E-3}	Matrix (gel) strength (and excess pore pressure)

DEBRIS FLOW | *EN MASSE* CONSOLIDATION (AND ABRUPT FREEZING) | LAMINAR (OR ALMOST LAMINAR)

Figure 3. 1: Table summarizing terminology used in Talling et al (2012)'s deposit-based classification scheme for subaqueous density flows (referred to as gravity flows in this thesis). Figure modified from Talling et al. (2012)
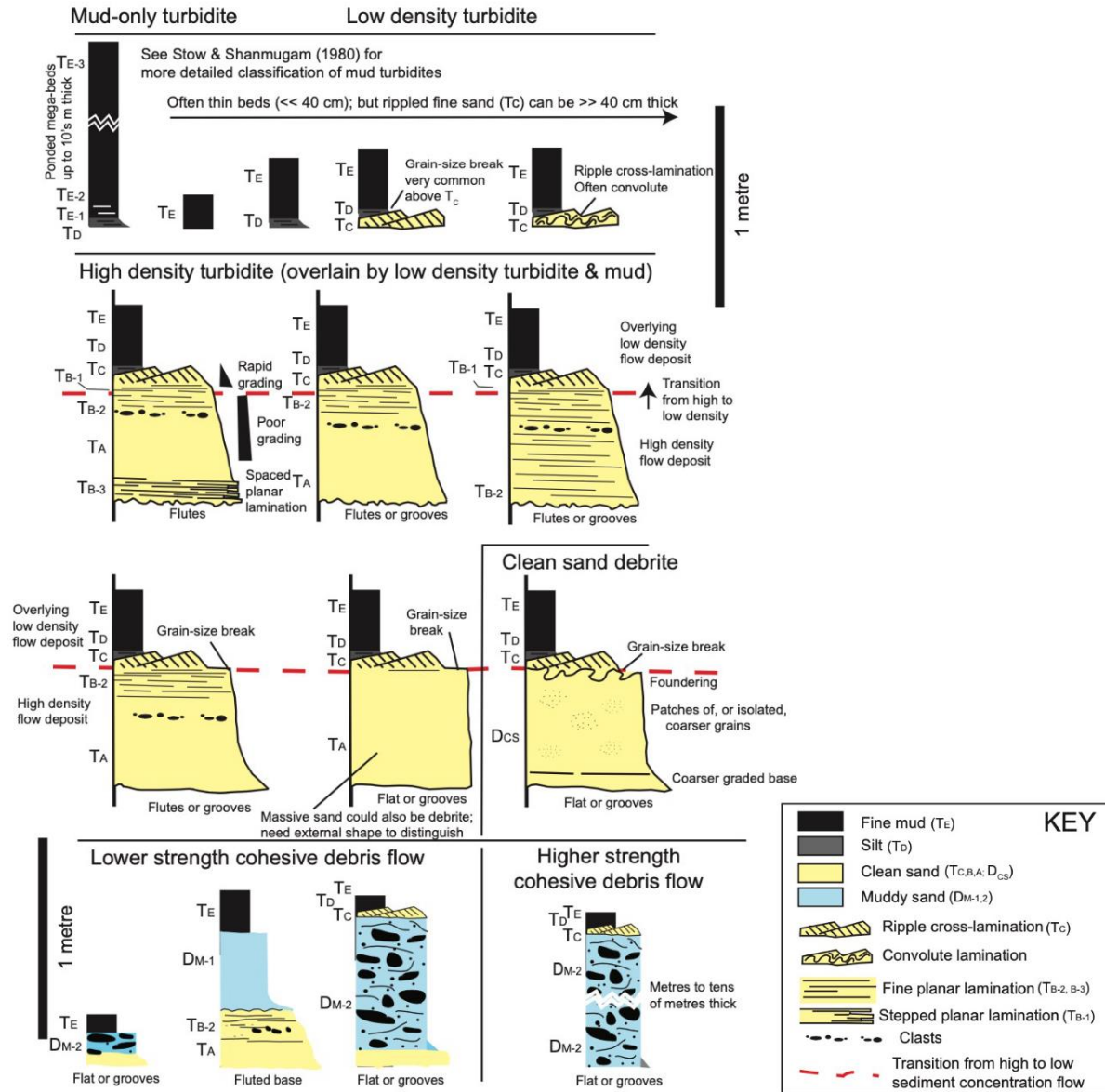
Figure 3. 2: Overview of sedimentary characteristics from different gravity flows in the Talling et al. (2012) classification. Figure from Talling et al. (2012).

3.1 Sedimentary Processes and Deposits

Gravity flows are key sedimentary processes operative on all slopes transferring vast amounts of sediments to deep-water basins (Haughton et al., 2009; Henstra et al., 2016; Lowe, 1982; Nemec, 1990; Talling et al., 2012). Both gravity flows and mass transport processes are generated directly by the force of gravity acting upon the excess mass of a sediment-laden flow (Boggs, 2014). A range of sediment gravity movements exists, ranging from coherent, *en masse* transports through to increasingly fluidal flows (Figure 3.3). Under some conditions a single flow event can involve several flow types, as one type can transform into another downslope both towards increasingly fluidal flows (Felix and Peakall, 2006; Henstra et al., 2016; Strachan, 2008) or increasingly cohesive flows (Baas et al., 2009; Haughton et al., 2009; Kane et al., 2017; Patacci et al., 2014; Talling et al., 2012).
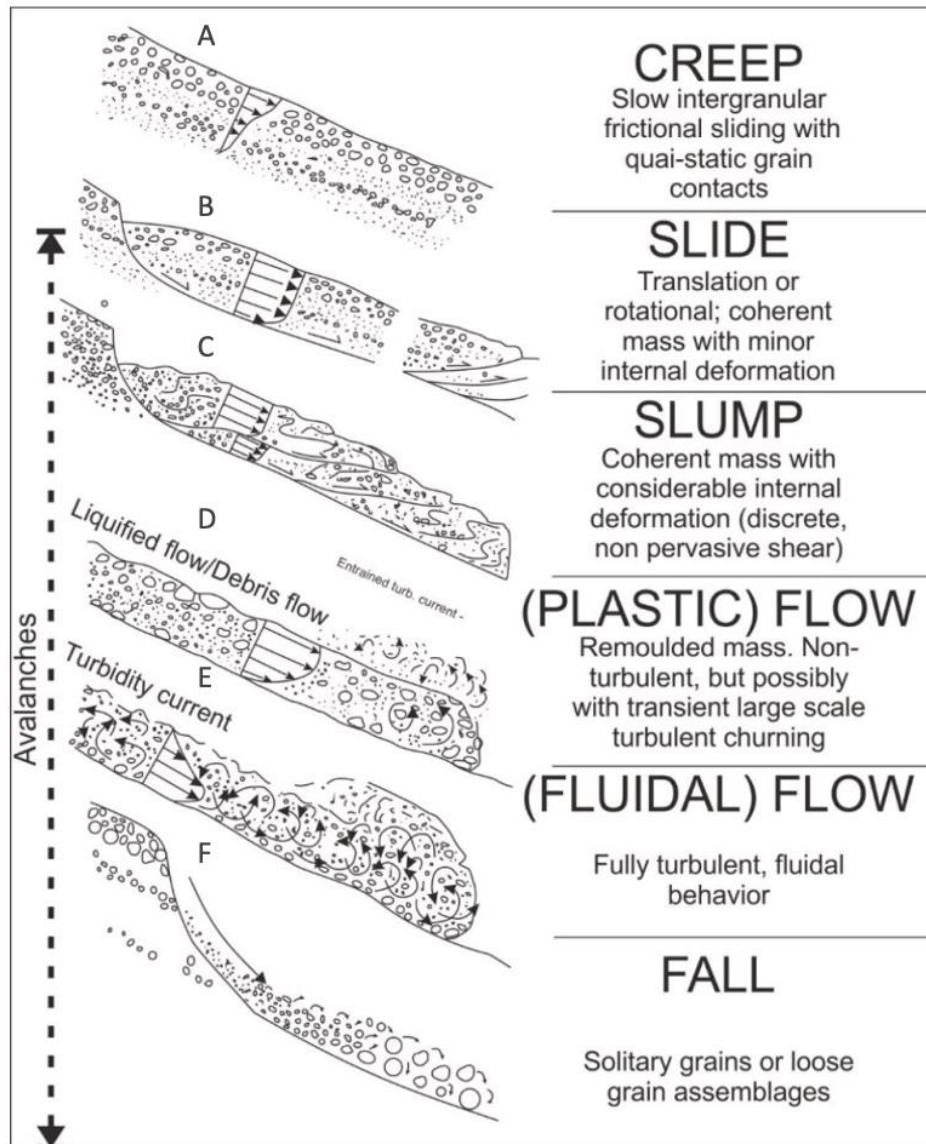
Figure 3. 3: Illustration of sediment gravity driven processes. Figure modified from Nemec (1990).

Turbidity Currents

Mulder & Alexander (2001) defined a turbidity current as "a current which fluid turbulence is the main particle transport mechanism, although other mechanisms may also operate to varying degrees" (Figure 3.3E). However, Talling et al. (2012) highlight that distinguishing deposits on the basis of sediment support mechanism is challenging as deposits seldom record the dominant *transport* mechanism. Instead Talling et al. (2012) described depositional processes of turbidity currents as incremental where larger grains preferentially settle in a layer-by-layer fashion. Deposits from turbidity currents are commonly referred to as turbidites characterized with laminated and graded to massive and ungraded mudstones, ripple cross-laminated to planar laminated siltstones and fine sandstones, and planar laminated to massive sandstones (Figure 3.4) (Bouma, 1962; Talling et al., 2012). Within this, turbidity currents exist across a range of sediment concentrations, leading to the sub-classification of low- and high-density turbidity currents (Henstra et al., 2016; Lowe, 1982; Talling et al., 2012). Low-density turbidity currents (LDTs) are characterized as fully turbulent flows containing less than 20-30 percent grains (Boggs, 2014; Lowe, 1982; Mulder and Alexander, 2001; Talling et al., 2012). Whilst interpreting sediment concentration from deposits of flows is problematic, low-density turbidity currents are typically considered to be composed mainly of clay to medium sand-sized particles supported in suspension by turbulent eddies within the flow, and deposited incrementally out of suspension as the flow (and turbulence) decelerates (Boggs, 2014; Kneller and Branney, 1995; Talling et al., 2012). High-density turbidity currents (HDTs) contain greater concentrations of grains and may include coarser particles (coarse sand grains to cobble-sized clasts) than low-density turbidity currents (Boggs, 2014; Lowe, 1982), which leads to hindered settling of particles near the bed of the flow or the generation of traction-carpets within highly concentrated basal layers (Lowe, 1982; Postma et al., 1988; Sohn, 2000). The various mechanisms supporting sediments in high-density currents includes fluid turbulence, grain to grain interactions, and a limited density contrast between grains and contiguous water (Talling et al., 2012). In general, LDTs deposit fine-grained, thin-bedded turbidite successions and high-density currents deposit coarse-grained, often gravelly, thick-bedded turbidite successions (Figure 3.5) (Boggs, 2014; Henstra et al., 2016).
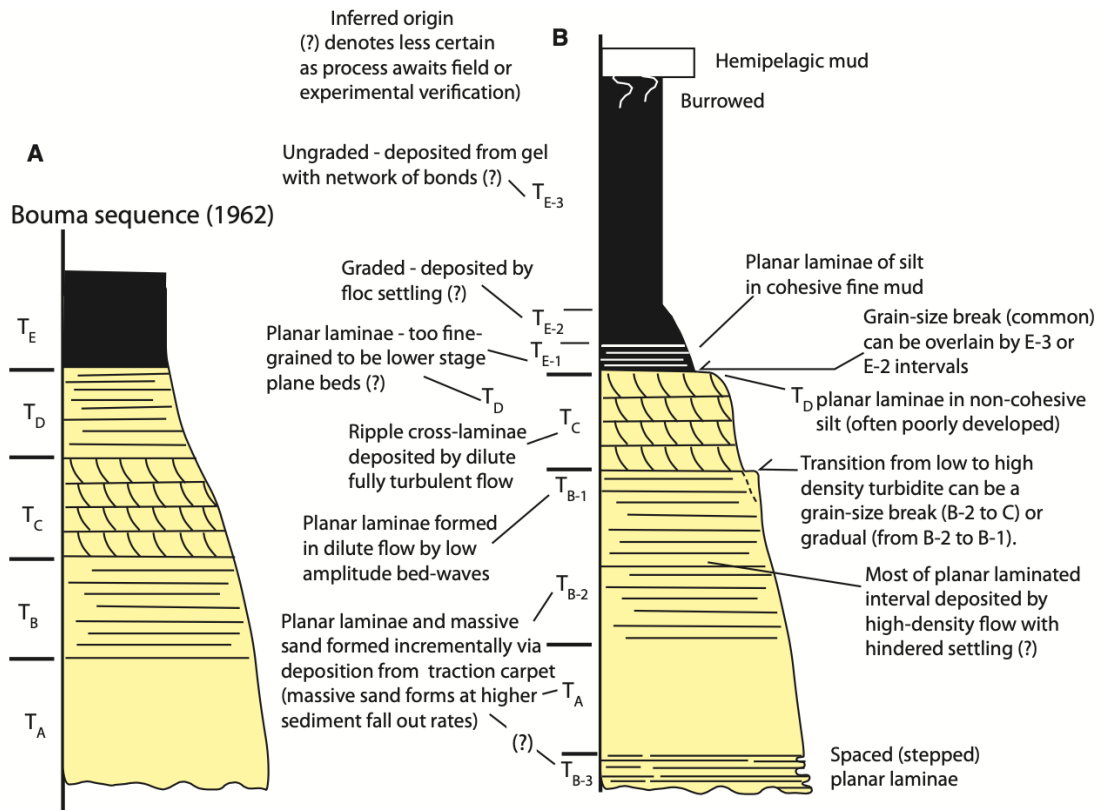
Figure 3. 4: Schematic presentation of the classic Bouma Sequence (A) and the reviewed turbidite sequence from Talling et al. (2012) (B). Figure from Talling et al. (2012).
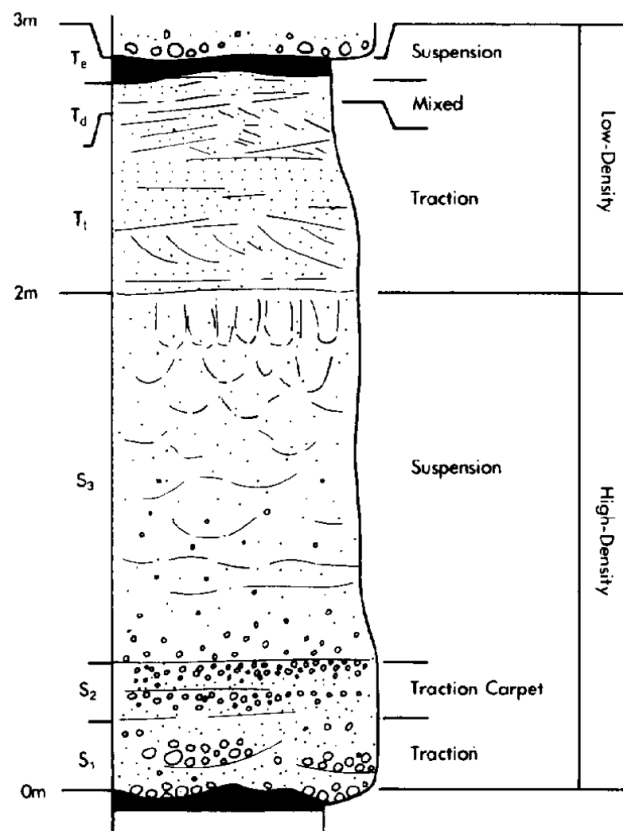
Figure 3. 5: Illustration of an ideal depositional sequence from a high-density turbidity current ($S_1 - S_3$) and a succeeding low-density turbidity current (T_t, T_d, and T_d). Figure from (Lowe, 1982).

Debris Flows

Debris flows are generally characterised as flows with Bingham-plastic behaviour meaning that the flow has cohesion, and an associated yield strength behaviour (Figure 3.3D) (Iverson, 1997; Nemec, 1990; Shanmugam, 2016; Talling et al., 2012). If the stress within the flow exceeds that yield strength, the flow will move, and if the stress is below the yield strength the flow will cease movement, and deposit (Talling et al., 2012). The primary process for debris-flow deposition is a quasi-instantaneous freezing or *en masse* deposition of the flow or parts of the flow (Major and Iverson, 1999; Mulder and Alexander, 2001; Talling et al., 2012). Debris flow deposits, often referred to as debrites, are as a result generally chaotic and poorly sorted with particle-sizes ranging from clay to boulders (Iverson, 1997; Major and Iverson, 1999; Nemec, 1990; Talling et al., 2012). Debrites often contain outsized clasts supported by the surrounding matrix where grading of clasts may be highly variable and can occur dependent on the relative density between clasts and the surrounding matrix or through kinetic sieving depending on interactions with pore-fluid pressure, remobilisation of flows and post-depositional alteration (Major and Iverson, 1999; Talling et al., 2012). The Talling et al. (2012) classification subdivides debris flows based on their cohesive mud concentrations into cohesive debris flows (mudflows), poorly cohesive debris flows and non-cohesive debris flows (Figure 3.2). Unlike turbidity currents, cohesive debris flows can show entirely laminar flow state, especially when clay rich (Baas et al., 2009; Talling et al., 2012) however most debris flows are highly heterogenous in terms of transport and depositional process (Major and Iverson, 1999). With increasing clast concentration, lower clay-content or ambient water entrainment, debris flows can become increasingly turbulent and have substantially lower or absent cohesion (Lowe, 1982). Heterogeneity of clay-content in time and space may allow debris flows to transform into turbidity currents if their strength is lowered by increasing fluid content (Amy et al., 2005; Strachan, 2008).

Mass Transport Processes (Slides and Slumps)

A slide refers to a coherent mass of sediment or rigid body that moves along a typically planar glide plane with limited internal deformation" (Figure 3.3B). Meanwhile slumps, whilst still largely coherent mass of sediment, can undergo substantial internal deformation (Figure 3.4C) (Bull et al., 2009; Nemec, 1990; Posamentier et al., 2011; Postma, 1984; Strachan, 2008). A single mass movement, and resulting mass-transport deposit, can have substantial internal heterogeneity of processes resulting from variability of sediment concentration and type, slope, and post-depositional alteration (Posamentier et al., 2011).

Debris Falls

Subaqueous Debris falls are initiated by slope-failures, characterized as dispersed single particles or particle assemblages (masses) avalanching down-slope (Figure 3.3F) (Nemec, 1990). The particles commonly bounce, slide, and roll during transportation where larger clasts usually travels faster and for a longer distance due to the pull of gravitational forces (Nemec, 1990). As a result, debris fall deposits show an increase in clast size downslope, and where several debris fall deposits are stacked on top of each other they tend to 'backlap' and display overall coarsening upwards trends (Nemec, 1990). In coarse-grained systems these can commonly be presented as matrix-poor or open-framework conglomerates with little in the way of imbrication or structuring (Gobo et al., 2015; Nemec, 1990).

Hemipelagic (or Hemilimnic) Fall-Out

Hemipelagic and pelagic fall-out, sometimes referred to as hemilimnic fall out in lacustrine settings (e.g., Dodd et al., 2019) is generally defined as settling of typically fine-grained material derived from continents and biogenic remains suspended in the water column onto the deep-ocean floor (Boulesteix et al., 2019; Stow and Smillie, 2020). Deposition of hemipelagic mud occurs under very low current velocities, such by suspension settling or drifting (Boggs, 2014) and in that sense true hemipelagites may be fairly rare, with most interpreted 'hemipelagite muds' largely being the product of very thin sediment-laden flows from remobilised mudstone (Boulesteix et al., 2019). Hemipelagic mud deposits are poorly laminated to massive where textures range from clay to silty, sandy clay and may show monospecific and limited bioturbation (Boggs, 2014; Boulesteix et al., 2019). However, the distinction between hemipelagic mud, turbidite mud and muddy debrites is hard to distinguish from each other visually/ in field where poorer outcrop preservation often obscures small (mm and sub-mm) scale structures (grain-size trends or changes in bioturbation intensity) needed to distinguish this (Boulesteix et al., 2019).

3.2 Sedimentary systems, geomorphology, and architecture

Deep-water depositional systems are complex and difficult to study, making them resistant to successful classification and modelling (Reading and Richards, 1994). Compared to more accessible depositional systems (e.g., fluvial, and deltaic) the relation between modern, active, sedimentary environments, sedimentary processes and resultant facies in deep-water depositional systems has been demanding to establish (Reading and Richards, 1994). Reading and Richards (1994) assigned deep-water depositional systems into 12 distinct classes including submarine fans, submarine ramps, and submarine aprons, further subdivided based on mud-, sand- and gravel- content (Figure 3.6). The Gulf of Corinth commonly hosts gravel-rich submarine fans common within short, steep systems on active margins (Cullen et al., 2020; Gawthorpe et al., 2018; Muravchik et al., 2020; Reading and Richards, 1994; Rohais et al., 2008; Strachan et al., 2013).
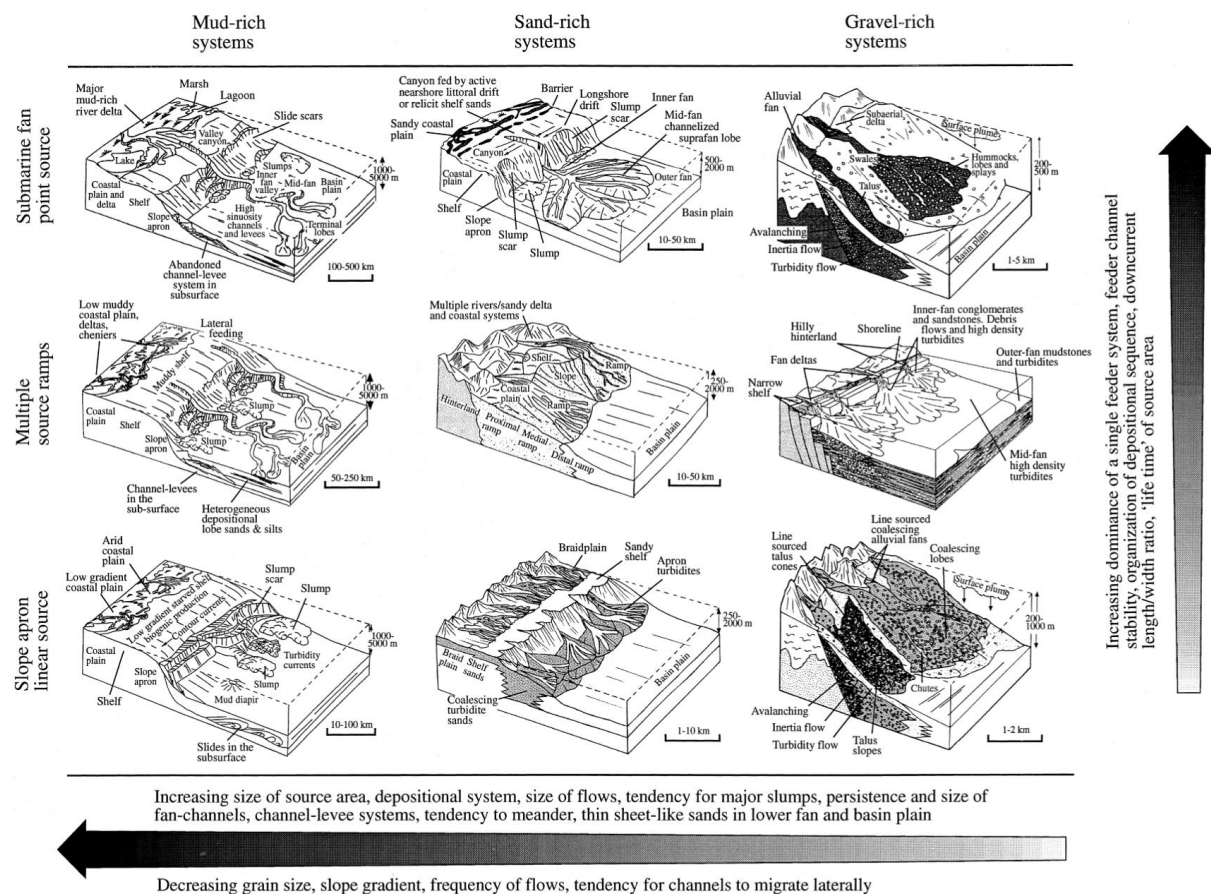
Figure 3. 6: Reading and Richard (1994)'s environmental endmember models based on sediment composition (volume and graind size) and number of feeder channels in the supply system. Figure from Stow & Mayall (2000).

Considering deep-marine clastic environments, submarine fans compose important clastic accumulations and represent the sediment-routing system between the source area (hinterland) and the depositional sink (deep-sea) (Garcia et al., 2015; Garland et al., 1999; Walker, 1978) (Garland et al., 1999; Walker, 1978). The principal geomorphic elements of submarine fan systems are large-scale canyons, channels and levees, and lobes (Figure 3.7) (Mulder, 2011; Reading and Richards, 1994). All these geomorphic features exist along a continuum, with complex transition zones existing between them producing some overlap in their architecture, depositional processes and distribution (Cullis et al., 2018). This section details their morphology, stratigraphic architecture, and primary facies, which is summarised in Table 3.1.
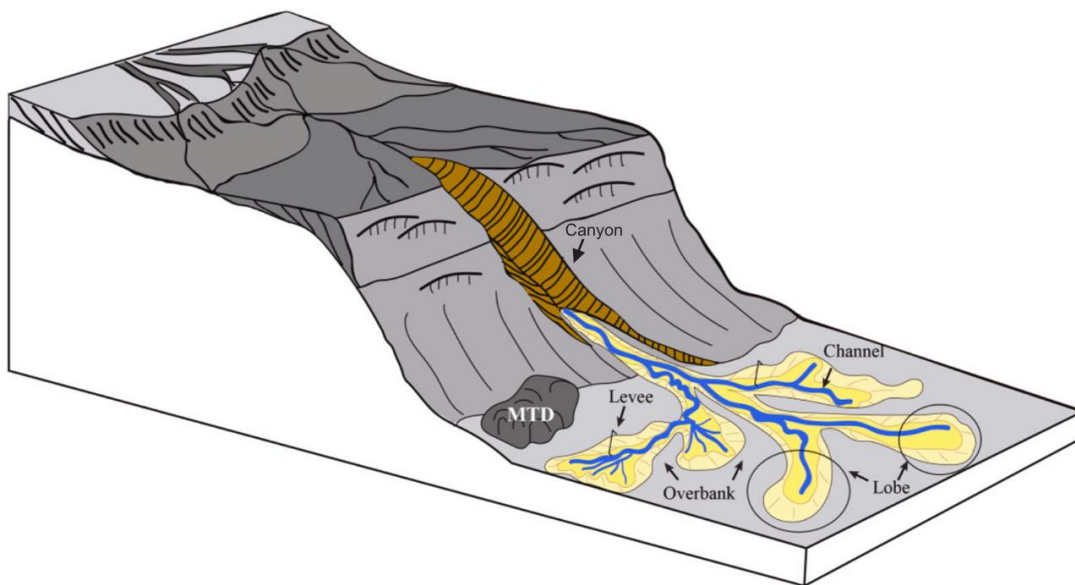
Figure 3. 7: Simplified model of a submarine fan model highlighting the main composition elements. MTD = mass transport deposit. Figure modified from Cicconeto et al. (2022) (modified in paper from Posamentier and Walker (2006)).

Canyons

Continental shelves and slopes are incised by submarine canyons oriented approximately perpendicular to the shelf break, which provide the main conduits for sediment transport from the shallow to deep-marine realm (Harris and Whiteway, 2011; Mulder, 2011; Piper and Normark, 2009). They are characterized as steep-sided valleys, generally with a v-shaped (in some instances u-shaped) cross-sectional profile and are typically narrow (a few km) and deep (hundreds of metres) with a length largely controlled by the geomorphology of the broader slope or margin (Harris and Whiteway, 2011; Mulder, 2011; Soutter et al., 2021).

Canyons are dominated by erosive processes during their formation (Garcia et al., 2015; Maier et al., 2018; Piper and Normark, 2009). As a result, their deposits are often complex due to repeated periods of erosion and sedimentation (Di Celma et al., 2013; Hodgson et al., 2011; Mutti et al., 1985; Weimer and Link, 1991). Canyon-fills can be composed of a variety of deposits, but are generally dominated by a thick package of turbidite fills comprising scoured conglomerates and pebbly sandstones in basal parts, and commonly overlain by a mixture of mud-prone stratigraphy recording complex backfilling and degradation (Jackson et al., 2021; Mutti et al., 1985; Weimer and Link, 1991). Canyons can be recognized by their erosive, but composite, master basal surfaces in seismic producing noticeable unconformities against surrounding stratigraphy (Figure 3.8A) (Shanmugam and Moiola, 1988; Tillmans et al., 2021).
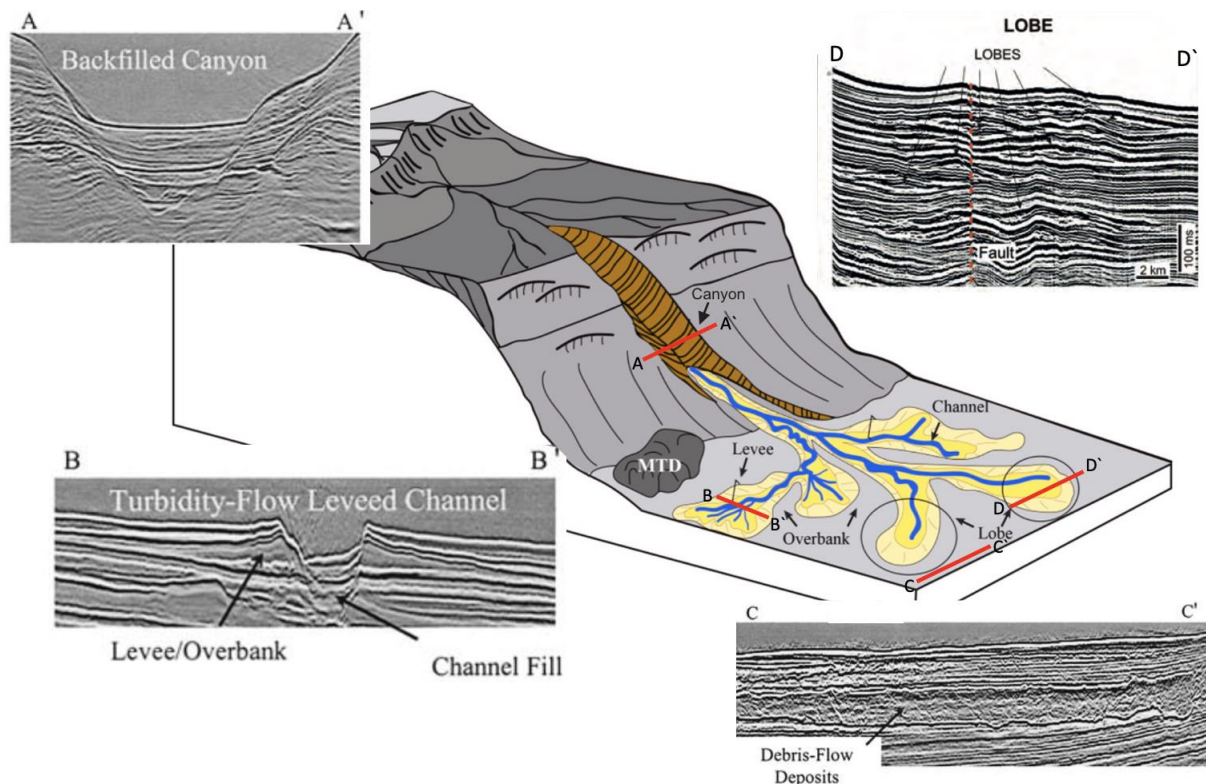
Figure 3. 8: Examples of how compositional elements of submarine fans can look like in seismic. Submarine fan figure modified from Cicconeto et al. (2022), seismic images of canyon, turbidity-flow leveed channel and debris-flow deposits form Posamentier & Kolla. (2003), and seismic image of lobes from Garcia et al. (2015).

Channels and Channel-Levee Systems

Submarine channels develop in the mouths of canyons typically with decreasing widths and depths basinwards (Hodgson et al., 2011; Shanmugam, 2016). Channels are elongated bodies with generally concave-up cross-sections (Galloway, 1998). The morphology of deep-water channels is controlled by erosion and deposition by gravity flows and mass transport (Hodgson

et al., 2011; Mulder, 2011) and is increasingly recognised as the progressive aggregation of up-stream migrating knickpoints combined with catastrophic mass-wasting events (e.g., Tek et al., 2021). Erosional (incised) channels are typically deep with poorly developed levee-systems located on the steepest part of the slope, while depositional (constructional or aggradational) channels are located on the lower slope where both the channel-floor and levees aggrades simultaneously (Galloway, 1998; Mulder, 2011). Dimensions are highly variable ranging from hundreds to thousands of metres in width, tens to more than a hundred metres in depth and several to hundreds of km in length (Galloway, 1998) with their geometry commonly controlled through the interaction of basin topography and sediment supply (Hodgson et al., 2016). Through progressive episodes of erosion and depositional channels stack to form distinct depositional elements which can be considered through a hierarchical arrangement (Figure 3.9) (Cullis et al., 2018; Sprague et al., 2005).
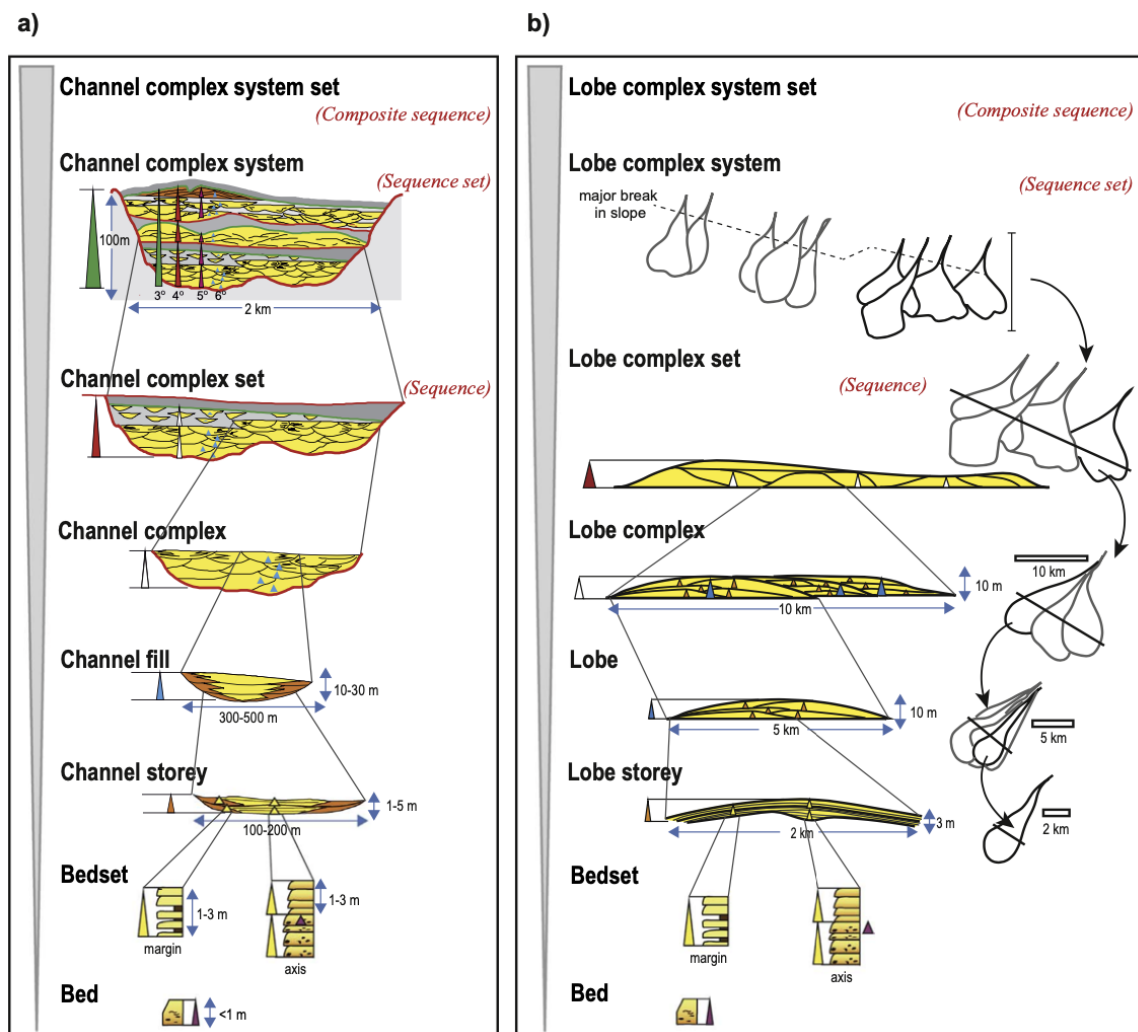
Figure 3. 9: Illustration of Sprague et al (2005)'s hierarchical scheme encompassing both channelized and lobate forms. Figure from (Cullis et al., 2018).

Channel-fill deposits can be highly variable (Figure 3.10) and are usually composed of massive to amalgamated sandy and conglomeratic turbidites (Galloway, 1998; Shanmugam and Moiola, 1988) bounded by an erosional surface at the base (Weimer and Link, 1991). In mud-dominated systems channel-fill deposits are usually composed of muddy turbidites and slump debris (Galloway, 1998). Channel-fill deposits can reflect cycles of overall fining upward gran-size trends and thinning upward bed thickness trends (Shanmugam and Moiola, 1988). Deposits of channels can be diverse due to other depositional processes operating in channels, including debris flows, mass transport processes, and hemipelagic fall-out (Shanmugam and Moiola, 1988). Debris flow channel-fill deposits are generally less sinuous than leveed turbidity-flow channels, commonly forming on short, steep margins (Posamentier and Kolla, 2003), however sinuous channels also can host substantial debris flows (e.g., Tek et al., 2021). Sediment bypass in channels can be recorded in mainly two features: residual facies from gravity flows and channel-margin thin-bedded facies indicating hindered deposition compared to thick amalgamated sandstone beds (Stevenson et al., 2015; Weimer and Link, 1991).

In seismic, channels usually have a discontinuous high-amplitude seismic reflection at the base due to incision into the underlying substrate of the basal floor (Figure 3.8B) (Posamentier and Kolla, 2003; Weimer and Link, 1991). Turbidity-flow channel-leveed elements deposited by flows with sufficient coarse-sediment loads are commonly characterized with lateral HARs (Mulder, 2011; Posamentier and Kolla, 2003). Debris flow channel-fill deposits are associated with chaotic to transparent seismic facies with grooved basal surfaces (Figure 3.8C) (Posamentier and Kolla, 2003).

Cullis et al. (2019) defined a levee as "*an aggradational sediment wedge found adjacent to a genetically related channel. The overbank elements forms as sediment-laden flows over-spill confined sediment pathways*". In general, the height of levees along a channel decreases basinwards from a few hundreds of metres upstream to several tens of metres downstream (Mulder, 2011). The characteristics of the channel and flows within them ultimately influences the heights and character of the levees, e.g., levees can be completely absent in strongly erosive systems (Posamentier and Kolla, 2003) or have complex wavefields where flows regularly exceed the channel depth with exceptionally high sedimentation rates producing large, extensive levees up to 50 km wide (Mulder, 2011; Tek et al., 2022). Deposits on levees are commonly characterised by fine-grained sandstone and mudstone turbidite elements (Kane et al., 2007; Weimer and Link, 1991). Turbidity currents progressively spill over the finer particles

downstream, resulting in thinner, coarser grained levee-deposits longitudinally (Mulder, 2011). In seismic by their "bird-wing" shape with internal reflectors pinching out (downlap) on the outer levee sides (Mulder, 2011). Their amplitudes are low to moderate and reflectors are continuous to discontinuous, occasionally, they can be completely transparent (Posamentier and Kolla, 2003).
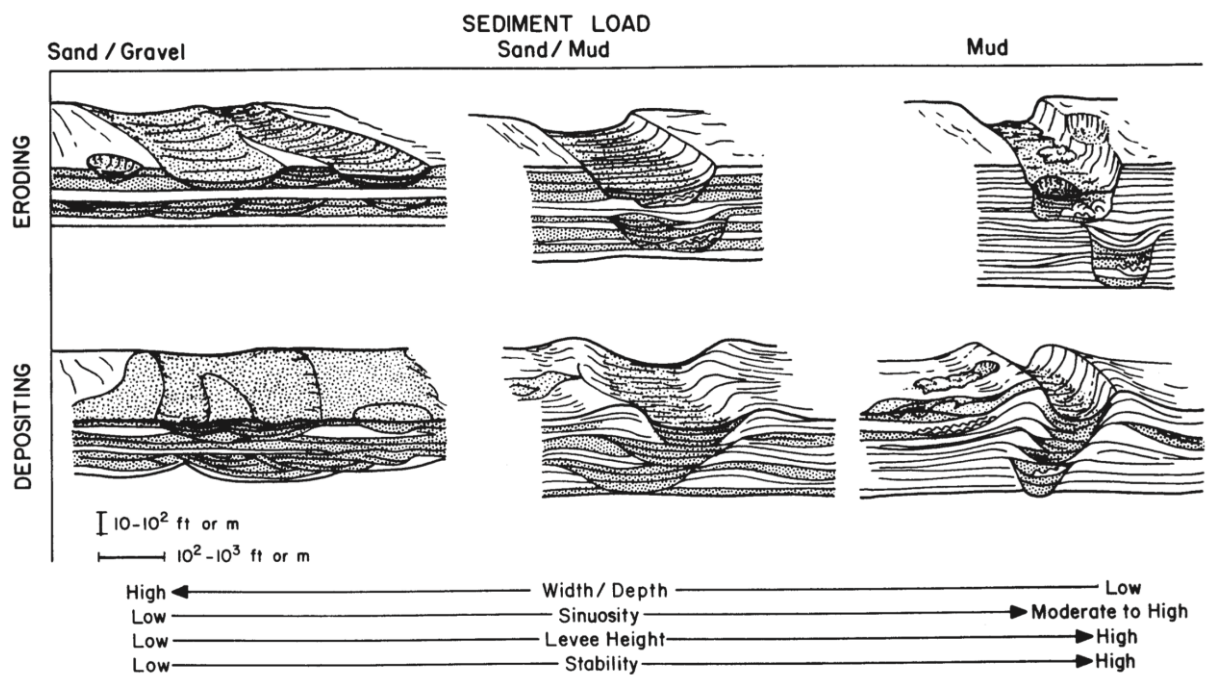
Figure 3. 10: Spectrum of depositional geometries of erosional and depositional channels dependent on grain sizes, correlated with relevant dimensions. Figure from Galloway (1998).

Fans and Lobes

Posamentier and Walker (2006) defined a lobe as "a sedimentary body having a lobate shape in plan-view and a lens-shaped cross-section, found at the lateral terminus of a channel" (Cicconeto et al., 2022; Posamentier and Walker, 2006; McHargue et al., 2021). Lobes are mainly dominated by net-depositional processes, although can be channelised in their proximal regions. Lobes can extend laterally from a few tens of metres to a few tens of kilometres with a relief usually less than 25 m above the seafloor (McHargue et al., 2021; Mulder, 2011). These dimensions are typical for mounded lobes deposited by coarse-grained turbidity currents that pile up, rather than sheet-like lobes deposited by muddy turbidites traveling further into the basin floor (Galloway, 1998; Mulder, 2011). Channels are commonly present in the most proximal parts of lobes prior to a non-channelized distal part (lobe fringe) (McHargue et al., 2021; Mulder, 2011; Spychala et al., 2015).
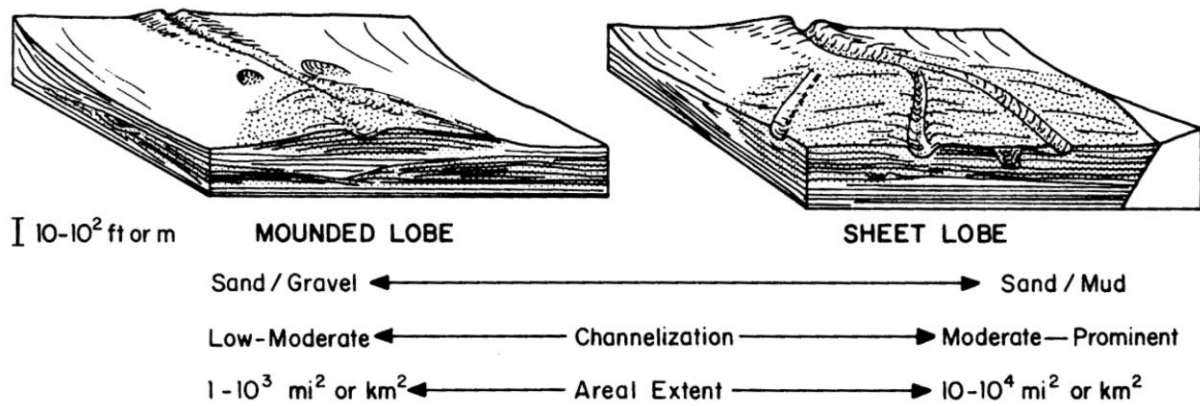
Figure 3. 11: Depositional geometries of mounded lobes and sheet-like lobes, correlated with relevant dimensions. Figure from Galloway (1998).

Lobes in ancient submarine fan models commonly comprise turbidite deposits (commonly 3-15 m thick) with overall thickening upward cycles and convex to sheet-like geometries (Macdonald et al., 2011; Shanmugam, 2000; Shanmugam and Moiola, 1988). Mounded lobes deposits are characterized as amalgamated coarse grained turbidites ranging from a few to tens of metres in thickness and a few km in width, while sheet-like lobe deposits are characterized as well bedded coarse to heterolithic turbidites extending up to several tens of km in length (Figure 3.11) (Galloway, 1998). McHargue et. al. (2021) illustrated the diversity of lobes by studying three distinct lobate examples surrounding a channelized lobe with many distributaries deposited by mud-rich turbulent currents, a non-channelized lobe deposited by mud-poor turbulent currents and remobilized by littoral drift, and a channelized lobe with only a few long and straight distributaries dominated by viscous flows (i.e., debris flows) (Figure 3.12) (McHargue et al., 2021).
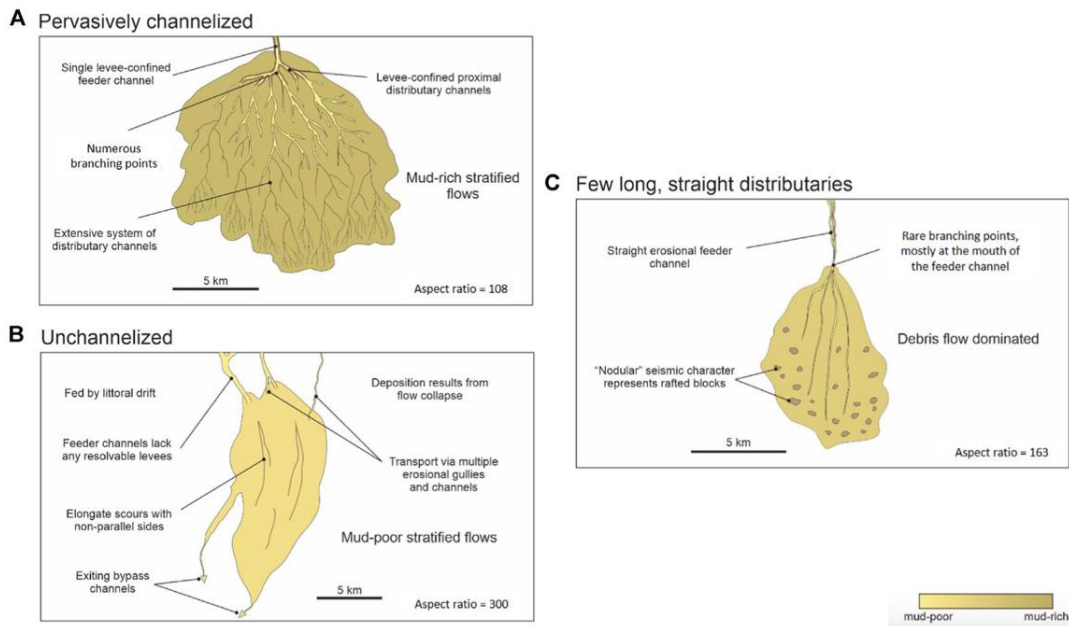
Figure 3. 12: Model illustrating the diversity of depositional lobes from McHargue et al. (2021), including a channelized lobe (A), unchannelized lobe (B), and partly channelized lobe (C). Figure from McHArgue et al. (2021).

Lobes are key building blocks or 'depositional elements' of submarine fans. A generalised model of submarine fan seismic character was established in Mitchum (1985) with an upper fan characterized with channel-levee complexes, and a lower fan characterized with lobate and mounded deposits. Lower fan depositional lobes are characterized as mounded seismic facies with bidirectional downlap and sheet-like internal character (Figure 3.8D) (Mitchum Jr, 1985; Shanmugam, 2000). These mounded, hummocky geometries of lobe seismic-facies can commonly give way to parallel and continuous facies (interpreted as basin plain) on both flanks in a strike section (Shanmugam and Moiola, 1988). In a dip section, the up-dip side may show chaotic reflections of the slope facies, the down-dip side may show parallel reflections of the slope facies, and progradational lobes in between may show very shallow, low angle sigmoidal reflections in appropriately oriented sections in prograding lobes (Shanmugam and Moiola, 1988). Shanugam (2000) highlighted that Mitchum (1985)'s model has insubstantial limitations since 3-15 m thick depositional lobes in outcrop are generally too thin to generate mounds that can be differentiated in seismic reflection profiles. As a result, most seismic imaging tends not to resolve individual *'lobe storeys'* or thinner lobes in the Sprague et al. (2005) hierarchical scheme, typically being only thicker lobes or lobe complexes being resolved (e.g., Deptuck et al., 2008). In unconfined, or only weakly laterally confined systems, lobes, and their composite lobe complexes tend to stack compensationally (Deptuck et al., 2008). However, within strongly laterally confined systems lobes/ lobe complexes may be highly ponded, and show

little in the way of lateral compensational stacking prior to re-incision and basinward progradation (Mayall et al., 2010; Soutter et al., 2019; Spychala et al., 2015), the architecture of lobes within strongly confined settings remains poorly documented, especially in rift settings (cf. Dodd et al., 2019).

Table 3.1: Table summarizing the characteristics of principal geomorphic elements in deep-water fans.

Architectural Elements and Facies in Outcrops and Seismic Sections

Architectural Element	Geological Morphology	Architectural Morphology	Deposits	Seismic Expression	Dimensions
Canyon	Steep-walled, erosional valleys on the shelf, oriented perpendicular to the shelf break.	Asymmetrical v-shaped profile.	Coarse grained turbidite features, chaotic facies, and overbank deposits.	Erosive basal surfaces.	Narrow (a few km) and deep (hundreds of m).
Channel	Depositional and erosive elements formed at the mouths of canyons.	Elongated bodies with concave-up, v-shaped, or u-shaped profiles.	Highly variable. Typically, massive to amalgamated coarse grained turbidites, muddy turbidites and other mass transport deposits. Fining- and thinning upward trends.	Discontinuous high-amplitude basal seismic reflection. Sand-rich deposits characterized with HARs. Debris flow channel deposits characterized with chaotic to transparent seismic facies and grooved basal surface.	Hundreds to thousands of m in width, tens to more than a hundred m in depth, and a few to hundreds of km in length.
Levee	Aggradational sediment wedge located adjacent to a genetically related channel.	Lateral extensive "bird-wing" shape.	Fine-grained sandstone and mudstone turbidite elements.	"Bird-wing" shape with internal reflectors pinching out. Low- to moderate amplitudes and discontinuous- to continuous reflections.	Height ranges from several tens of m to hundreds of m. Lateral extension can reach 50 km.
Lobe	Depositional element found at the lateral terminus of a channel.	Lobate shape in plan view and lens-shaped cross-section. Mounded lobes and sheet-like lobes.	Coarse- to fine-grained turbidite deposits. Debris and mass-transport deposits.	Mounded seismic facies with bidirectional downlap. Strike section: hummocky geometry. Dip-section: up-dip side show chaotic reflections, down-dip side show parallel reflection and progradational lobes show clinoform reflection.	Extends laterally from a few tens of m. Relief less than 25 m.

4 Seismic Modelling

Seismic Modelling helps understanding elastic wave propagation in the subsurface (Lecomte et al., 2016). Seismic data are key to extract information about the earth's subsurface, but seismic images from processed seismic data suffer from known limitations such as detectability, resolution and illumination, and the subsurface geology is unknown (Lecomte et al., 2015). Hence, seismic modelling is a useful tool to improve seismic interpretations with an appropriate method applied (Lecomte et al., 2015).

Mainly three commonly used seismic modelling approaches exists: 1D convolution modelling, 2(3)D full-wavefield modelling, and 2(3)D ray-based modelling. The 1D convolution method is frequently used in the industry but it is only applicable for horizontally stratified structures without lateral velocity variations (Figure 4.1) (Lecomte et al., 2015), and its conceptual validity is thus very limited (Lecomte et al., 2016). The 2(3)D full-wavefield modelling represents an ideal seismic-modelling strategy as it generates complete synthetic seismograms to be processed in the same way as real seismic data, but this method requires high resource costs (Lecomte et al., 2016). The 2(3)D ray-based modelling (RB) generates synthetic seismograms for user-selected wave phase such as P-waves, S-waves, following reflection, transmission, conversion etc. (Lecomte et al., 2015). This method is both fast and accurate and is useful for illumination and resolution studies (Lecomte et al., 2015; Lecomte et al., 2016), although it has its limitations related to modelling detailed target structures (Lecomte et al., 2016).

4.1 Seismic Response

Seismic data are acquired by acoustic sources generating waves of sound energy, and receivers recording the energy that has been reflected in the subsurface due to variations in the impedance (Simm and Bacon, 2014). The seismic response of a seismic wavelet is determined by the reflections generated at an acoustic impedance boundary, that marks a change in the properties of the over- and underlying layers of the boundary, which is measured by the reflection coefficient (RC) (Figure 4.1) (Herron, 2011). The reflection coefficient is a function of the acoustic impedance which is defined as the product of compressional-wave (P-wave) velocity (V) and bulk density (ρ) (Herron, 2011). However, the elastic impedance also requires the shear-wave (S-wave) velocities (Simm and Bacon, 2014).
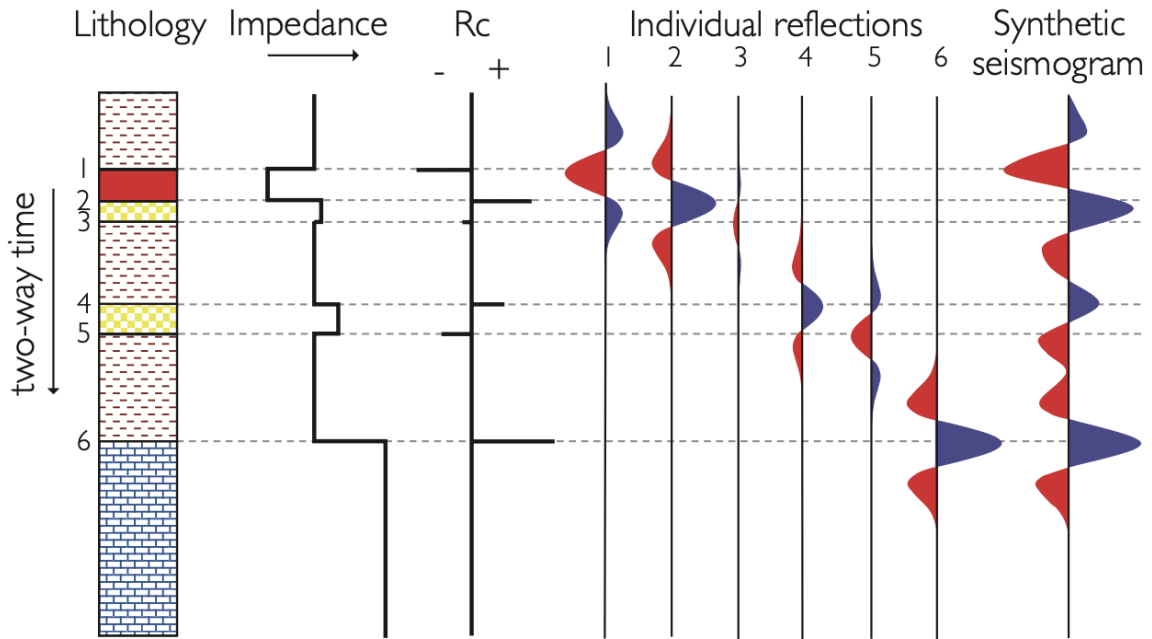
Figure 4. 1: Illustration of how changes in the acoustic impedance between lithological layers generates positive and negative reflection coefficients, producing individual reflections of symmetrical wavelets that together composes a synthetic seismogram. Figure from (Simm and Bacon, 2014).

4.2 Seismic Resolution

Seismic resolution determines how detailed the subsurface geology is exposed in seismic images (Herron, 2011). The seismic resolution is a fraction of the wavelength (λ) which is a function of velocity (v) and dominant frequency (f) through the following equation: $\lambda = \frac{v}{f}$ (Herron, 2011). Resolution varies both vertically and laterally in the subsurface due to velocity variations and frequency changes of the seismic signal (Herron, 2011).

The vertical resolution is indicated by the tuning thickness which is, as a general principle, estimated by: λ/4 (Herron, 2011; Simm and Bacon, 2014). Typically, the frequency decreases and the velocity increases with depth in the subsurface, causing a decrease in the vertical resolution with depth (Simm and Bacon, 2014). The lateral resolution is defined by the Fresnel zone (Figure 4.2), referred to as the area of constructive interference of the wavefront generating reflections (Simm and Bacon, 2014). Migration is an important tool for enhancing the lateral seismic resolution since features smaller than the Fresnel zone will be obscured in unmigrated seismic (Simm and Bacon, 2014). Seismic migration collapses the Fresnel zone by compressing the zone in the inline direction for 2D migration, while also compressing the zone in the crossline direction for 3D migration, thus yielding a smaller circle of diameter λ/2 (Figure 4.2) (Herron, 2011; Simm and Bacon, 2014). Note that the lateral resolution, λ/2 (after migration), is however twice as large as the vertical one λ/4.
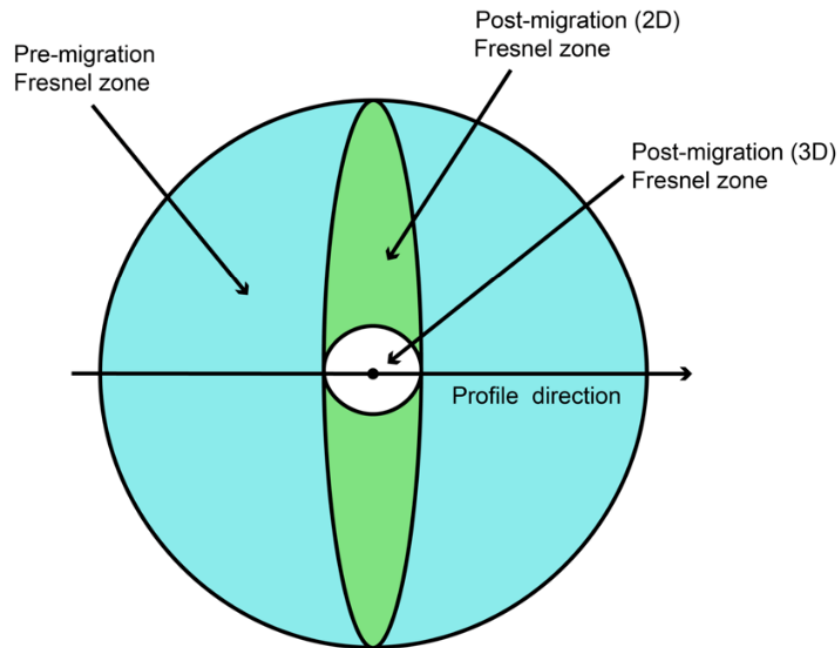
Figure 4. 2: Illustration of the pre-migration Fresnel zone and the collapsed 2D- and 3D post-migration Fresnel zones. Figure from (Andersen, 2020).

4.1 2(3)D Point Spread Function (PSF) Convolution Method

The seismic modelling method used in this thesis is the 2(3)D point spread function (PSF) method which is a simplified ray-based method, extending the 1D-convolution approach to 2(3)D media while keeping the ease-of-use of the latter (Lecomte et al., 2015; Lecomte et al., 2016). This method takes 2(3)D reflectivity grids as input and generates prestack depth migration (PSDM) seismic images by convolving the respective reflectivity model with a prestack convolution operator (the PSF) (Lecomte et al., 2015; Lecomte et al., 2016). Both angle-dependent illumination and resolution effects are considered in the PSFs and obtained as a function of parameters such as background velocity, survey, and wavelet (Lecomte et al., 2015; Lecomte et al., 2016).
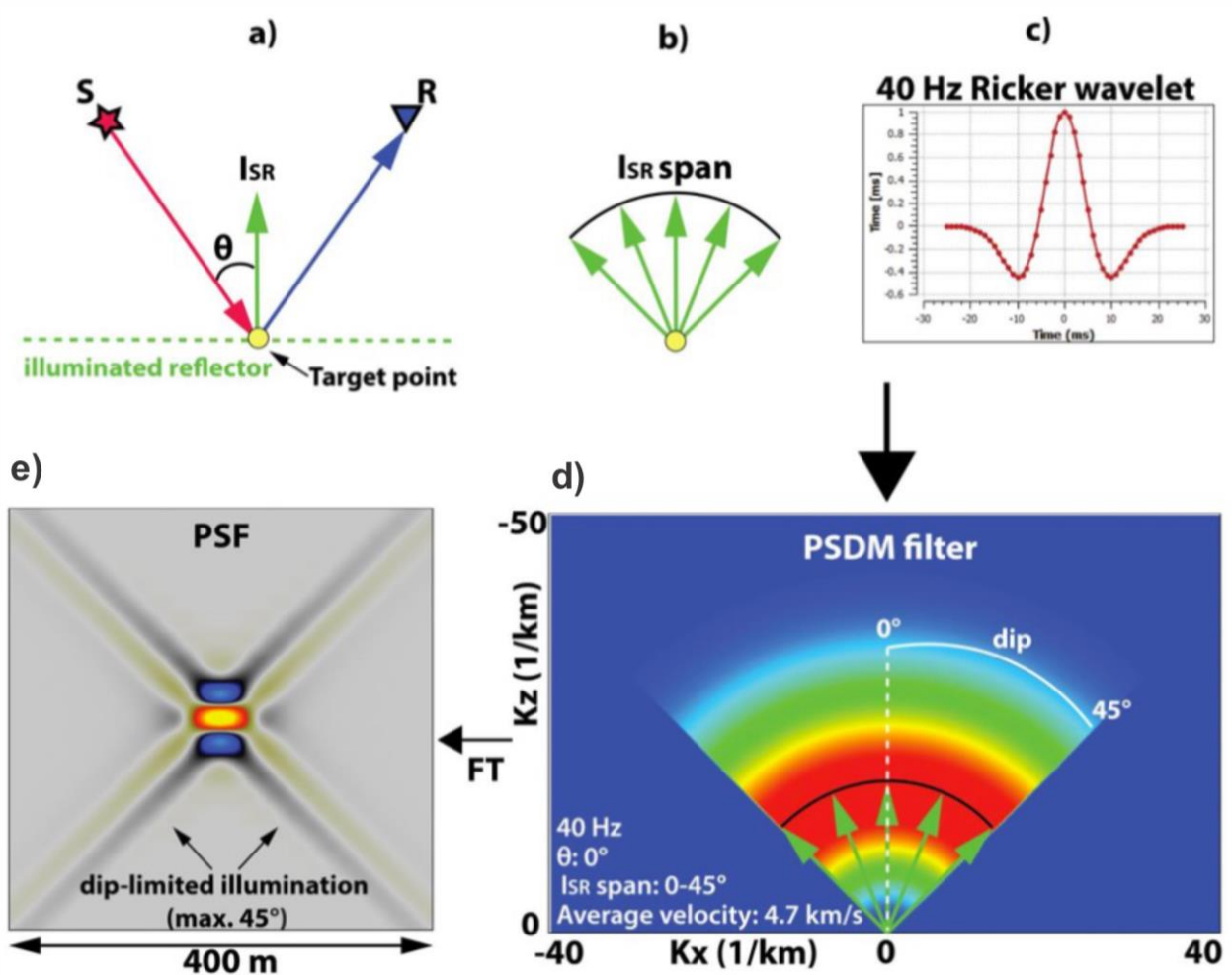
Figure 4.3: Key elements of the PSF convolution modelling. a) Illumination vector I_{SR} generated at a target point (P) for a given velocity model in a survey with a shot (S) and a receiver (R). b) Generic I_{SR} span and b) wavelet (herein the ricker wavelet with frequency 40 Hz) used to generate a PSDM filter. d) PSDM filter being Fourier Transformed (FT) used to generate e) a PSF with an illumination angle of 45° (reflectors steeper than 45° will not be illuminated for this case). The cross pattern artefact on the PSF is caused by filter truncation (Lecomte et al., 2016). Figure modified from (Andersen, 2020).

An essential element of the PSF convolution method is the illumination vector (I_{SR}) (Figure 4.3 a) (Lecomte et al., 2016). The reference point or target point (P) in a given velocity model marks where the I_{SR} are generated in a survey with a set of shot (S) and a receiver (R) pairs (Lecomte et al., 2016). The illumination and resolution of the PSDM imaging at the reference point is controlled by the orientation and length of the I_{sr} (Lecomte et al., 2016). In particular, if an I_{sr} is oriented perpendicular to a reflector close to the reference point, that reflector will be illuminated and appearing on the PSDM image (Lecomte et al., 2016). For instance, a horizontal reflector will only be illuminated if a vertical I_{sr} is present (Lecomte et al., 2016). Generic I_{sr}-spans can be generated if both background model and survey information are unavailable (Figure 4.3 b) (Lecomte et al., 2016), as for the seismic modelling in this thesis. A PSDM filter is then generated from the desired I_{st}-span here defined by the so-called illumination angle

corresponding to the steepest illuminated geological dip (45° in Figure 4.3, selected as a proxy for standard seismic acquisition), together with other parameters, such as wavelet (Figure 4.3 c), average velocity in the targeted area and incident angle (Figure 4.4 illustrates the difference between illumination angle and incident angle) (Lecomte et al., 2016). The resulting PSDM filter is further Fourier-Transformed (FT) (Figure 4.3 d) to generate a PSF (Figure 4.3 e) to be convolved with a reflectivity model to generate synthetic seismic (Lecomte et al., 2016).
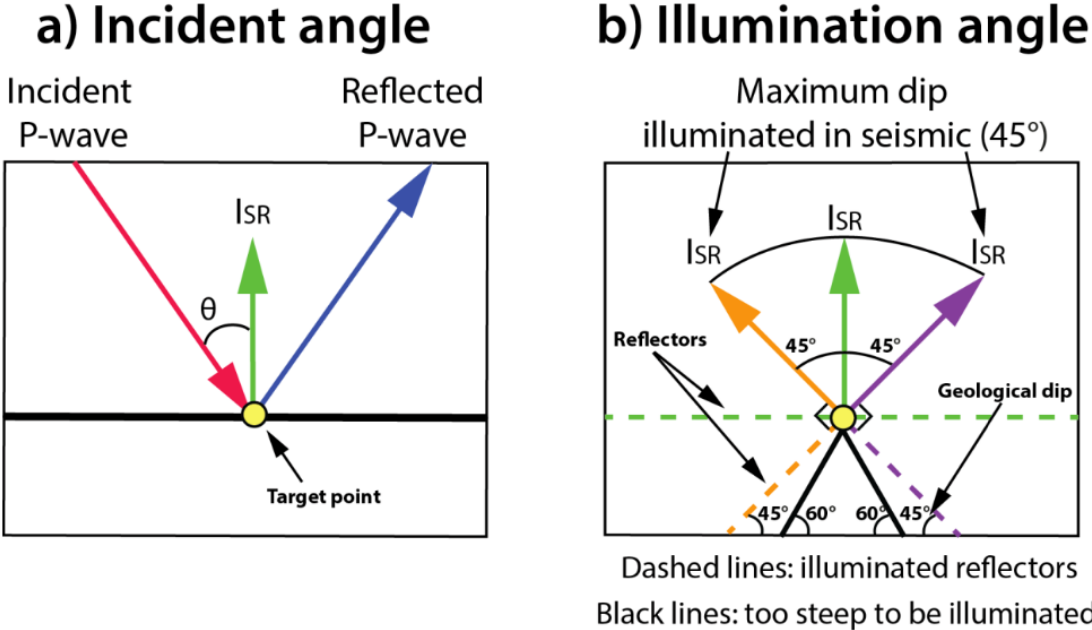
Figure 4.4: a) The incident angle (θ) is defined here for an incoming seismic wave (red arrow) reflected at a horizontal reflector (blue arrow), hence having a vertical I_{SR} (i.e., normal to the reflector; green arrow). b) The illumination angle defines the maximum reflector dip that can be illuminated. In this case, the illumination angle is set to 45° (steepest illuminated dip) and the associated I_{SR} span is represented, where potentially illuminated reflectors are marked with a dashed line (green, orange, and purple), while non-illuminated reflectors (exceeding the maximum illumination angle) are marked with a black continuous line. Per definition, the I_{SR} are perpendicular (normal) to the potentially illuminated reflectors. Figure from (Andersen, 2020).

5 Data and Methodology

This chapter provides an outline of the data acquisition and methods applied on the respective data in the process of generating 2D synthetic seismic images based on 3D virtual outcrop models. The Olive Grove and Stomio outcrop models from the WXFB located on the southern onshore Gulf of Corinth (Greece) were made by Tim Cullen within the SynRift Systems PETROMAKS2 project between 2017 and 2019. These outcrop models along with field observation for the Syn-Rift systems fieldwork comprise the dataset used in this thesis and were interpreted geologically and assigned elastic properties with the aim of constructing geological models (geomodels) to be used as input for seismic modelling.

5.1 Data acquisition

Virtual outcrop models built by photogrammetric techniques provides the opportunity to remotely visualize and investigate geological outcrops including inaccessible areas (e.g., Bemis et al., 2014; Bilmes et al., 2019; Burnham and Hodgetts, 2019). The Olive Grove and Stomio models were created by using DJO Phantom 3 and Mavic Pro UAVs (Unmanned Aerial Vehicle) to collect imagery for Structure-from-Motion (SfM) photogrammetry using several hundred outcrop images with sufficient overlap ($\approx 30 - 50$ %) (Cullen, 2020). Location information for each image were stored through associated metadata and control points at the ground were collected if possible in order to calibrate them during processing (Cullen, 2020). If control points were unobtainable (e.g., when investigating inaccessible areas) a 'homepoint image' was used which involves taking a picture on the UAV with known field GPS coordinates that record the drones take-off point (Cullen, 2020). The collected images were further processed in Agisoft Photoscan Professional (now renamed Agisoft Metashape) to build fully textured, 3D triangulated meshes (Cullen, 2020). The workflow from collecting images in field through to a 3D digital outcrop model is summarised in Figure 5.1 based upon recent methodological reviews (Bilmes et al., 2019; Burnham and Hodgetts, 2019).

Photo Acquisiation

Ensure lighting conditions are good for the exposure (limited contrast). >70% overlap where possible. Fly at distance suitable for required resolution.

Import and quality-check photographs

1. Choose high quality, representative images (no blur, poor exposure etc.)
2. Check locations seem consistent with flight pattern (e.g. blue squares right are each located photograph) and QC altitude data
3. Mask unwanted areas of photos (sky, dense vegetation)

Align Photos (Sparse Cloud Generation)

1. Run Alignment workflow within Agisoft with 'High Accuracy' settings.
2. Quality check result and reiterate with removal of erroneous or low accuracy points.
3. Crop sparse cloud to required area to reduce processing time.
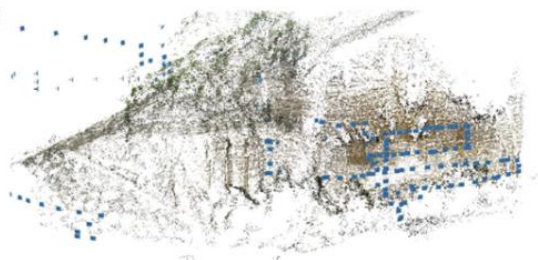
Dense Cloud Generation

1. Using cleaned and trimmed Sparse Cloud, populate the Dense Cloud using the Dense Cloud workflow within Agisoft
2. Select 'High Quality' for most models. Where models are too large to process, split into seperate areas and process at High Quality
3. Clean and trim produced Dense Cloud.
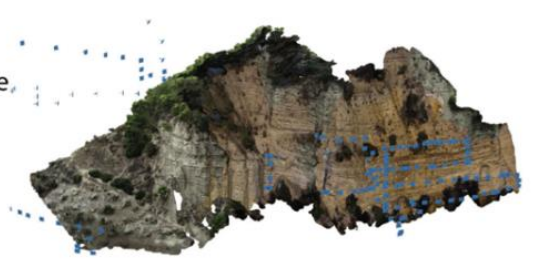
Mesh and Texturing

1. Use mesh generation workflow to generate a triangluated mesh between the points of dense cloud.
2. Use depth maps from Dense Cloud reconsutrction, and select high quality and high face count settings (customise where appropriate).
3. Run texture workflow on completed mesh for photorealistic 3D model. Settings will be resolution dependent.

Figure 5. 1: Summary of digital outcrop model generation workflow from Cullen (2020).

5.2 From Outcrops to Geological Models

Outcrop Interpretations and Sedimentary Logs

The generated digital outcrop models were exported to the software LIME that allows for measurements and interpretations of 3D models (Buckley et al., 2019). Both the Olive Grove and Stomio models were interpreted in a hierarchical relationship based on different scales of lithological and geometrical changes. The highest order corresponds to the WX-units (described in Chapter 2.2 (Study Area) from Cullen et al. (2020) and the lower order breaks down major- and minor stratigraphic boundaries to separate sedimentary packages. Depending on the resolution, single beds and architectural elements were further outlined within several boundaries.

For the accessible areas of the Olive Grove model both sedimentary logs from field (OG-A, -04, -09, and -10) and images taken in field to be logged (OG-B, -C, -D, and -E) were provided by Tim Cullen. Additionally, seven pseudologs were made as an extension from the above forementioned field logs for the Olive Grove Model and five approximately equally spaced pseudologs were made for the Stomio Model. The hierarchical interpretations and sedimentary logs, together with published literature (Cullen, 2020; Cullen et al., 2020; Gobo et al., 2015; Rubi et al., 2018), formed the basis for deriving a depositional and architectural interpretation of the virtual outcrop models and making complete geomodels.

Geological Models

The complete geomodels were made in the vector graphics software program Adobe Illustrator by exporting each outcrop model as a high-resolution 2D image from AgiSoft and LIME to take the interpreted stratigraphic boundaries, and add under- and overburden stratigraphy, thereafter, assign colours to the different lithological packages/ units. In addition, a larger, fault-block scale, geomodel was made using a cross-sectional stratigraphic correlation panel for the West Xylokastro Fault Block from Cullen et al. (2020) (further referred to as the 'cross-section' geomodel). (Figure 2.5). The three resulting geomodels were converted to greyscale in the digital photo editing software program paint.net with colour codes extracted for the various lithological units. The greyscale images were saved as PNG files to be used as input in a MATLAB code where the extracted grey codes were identified to assign a lithological-unit index (integer) and elastic properties including P-wave velocity (Vp), S-wave velocity (Vs) and density. This code generated the distribution of values for each property, as well as noise, in

separate 2D grids and stored each in a SEG-Y file, to be used for the 2D synthetic seismic forward modelling in SeisRoX (NORSAR Software Suite).

5.3 Elastic Properties

The elastic properties (Vp, Vs and density) assigned to the geomodels were extracted from released well-data using the DISKOS database from two wells from the Late-Jurrassix Melke Formation in the Fenja Field located on the Southern Haltern Terrace, offshore Norwegian Sea: 6406/12-3 B and 6406/12-3 S (Figure 5.2). The Halten Terrace area composes a small, confined syn-rift basin (3 by 5 km^2) fed by a local basement high (Jones et al., 2021). The wells drilled at the Halten Terrace target Upper-Jurassic syn-rift stratigraphy providing an advantageous subsurface record of the variability and complexity within these deposits (Jones et al., 2021). The complete syn-rift succession is broadly composed of early-rift fine-grained gravity flow deposits, peak-rift coarse-grained, submarine fan systems deposited by gravity flows, followed by landslide complexes deposited due to footwall uplift during rifting, and late-rift mud-rich deposits with small coarse-grained apron fans (Jones et al., 2021). The properties were extracted from these wells since the geological setting of the Melke Formation in the Fenja Field shows similarities to the setting in the West Xylokastro Fault Block (Cullen et al., 2020; Cullen et al., 2021) and allows for important analogue comparisons to be made between the two setting. Values for Vp, Vs and bulk density were determined taking the mean over the depth range for a given lithology. Vp, Vs and density values were extracted for a mudstone, sandstone, conglomerate, and mass-transport deposit intervals below the free-water level, determined by resistivity data, for each well. The core photos of the selected lithological intervals for both wells are shown in Figure 5.3, and the corresponding depths are given in Table 5.1. The cored intervals did not cover sufficient thicknesses of mudstones, therefore, depth sections confirmed by remarkably high gamma-ray values (ranging from 66 to 120 for well 6406/12-3 B and 65 to 147 for well 6406/12-3 S) were used to extract velocity and density values. The values were extracted from dipole sonic logs where the velocities are given in μs/ft and were converted to m/sec by using the following equation: $velocity = \frac{1}{\Delta t \mu s/ft * 10^{-6}} * 0,3048$ (Rider and Kennedy, 2011) (Table 5.2 and 5.3).
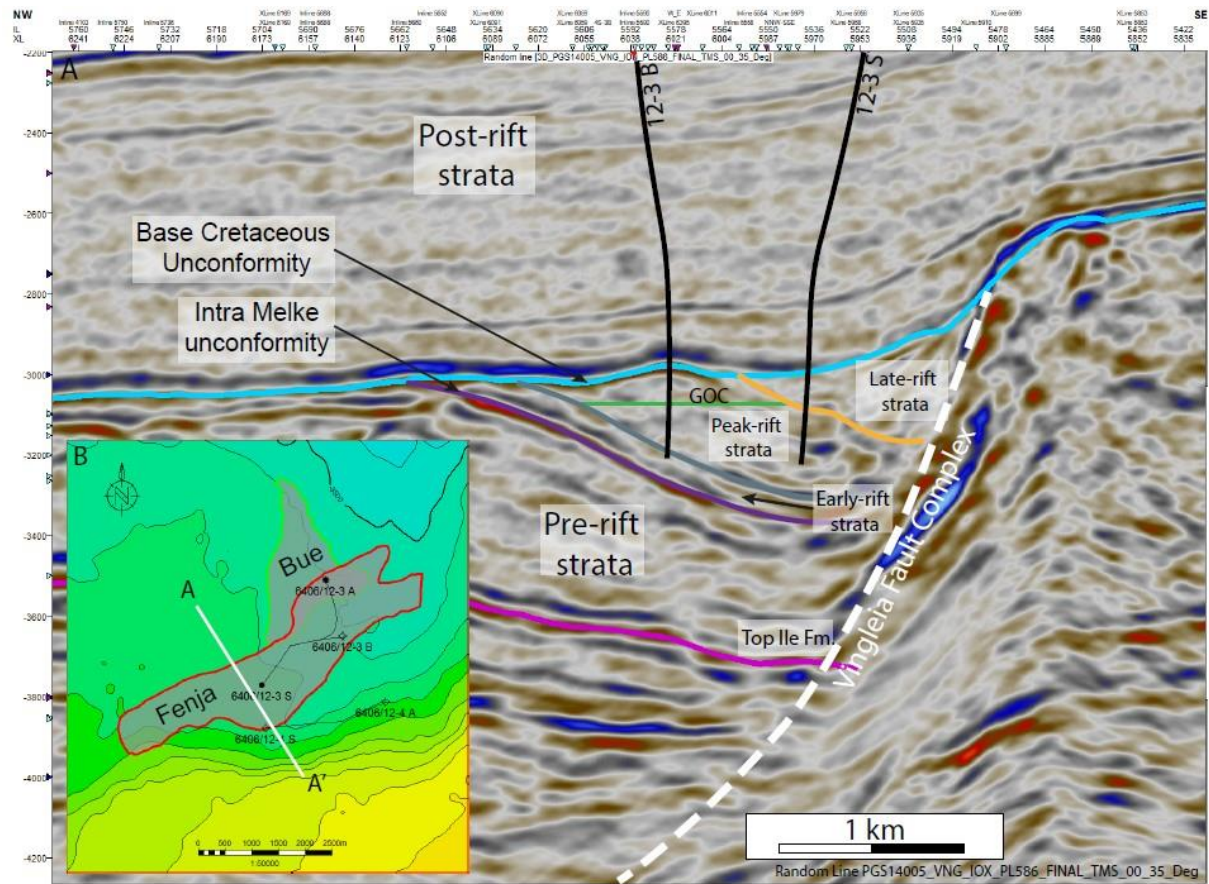
Figure 5. 2: A) Seismic profile showing locations of well 6406/12-3 B and -S and key stratigraphic surfaces. B) Regional map of the Fenja field where seismic profile (A) is marked as A-A'. Well 6406/12-3 S is located centrally in the basin, while well 6406/12-3 B is located closer to the flank. Figure from (Jones et al., 2021).

Table 5. 1: Core depths for the lithological intervals for the 6406/12-3 B and -S Haltern Terrace offshore wells. rkb = rotary kelly bushing.

Depths of Lithological Intervals

Well Name: 6406/12-3 B		Well Name: 6406/12-3 S	
Lithology	**MD (m rkb)**	**Lithology**	**MD (m rkb)**
Mudstone	3925,4 – 3934,2	*Mudstone*	3765,1 – 3767,1
Sandstone	3855,0 – 3858,0	*Sandstone*	3720 ,0– 3721,0
Conglomerate	3844,5 – 3845,4	*Conglomerate*	3711,5 – 3713,3
Mass Transport Deposit	3847,7 – 3849,1	*Mass Transport Deposit*	3524,5 – 3528,3
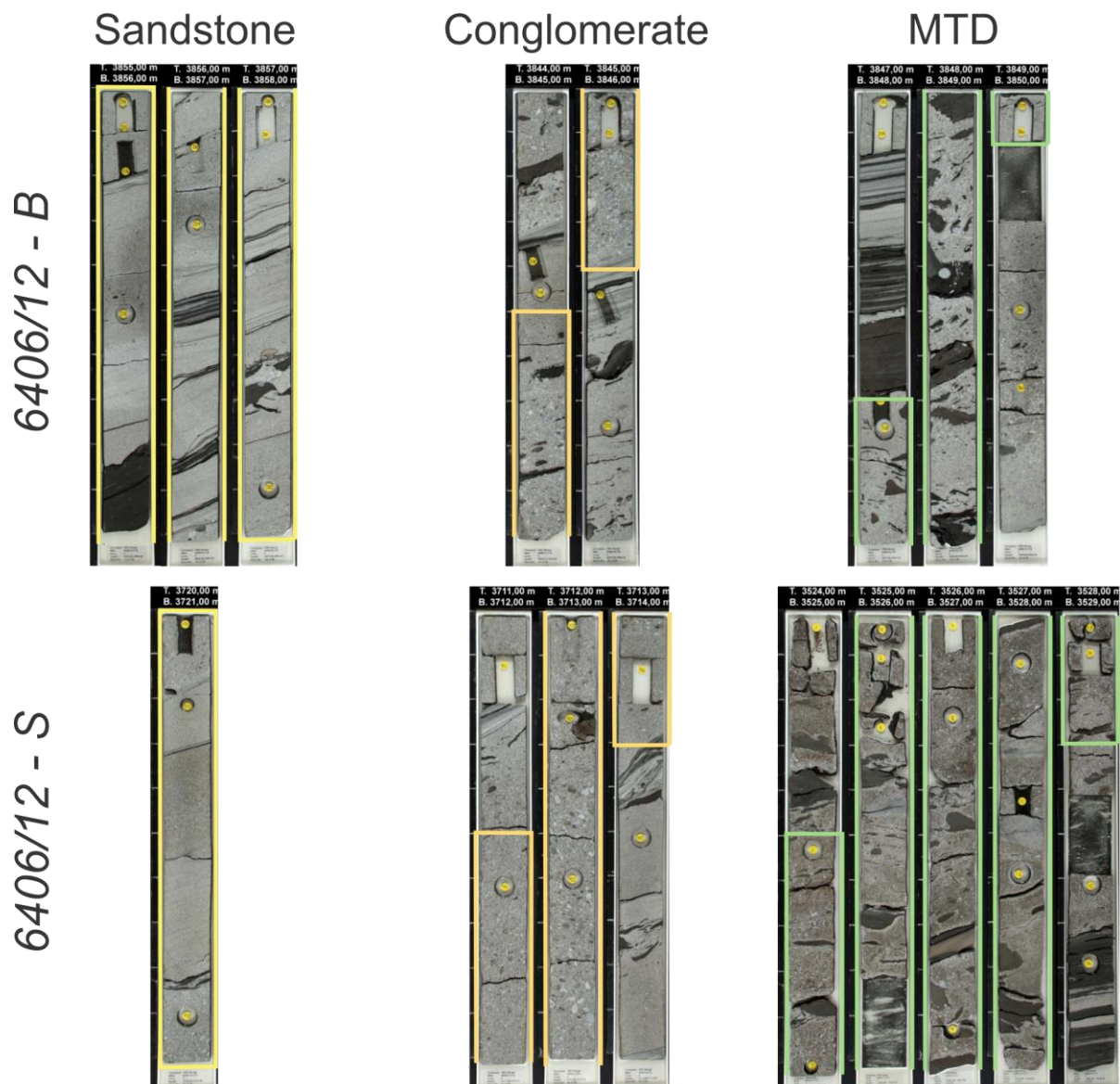
Figure 5. 3: Sandstone, conglomerate, and mass-transport deposit intervals within the core sections from wells 6406/12 – B and – S. MTD = Mass-transport deposit.

Table 5. 2: Elastic properties from the 6406/12-3 B Haltern Terrace offshore well.

Elastic Properties:6406/12-3 B

Lithology	Geomodel Colour	Vp (km/s)	Vs (km/s)	Density (g/cc or kg/dm³)
Mudstone	Grey	3,9	2,2	2,6
Sandstone	Yellow	4,1	2,5	2,4
Conglomerate	Orange	4,2	2,5	2,4
Mass transport deposit	Green	4,0	2,5	2,5

Table 5. 3: Elastic properties from the 6406/12-3 S Haltern Terrace offshore well.

<p align="center">Elastic Properties: 6406/12-3 S</p>

Lithology	Geomodel Colour	Vp (km/s)	Vs (km/s)	Density (g/cc or kg/dm^3)
Mudstone	Grey	3,8	2,4	2,6
Sandstone	Yellow	4,0	2,4	2,4
Conglomerate	Orange	3,9	2,3	2,4
Mass transport deposit	Green	3,8	2,3	2,4

5.4 Seismic Modelling

The 2D synthetic seismic images based on the geological outcrop models were generated by using the PSF-based convolution method of SeisRoX. Various geophysical parameters were explored for the three geomodels, including frequency, maximum illumination angle, incident angle and level of noise, with the aim of investigating their prominent effect on the generated reflectivity models and seismic sections (Table 5.3). The wavelet type were set consistent, using the Ricker wavelet, which is a zero-phase wavelet characterized with a central peak and two side lobes (Ricker, 1940; Ryan, 1994). The theoretical principles behind the PSF convolution method and associated geophysical parameters are explained in Chapter 4 (Seismic Modelling) and the workflow from outcrop to 2D synthetic seismic is illustrated and explained in Figure 5.4. The 2D synthetic seismic profiles and noise sections were amplitude-calibrated in order that an isolated horizontal reflector of reflectivity strength of +1 will correspond to a modelled seismic amplitude strength of +1 in the calibrated seismic (Faleide et al., 2021). This allows direct comparisons with the input reflectivity and across all modelled seismic sections, whatever the selected parameters. With actual seismic, such amplitude calibration is also necessary and carried out at well ties, the extracted wavelet implicitly containing the calibration factor.
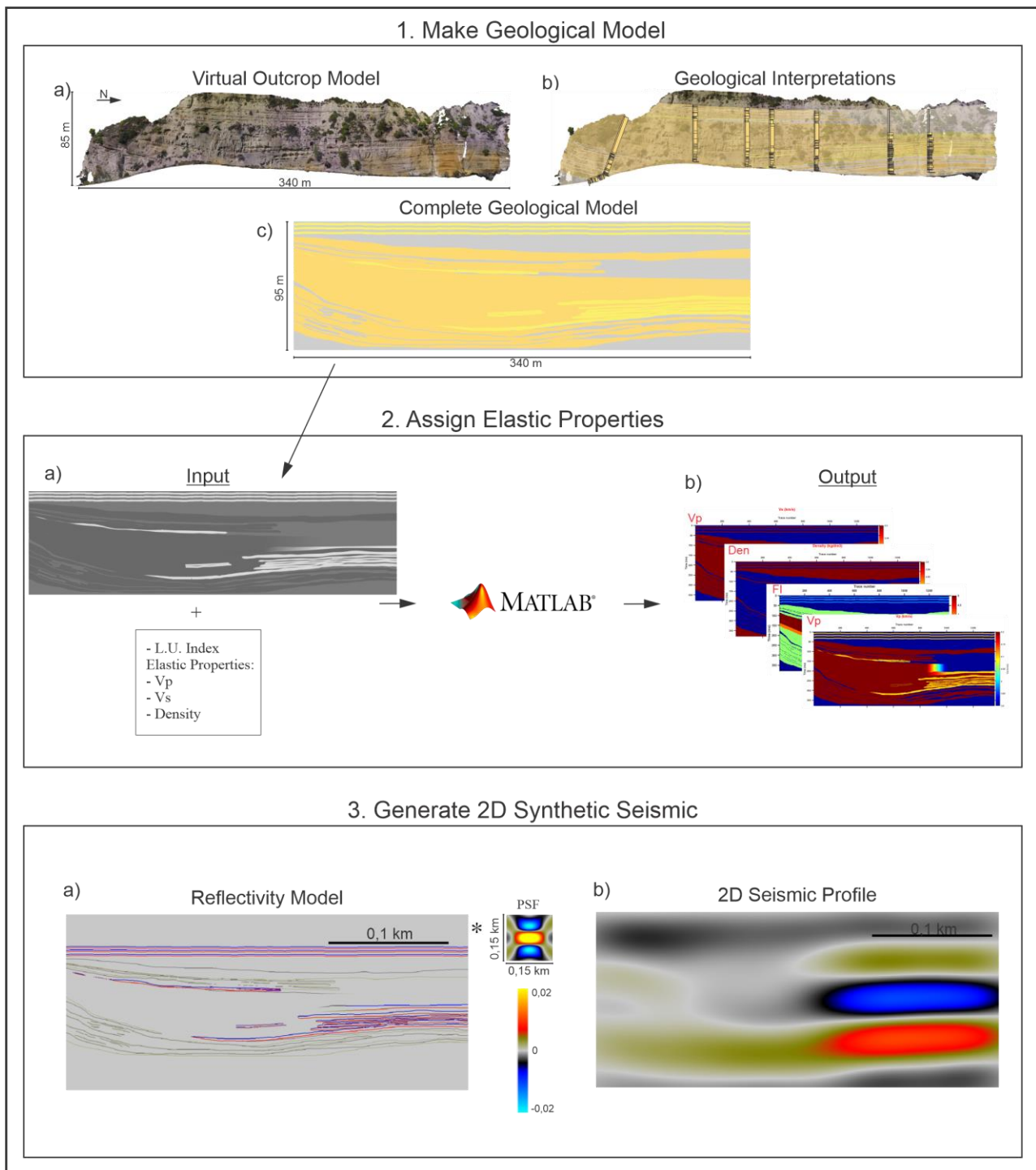
Figure 5. 4: An illustration of the workflow from 3D outcrop models to 2D synthetic Seismic. 1. (a) A virtual outcrop model ('Olive Grove' model used as example) is used to construct a geological model (b) by performing geological interpretations in LIME by mapping out stratigraphic boundaries to separate different lithological packages. (c)The complete geomodel is made in a graphics software program. 2. (a) (input)The geomodel is further converted to a greyscale image saved as a PNG file to be used as input, together with a lithological-unit number and elastic properties, in MATLAB. L.U Index = Lithological-unit Index. (b) (output) to generate four SEG-Y files where the distribution of the values for each property is stored in a grid. 3. (a) The SEG-Y files are imported to SeisRoX and used as input for property cubes defining the target model. By running a wavelet-based workflow, where the essential geophysical parameters are selected, a reflectivity model is first generated. The reflectivity model is finally convolved with a PSF to generate 2D synthetic seismic (PSDM alike). PSF =Point Spread Function.

Table 2.3: Overview of the various parameters explored for the different geomodels, and set associated parameters are listed. IA = Incident Angle, MIA = Maximum Illumination Angle, Fr = Frequency.

	Incident Angle (°): 0, 10, 20, 30	*Maximum Illumination Angle (°): 10, 20, 45*	*Frequency (Hz): 20, 40, 60, 140*	*Level of Noise (%): 25, 50, 100*
Cross-Section	MIA: 45° Fr: 40 Hz	IA: 20° Fr: 20 Hz	MIA:45° IA: 20°	IA: 20° MIA: 45° Fr: 20 Hz
Olive Grove	MIA: 45° Fr: 20	None	*Only 140 Hz* MIA:45° IA: 20°	IA: 20° MIA: 45° Fr: 20 Hz
Stomio	None	None	MIA: 45° IA: 20°	IA: 20° MIA: 45° Fr: 20 Hz

6 Results

This chapter presents the results of the geological interpretations of the 'Olive Grove' and 'Stomio' outcrop models, and the 2D synthetic seismic sections generated from the constructed geomodels. The seismic modelling results include 2D synthetic seismic images of the 'cross-section', 'Olive Grove'- and 'Stomio' geomodels. Various geophysical parameters were assigned, including dominant frequency, incident angle and illumination angle, in order to examine how these parameters, in addition to geological complexity, can influence the resulting seismic signature.

6.1 Stratigraphy and Outcrop Architecture

In this study, three geomodels are constructed from digital outcrops and published data to produce lithological geobodies consisting of mudstone, sandstone, conglomerate, and mass-transport deposit, to be used as input for the seismic modelling. In addition, an overburden stratigraphy of alternating sandstones and mudstones is assigned to initiate some signal above the geological models and remove boundary effects from the area of interest. The larger fault block scale geomodel derived from the cross-sectional stratigraphic correlation panel from Cullen et al. (2020), shown in Figure 6.1, was made through correlation and projection of stratigraphic units between the exposure panels.

The 'Olive Grove' and 'Stomio' outcrop models were interpreted stratigraphically and architecturally in a hierarchical relationship with major bounding surfaces drawn on the basis of stratal terminations, lithofacies changes or character (e.g., erosion) in order to construct realistic geomodels. The following sections summarize the geological interpretations for both outcrop models within the WX-units, whereas a detailed description for each of the major and minor boundaries can be found in Appendix 1 for 'Olive grove' and Appendix 2 for 'Stomio'. 'Olive Grove' is a more accessible outcrop than 'Stomio', providing the opportunity to make more detailed interpretations based on previous field observations.
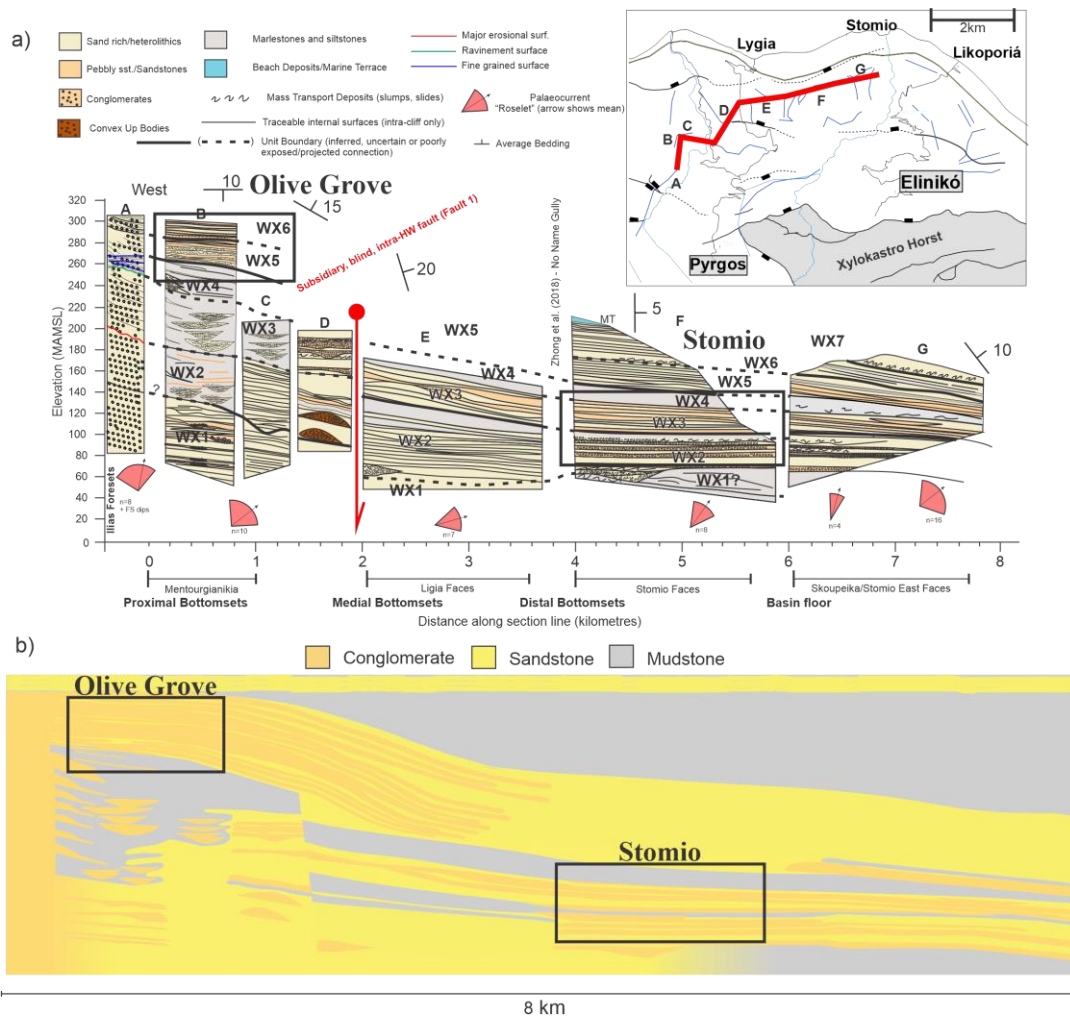
Figure 6. 1: a) The stratigraphic correlation panel from Cullen et al. (2020). b) The 'cross-sectional' geomodel derived from a). Locations of the 'Olive Grove' and 'Stomio' outcrops are marked in both a) and b).

6.1.1 Olive Grove

The 'Olive Grove' outcrop exposes proximal bottomset deposits of the Ilias delta within the WX5-7 units (Cullen et al., 2020). The interpretations from a 3D virtual outcrop model to a geomodel of the 'Olive Grove' outcrop are presented in Figure 6.2. Overall, the outcrop is dominated by conglomerates with sub-ordinate mudstone and sandstone packages which vary locally. The different lithological units interpreted from the geomodel distinguish between conglomerates, sandstones, and mudstones. These units are mapped out on the 'Olive Grove' outcrop model showing a general trend to increase the non-conglomeratic portion of the stratigraphy towards the northern, down-dip, part of the outcrop (figure 6.2 c). Detailed full field- and pseudologs are attached in Appendix 3. The complete geomodel with correlated lithological units within WX5, WX6 and WX7 and over- and under burden stratigraphy is shown in Figure 6.2 d.
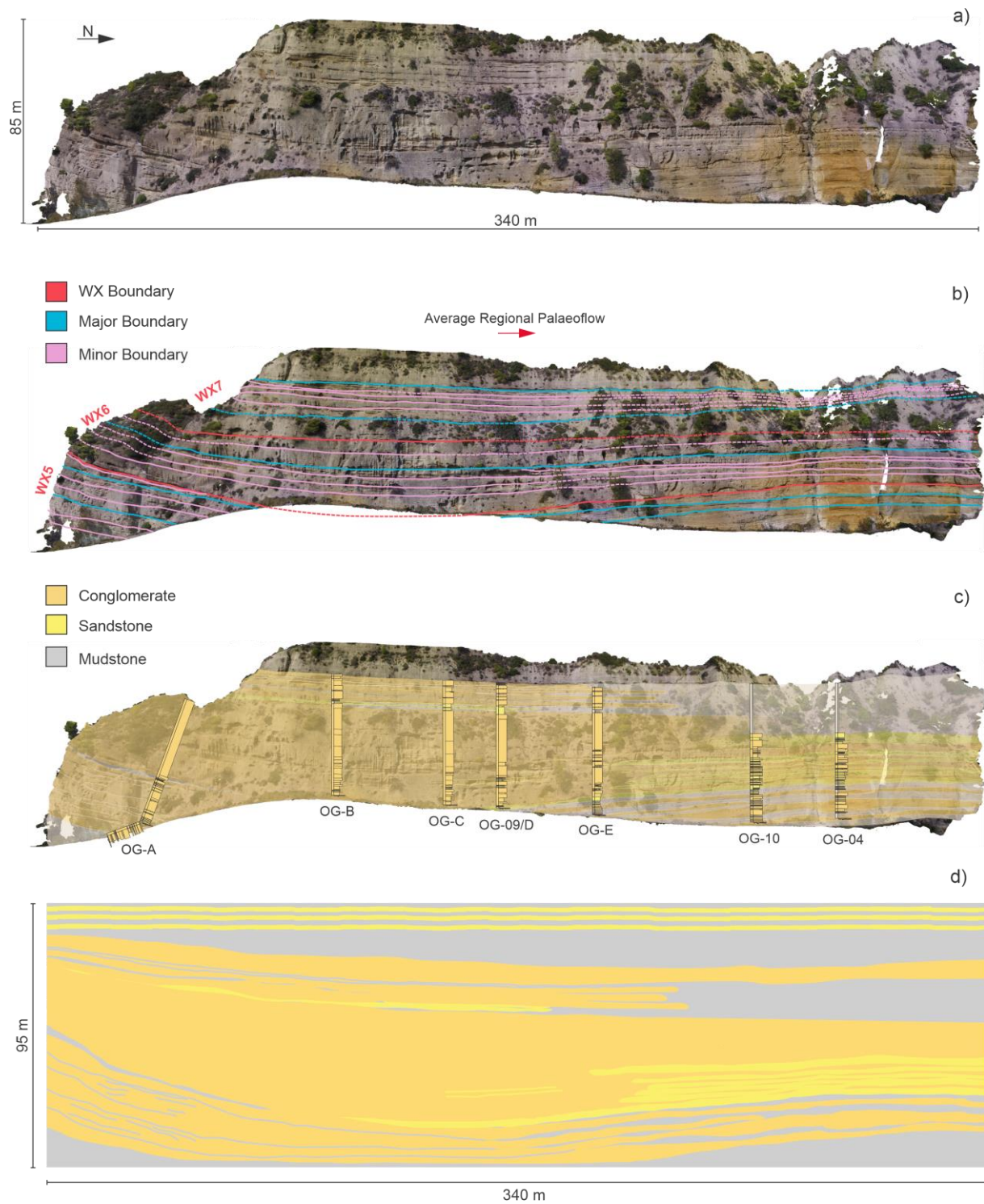
Figure 6. 2: a) The 'Olive Grove' outcrop model with dimensions and North direction marked. b) Hierarchical interpretation with WX-, major-, and minor boundaries marked, as well as average regional palaeoflow direction. c) Interpreted lithological units of the 'Olive Grove' outcrop model, with overlain pseudologs. d) Complete geomodel with marked dimensions.

WX5 South

WX5 in the southern part of the 'Olive Grove' outcrop has an average dip of 13° towards the North and is composed of stacked and amalgamated conglomerates interbedded with mudstones (Figure 6.3). The conglomerate beds are often massive and structureless, ranging from matrix- to clast supported, with rounded to sub-rounded small pebble- to cobble-sized clasts with variations in bed thicknesses from 0,2 m to 3,5 m (Figure 6.3 and OG-A). Where trends in grainsize are observed, they are often highly variable spatially, exposing fining and coarsening upward trends in clast and matrix sizes. Bed thicknesses intervening mudstone layers are typically less than 0,3 m. The conglomerate layers thicken upwards within Unit S.1 and become thinner and more stratified upwards within Unit S.2. The lower part of Unit S.3 is composed of conglomerates interbedded with mudstones, and the upper part is composed of mudstones with thin gravelly layers with typical bed thicknesses of < 1 m (Figure 6.3 b). Unit S.3 generally thins out northwards due to the erosion at the surface separating WX5 and WX6. Conglomerate packages within WX5 are interpreted to be the deposits of debris- and granular flows forming bottomset-foreset transition lobes or bars (Gobo et al., 2014; Talling et al., 2012), while thinner mudstones are interpreted to be deposited by following more dilute parts of a flow as a lower-velocity turbidity current (Gobo et al., 2014; Lowe, 1982; Talling et al., 2012). The thin gravelly layers within the mudstone-rich S.3 Unit indicate erosional scours forming during sediment bypass (Stevenson et al., 2015).
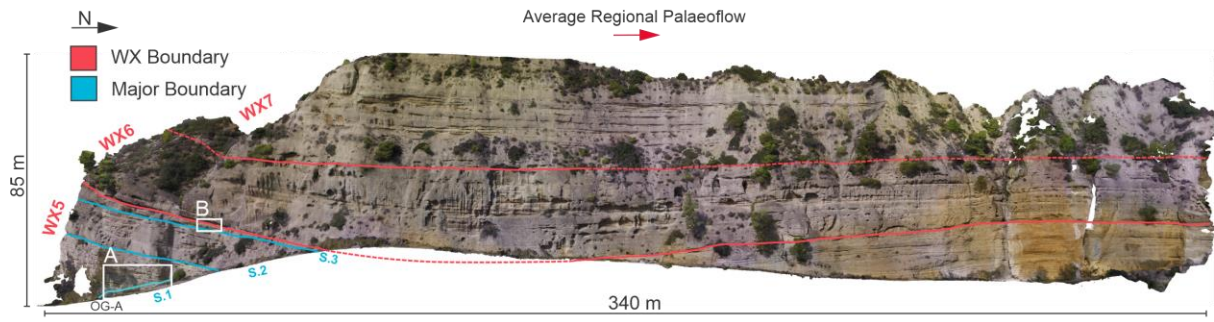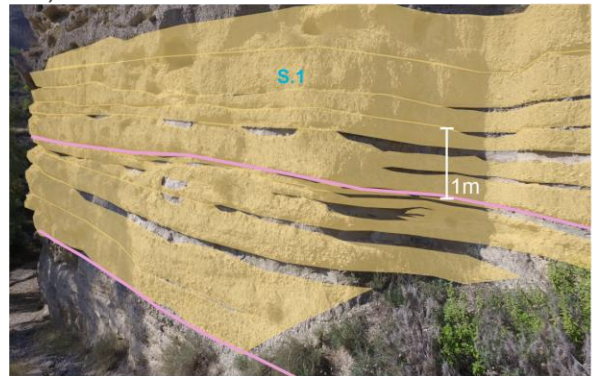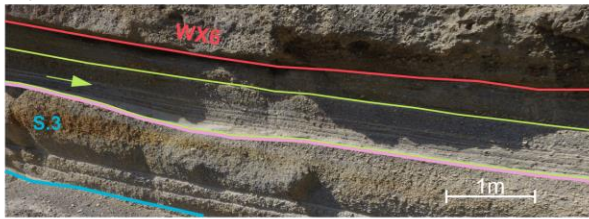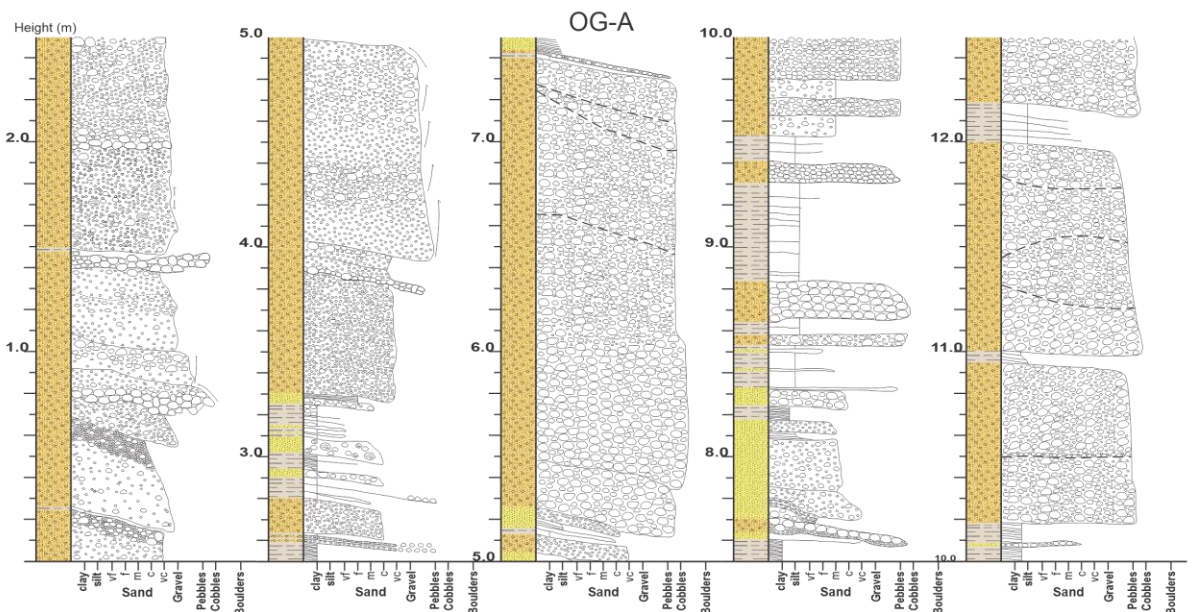
Figure 6. 3: Location of a is marked with box A on the 'Olive Grove' outcrop model and log OG-A is marked with a light blue line. a1) shows lower parts of the Southern WX 5 unit with log OG-A marked in light blue. a2) shows a1 with conglomerate layers marked with transparent orange colour. Location of b is marked with box B on the 'Olive Grove' outcrop model. b) Mudstones with thin gravelly layers are marked within green lines and - arrow. The erosive WX6 boundary is also marked.

WX5 North

The WX5 unit in the northern part of the 'Olive Grove' outcrop dips gently towards the South (~ 5°), with steepest dips in the southern part and approximately horizontal in the northern part. The unit is mainly composed of alternating layers of massive and structureless conglomerates and planar laminated mudstones, with an increasing proportion of mudstone beds upwards (Figure 6.4 and 6.5). In addition, some parts of Units N.1 and N.3 are cut by small faults (Figure 6.4 a) from post depositional mass-movement. The upper part of WX5, Unit N.3, is composed of mudstones with typical bed thicknesses of less than 1 m and thin (< 0,5 m thick) gravelly conglomerates and coarse sandstones layers, which comprise the basis for the correlation of the overlying erosive WX6 unit (Figure 6.4 a). Unit N.1 and N.2 are composed of lens-shaped conglomerates with both pinch-out and pinch and swell geometries, becoming more parallel bedded towards the North (Figure 6.4 b and 6.5). Grain-size trends within the conglomerates are variable, exposing both normal and inverse grading, and conglomerate clasts are rounded to sub-rounded gravel to cobbles. Unit N.2 has a higher proportion of mudstone layers and less variation in conglomerate bed thicknesses than Unit N.1. Conglomerate bed thicknesses are typically 0,5 m in Unit N.2, while the thicknesses range from 0,1 m to 2,5 m within Unit N.1. The mudstone layers are typically 0,3 m within Unit N.2 and 0,1- 0,4 m within Unit N.1. Silt-rich mudstones within Unit N.1 expose both current ripples and climbing ripples (Figure 6.5 d, log OG-04) indicating a unidirectional flow with a high flow regime and rates of aggradation rather than hemipelagic/ hemnilimnic fallout (Jobe et al., 2012). The conglomerates within unit N.1 and N.2 are interpreted to be medial bottomset lobes or bar deposits deposited by debris flows, and the overlying mudstone layers are interpreted to be deposited by a following dilute flow (Gobo et al., 2014; Talling et al., 2012). The lens shaped conglomerates in figure 6.5 c display a compensational stacking pattern at the bed scale, indicating the development of substantial topography conglomerate deposits which affects later flows (Deptuck et al., 2008). The mudstones within unit N.3 are interpreted to be deposited by dilute flows (low-velocity turbidity currents) (Gobo et al., 2014; Lowe, 1982; Talling et al., 2012) with thin gravelly layers of sediment bypass (Stevenson et al., 2015).

Olive Grove WX5 (N)
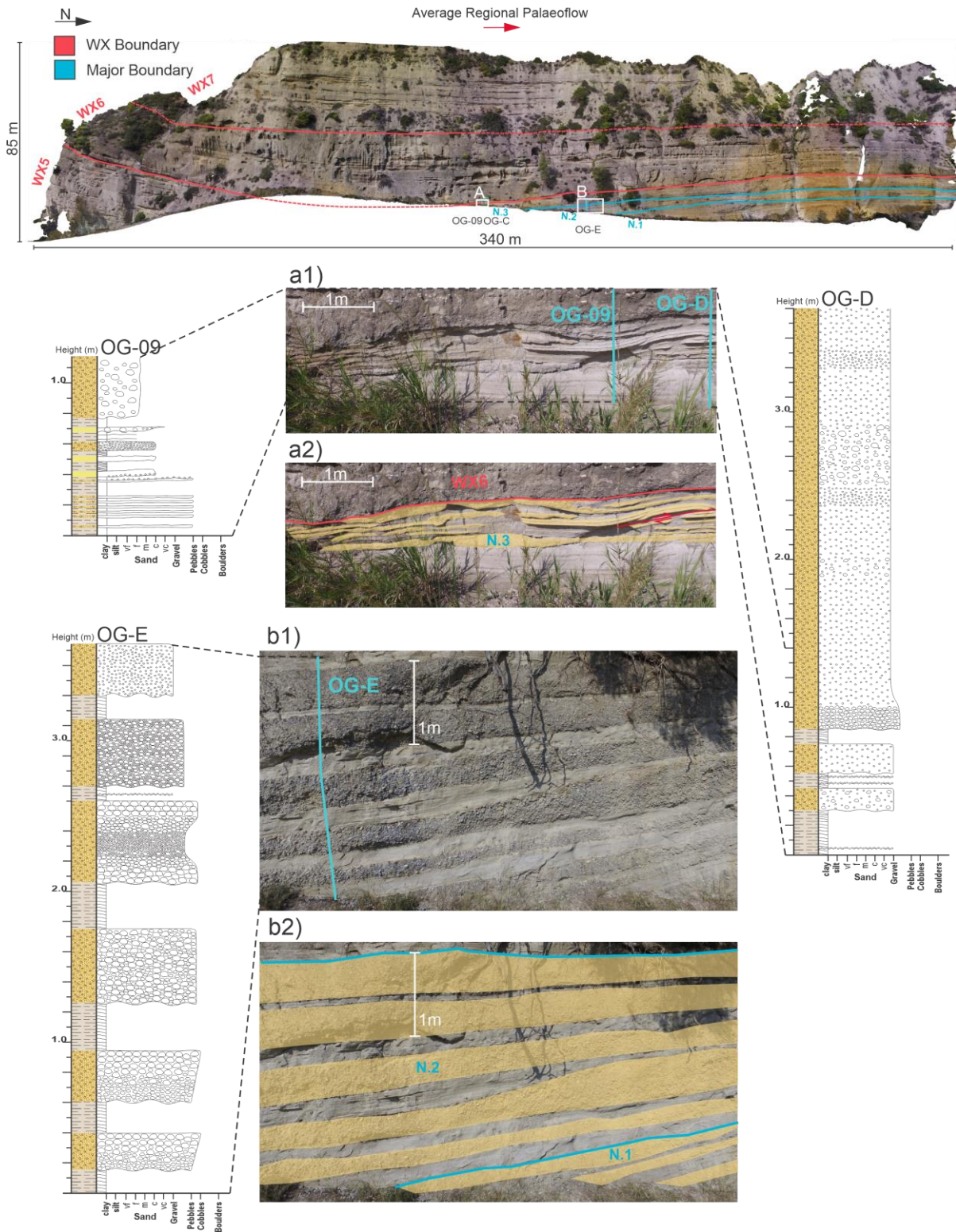
Figure 6. 4: Location a is marked with box A on the 'Olive grove' outcrop model and logs OG-09 and OG-D are marked with light blue line. a1) shows unit N.3 deposits. a2) gravelly conglomerate and coarse sandstone layers are mapped out with transparent orange colour, as well as a thrust fault with red line. Location of b is marked with box B on the 'Olive Grove' outcrop model and log OG-E is marked in light blue. b1) shows N.2 deposits of alternating mudstone and conglomerate layers. b2) conglomerate layers are mapped out with transparent orange colour. See legend Figure 6.3.
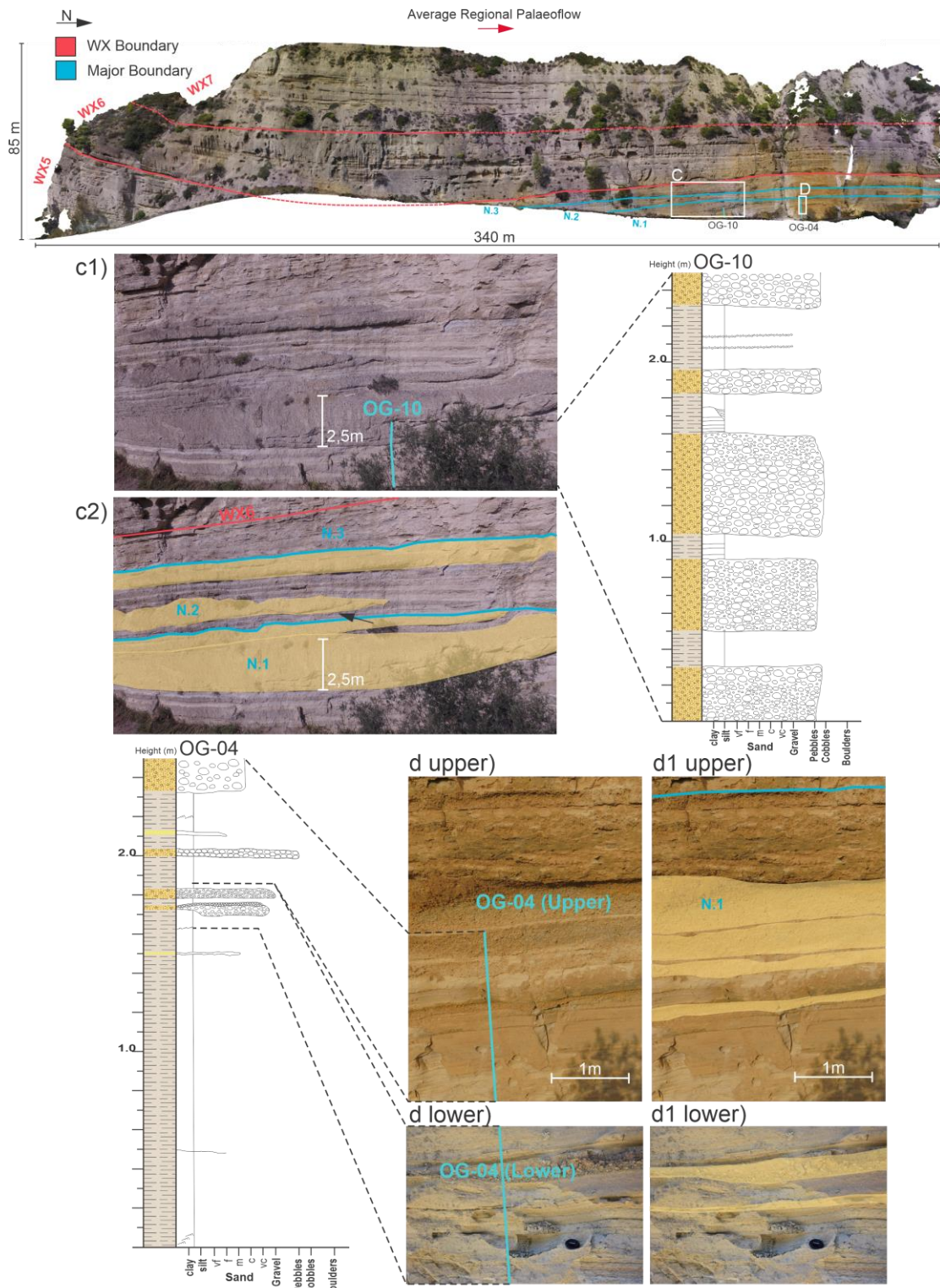
Figure 6. 5: Location of c is marked with box C on the 'Olive Grove' outcrop model, and log OG-10 is marked with light blue line. c1) show alternating layers of mudstones and lens shaped conglomerates within the N.1 and N.2 units, and log OG-10 is marked with light blue line. c2) thick lens shaped conglomerates showing backstepping stacking patterns are mapped out. d upper and lower) show alternating layers of conglomerate and mudstones in the northern part of Unit N.1, and log OG-04 is marked with light blue line. d1 upper and lower) conglomerate layers are mapped out with transparent orange colour. See legend Figure 6.3.

Statistics of the pinch and swell bed-scale geometries within the WX5 North unit have been measured for thicknesses and lengths. Thicknesses correspond to the observed maximum thickness, and the lengths correspond to the maximum length of an individual geometry. A Thickness-to-Length plot in Figure 6.6 shows the relationship of these measurements for the individual beds. Common thicknesses appear between 0,25 m – 0,75 m, whereas the most common lengths appear between 2,0 m – 7,0 m. The green dots on the plot corresponds to symmetrical pinch and swell geometries, and the pink dots corresponds to asymmetrical pinch and swell geometries. The symmetrical geometries measurements have a larger span of values, compared to the asymmetrical measurements which are more concentrated around thicknesses of ~ 0,5 m and lengths of ~5,0. The blue dashed line represents a trendline, where the R^2 value (~ 0,9) indicates a good correlation between all the respective pinch and swell measurements, hence a linear relationship.
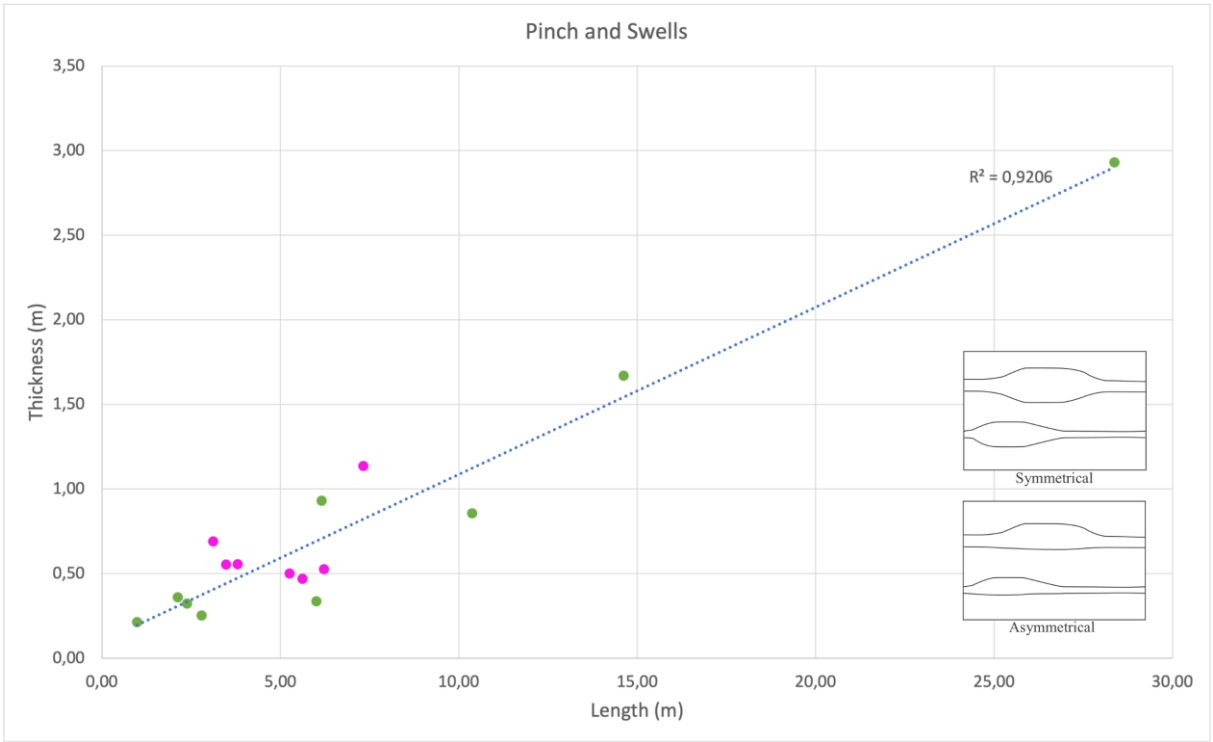
Figure 6. 6: Scatter plot of the pinch and swell geometry measurements within the WX5 North Unit, of maximum thicknesses plotted against maximum lengths. Green dots = symmetrical geometries, pink dots = Asymmetrical geometries, Blue dashed line = Trendline. The geometries of symmetrical and asymmetrical pinch and swells are illustrated in the bottom right corner.

WX6

Unit WX6 of the 'Olive Grove' outcrop is broadly horizontal with a gentle dip of 10° towards the North in the southernmost part, becoming obscured by vegetation to the right-hand side of the exposure. Unit WX6 is broadly composed of stacked and amalgamated conglomerates with crude, laterally non-extensive boundaries in the South, and the northern part is characterized by alternating beds of sandstones and conglomerates (Figure 6.7). The major and minor boundaries of the WX6 Unit mainly map out the most prominent boundaries between the amalgamated conglomerates in the South, which correlate to sandstone-conglomerate boundaries in the North (Figure 6.7). The conglomeratic layers in the South are generally massive and structureless, ranging from matrix- to clast supported. Grain size trends where present are variable, exposing both normal and inverse grading, and clasts are rounded to sub-rounded from gavel up to cobble sized. Additionally, layers composed of isolated clasts with outsized clasts are present (Figure 6.7 a and b), where some of these shows low angle, up-dipping fabrics and/ or imbrication (Figure 6.7 a). The northern part of the WX6 Unit is more sand-rich than the southern part and exposes alternating layers of sandstones and conglomerates (Figure 6.7 c). There are also rare thin (< 0,5 m thick) mudstones present in some parts throughout the WX6 Unit. The uppermost part of the WX6 Unit, is conglomeratic in the South but becomes highly obscured by vegetation towards the North, but where observation is possible, it is generally dominated by sandstones. The massive, amalgamated conglomerates in the southern part are interpreted to be deposited by debris flows (Gobo et al., 2014; Lowe, 1982; Talling et al., 2012). Some conglomeratic beds show continuity into overlying sandstone and mudstone layers and can be interpreted as the deposits of stratified, coarse-grained, high-density turbidity currents with low-density dilute wakes (Gobo et al., 2014; Lowe, 1982; Talling et al., 2012). The layers composed of isolated clasts are interpreted to be stacked, multiple debris fall deposits and granular flows (Gobo et al., 2014; Nemec, 1990). The more distal sand-prone deposits in the northern part are interpreted to be fringal equivalents of more conglomerate rich parts of lobate deposits up-dip, such as for the deposits in the northern part of the WX5 Unit (Deptuck et al., 2008).

Olive Grove WX6
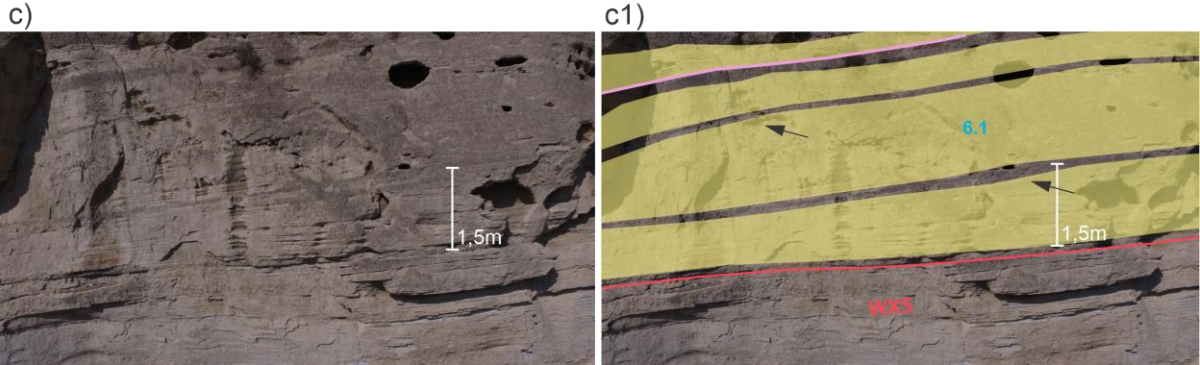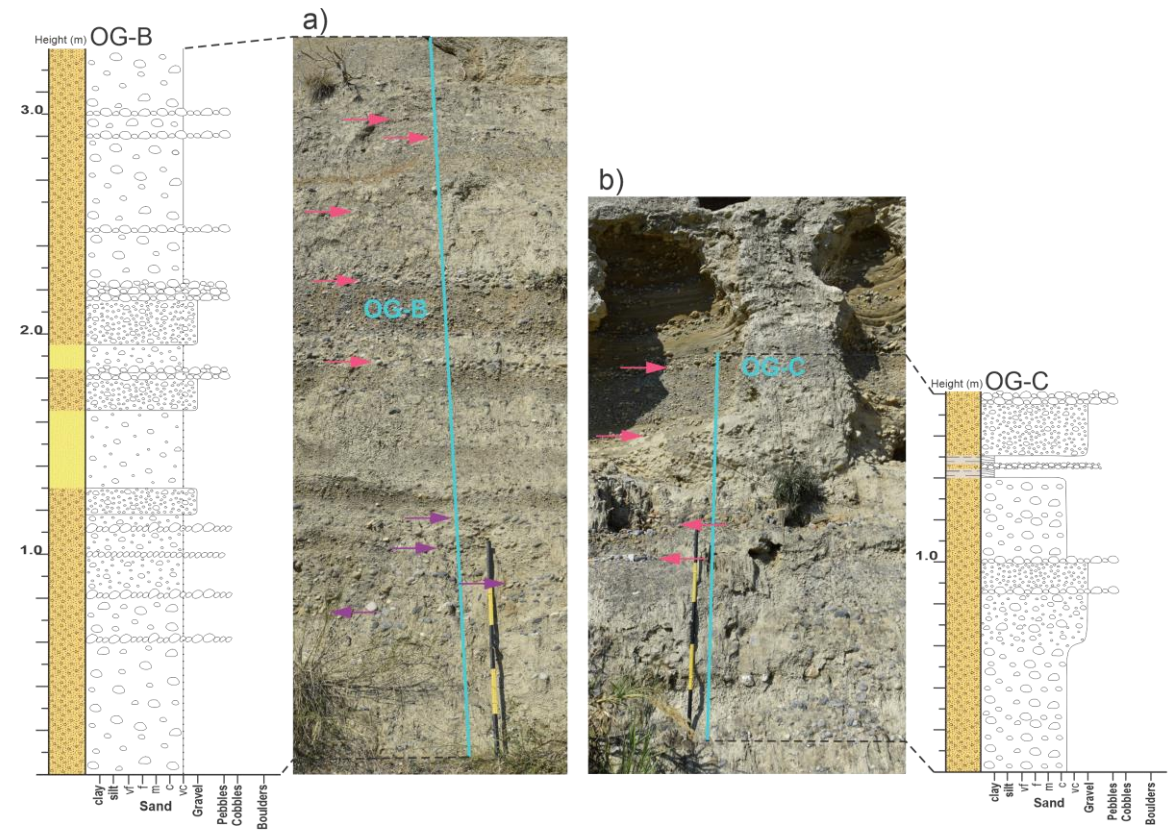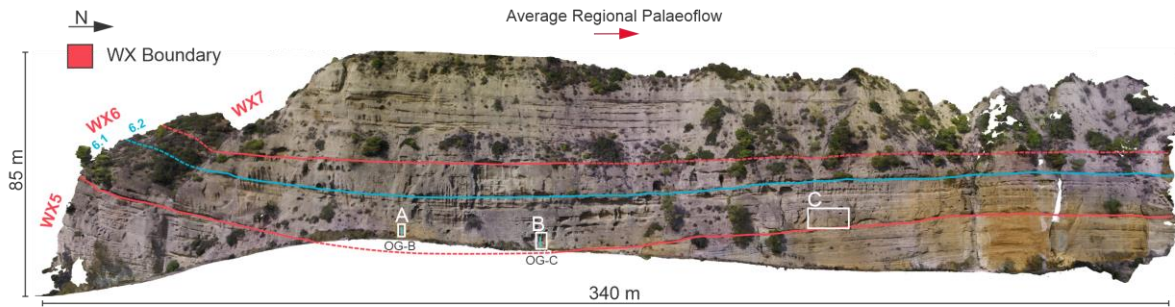
Figure 6. 7: a is marked with box A and b is marked with box B on the on the 'Olive Grove' outcrop model, and log OG-B and OG-C are marked with light blue line. a and b) Show conglomeratic deposits where single layers of clasts are marked with pink arrows, and single layers of clasts with low angle fabric/ imbrication is marked with purple arrows. c is marked with box C on the 'Olive Grove' outcrop model. c1) Show alternating layers of sandstones and conglomerates. c2) Sandstone beds are marked with transparent yellow colour. See legend Figure 6.3.

WX7

The WX7 unit of the 'Olive Grove' outcrop broadly has a horizontal layering of the beds and is composed of laterally extensive, sheet-like conglomerates with laterally discontinuous mudstone-caps on top, with stronger stratification upwards (Figure 6.8). The conglomerate beds often amalgamate into each-other and have typical bed thicknesses of 1- 2 m, while the overlying mudstone layers follows the stratigraphy and is typically 0,2 m thick. Major and Minor boundaries within the WX7 unit separate the various conglomerate beds. The conglomerate beds are interpreted to be laterally extensive lobate deposits, with more erosive boundaries compared to the lobate deposits in the northern part of units WX5 and WX6. The northern part of the WX7 unit is highly obscured by vegetation, and the stratigraphy in the area is therefore uncertain. However, the strongly weathered, and mud-wash rich exposure has led to the interpretation of this as a dominantly mudstone-rich package.

Olive Grove WX7
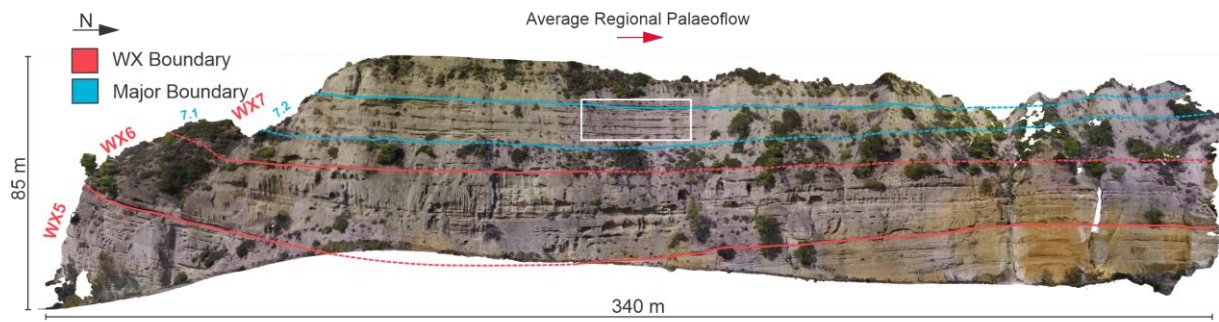
a)
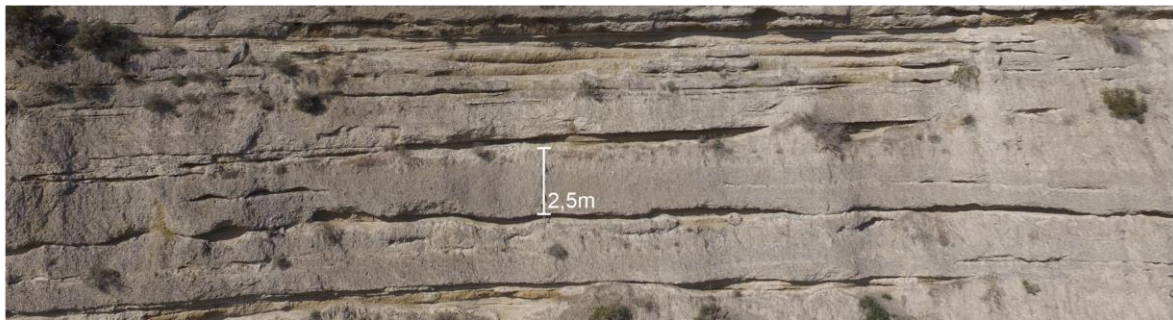
a1)
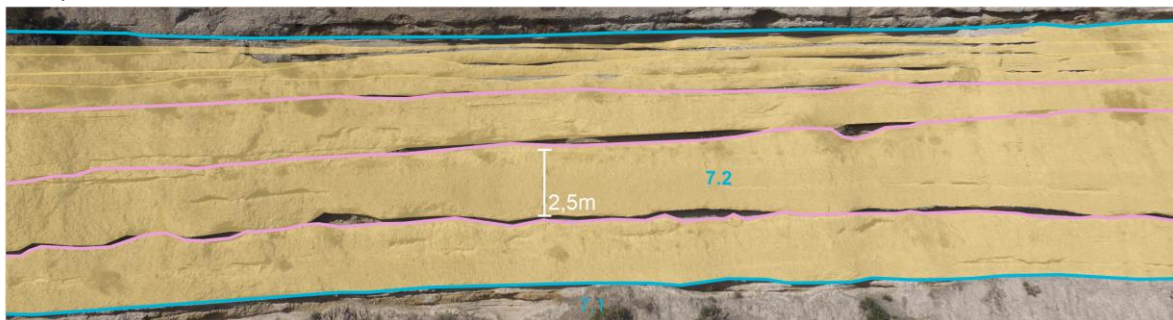
Figure 6. 8: a is marked with white box on the 'Olive grove' outcrop model. a) show laterally extensive conglomerate beds with mudstone cap on top. a1) Conglomerate beds are marked with orange transparent colour.

6.1.2 Stomio

The 'Stomio' outcrop exposes distal bottomset/ basin floor deposits fed by the Ilias delta, including the WX1-5 units (Cullen et al., 2020). The interpretations from a 3D virtual outcrop model to a geomodel of the 'Stomio' outcrop are presented in Figure 6.9. Overall, the outcrop is vertically heterogeneous with lateral continuity of distinct lithological packages at bed-set scales, however these are internally more complex. The stratigraphy is generally more sand- and mud-rich than the stratigraphy of the 'Olive Grove' outcrop (Figure 6.9 c). 'Stomio' pseudologs are attached in Appendix 4.
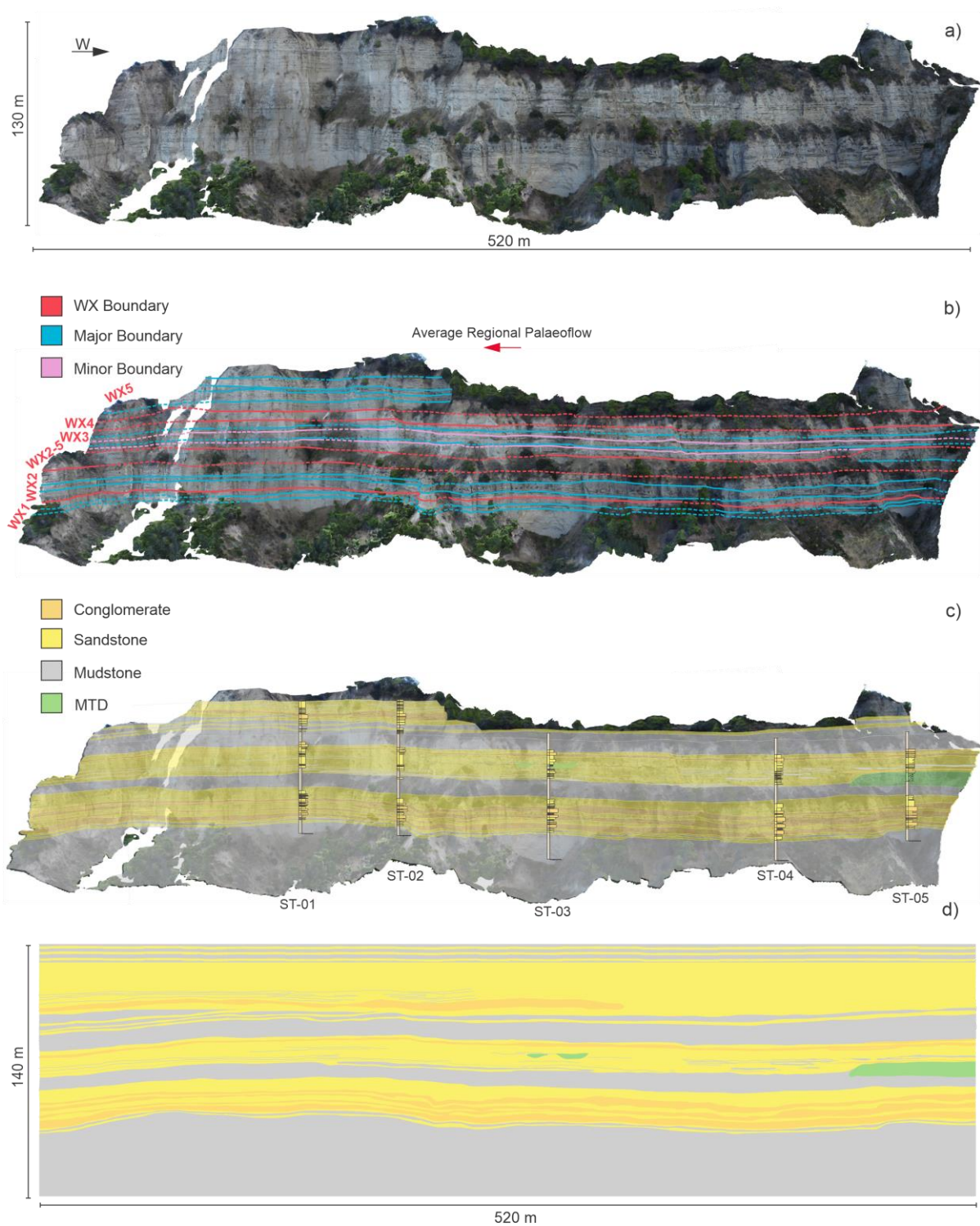
Figure 6. 9: a) The 'Stomio' outcrop with dimensions and North direction marked. b) Hierarchical interpretation with WX-, major- and minor boundaries marked, as well as average regional palaeoflow direction. c) Interpreted lithological units of the 'Olive Grove' outcrop model with overlain pseudologs. d) Complete geomodel with marked dimensions.

WX1

The WX1 unit in the 'Stomio' outcrop model is a broadly horizontal mudstone-dominated unit, with a few laterally extensive coarse-grained sandstone and conglomerate layers at the top (Figure 6.10 and Figure 6.11). The unit is sporadically obscured by vegetation and mud-wash. unit 1.1 is composed of an approximately 15 m thick mudstone package, unit 1.2 is composed of laterally extensive coarse-grained sandstone and mudstone layers with typical bed thicknesses of 1 m, and unit 1.3 mainly composed of conglomerates interbedded with a few mudstone layers with bed thicknesses ranging from 0,2 m to 3,0 m.

WX2

The WX2 unit in the 'Stomio' outcrop model is a broadly horizontal unit composed of complex mudstone-, sandstone- and conglomerate deposits (Figure 6.10). Unit 2.1 is composed of amalgamated sandstones, with typical thicknesses between 0,5 m to 1,5 m, interbedded with mudstones (< 0,5 m). Unit 2.2 is composed of massive conglomerates with lateral variability in bed thicknesses ranging from 0,5 m to 5,0 m in the upper and lower part, with heterolithic bedding of mudstones and sandstones in between. Unit 2.3 is composed of amalgamated sandstones interbedded with mudstones, with a couple of conglomerate beds towards the east. Within unit 2.3, the bed thicknesses of the sandstones and conglomerates vary laterally from 0,2 m to 2,5 m, and mudstones are typically less than 1 m. Based on the stacking pattern of both laterally extensive and discontinuous beds within WX2, the architectural elements are interpreted to be lobate deposits. The chaotic and massive nature of the conglomerate packages within unit 2.2 indicate deposition by debris flows. Figure 6.11 shows preserved cross-stratification within the conglomeratic layers of unit 2.2, which is interpreted to be deposited during a stage when a subaqueous debris flow starts to deposit *'en masse'* and continues to spill over at the edges forming a significant cross-stratificational pattern (Major and Iverson, 1999).

WX2-5

The WX2-5 unit in the 'Stomio' outcrop model is an additional WX-unit (~ 10 m thick) composed of mudstones, which is highly obscured by vegetation. In the western part of the outcrop, a chaotic package with little preservation of internal layering due to deformation is interpreted to be a mass-transport slump deposit (Figure 6.11)

Stomio WX1, WX2, WX5
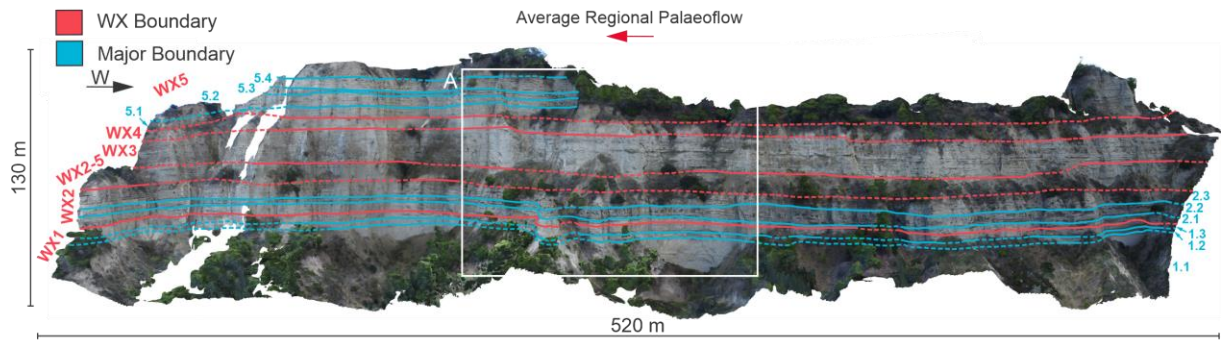
a)

a1)
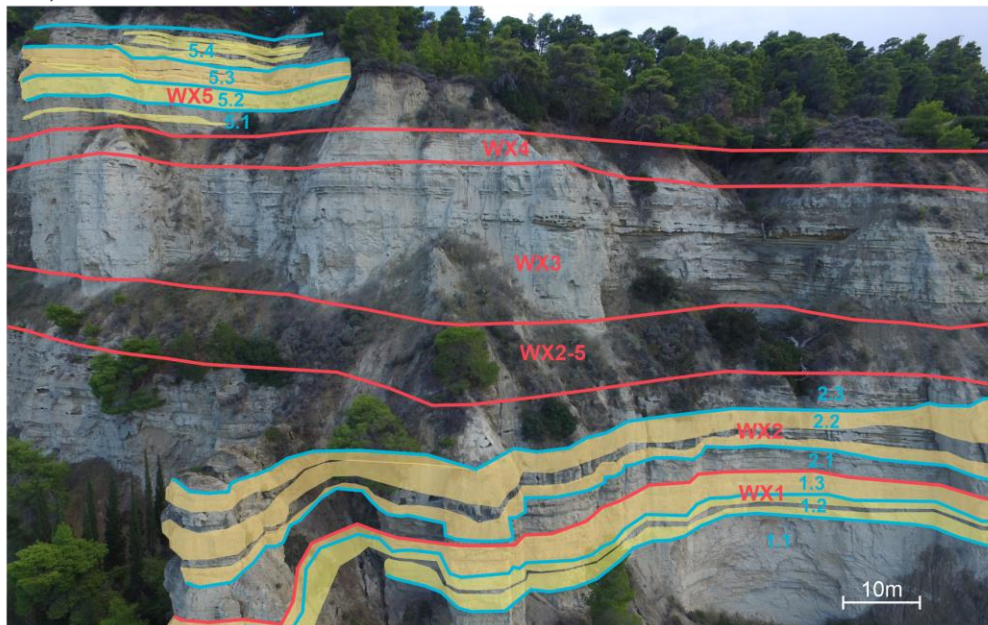
Figure 6. 10: Location of figure a is marked with white box on the 'Stomio' outcrop model. For the WX1 and WX5 units sandstone beds are marked with transparent yellow colour and conglomerate beds are marked with transparent orange colour. In the WX2 unit the distinctive conglomerate beds are mapped out.
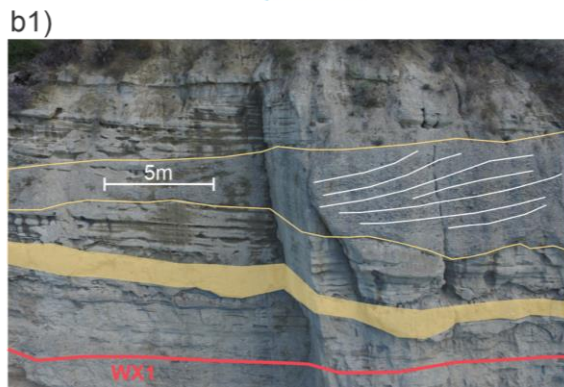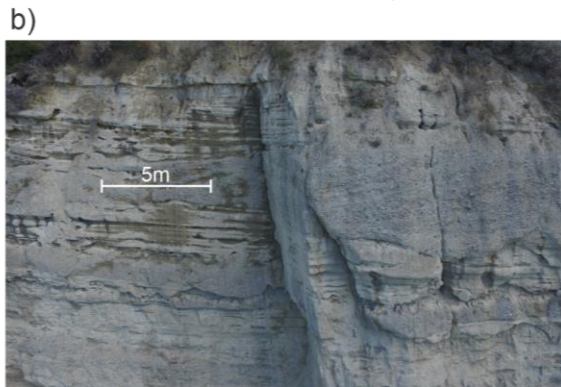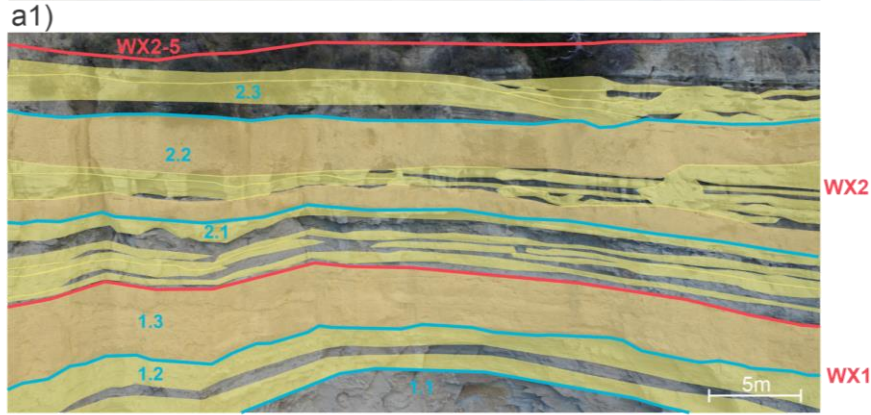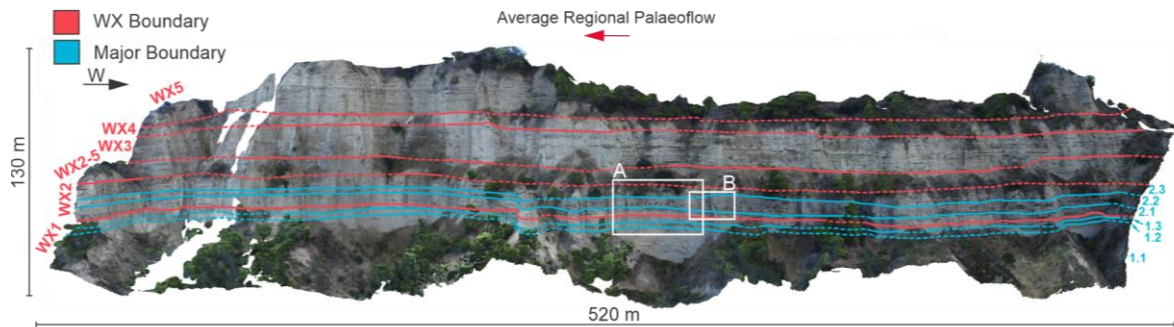
Figure 6. 11: Location of a is marked with box A on the 'Stomio' outcrop model. a) Display deposits of the WX1 and WX2 units where sandstone layers are mapped out with yellow transparent colour and conglomerate layers are mapped out with orange transparent colour. Location of b is marked with box B. b) Cross-stratification within the debrite deposits within unit WX2.

WX3

The WX3 unit is composed of a complex mix of conglomerates, sandstones, and mudstones with some localised mass-transport deposits. Overall, the unit is mainly dominated by both laterally continuous and amalgamated interbedded sandstones and mudstone packages, which internally host discontinuous lensoid sandstones interbedded with mudstones at the bed scale (Figure 6.12). Typical bed thicknesses are less than 0,5 m for mudstones and~ 1 m for sandstones. Unit 3.1 and 3.2 are both sandstone dominated, but 3.1 has a higher proportion of mudstones and 3.2 has some local mass-transport deposits that can be identified. Unit 3.3 has more conglomerate beds than the underlying 3.1 and 3.2 units. The conglomerates range in thicknesses from 0,5 m to 1,9 m. WX3 is interpreted to be lobate deposits with overall sheet-like architecture at the bed scale (Figure 6.12 a, and 6.13 a). In cross-sectional view, some more concave-up geometries can be displayed, indicating a more channelized environment (Cullen et al., 2021). The mass transport deposit in 6.12 b shows little internal deformation in the upper part and substantial sheet folding of layers in the lower part, indicating a spatially changing character between a slide and slump (Posamentier et al., 2011).

WX4

The WX4 unit is a mudstone-dominated unit (~ 10 m thick) highly obscured by vegetation (Figure 6.13). This unit is interpreted to be deposited by thin, dilute turbidity currents during a period of lower sediment supply linked to a major transgression (Cullen et al., 2021).

WX5

The WX5 unit within the 'Stomio' outcrop is only present in the easternmost part of the outcrop and is broadly horizontal. The unit is composed of heterolithic beds of conglomerates, sandstones, and mudstones (Figure 6.10). Unit 5.1 is mudstone-dominated, Unit 5.2 and 5.4 are sandstone dominated, and unit 5.3 is conglomerate dominated. Bed thicknesses are typically 0,5 m – 2 m for mudstones and sandstones and range from 1,0 m to 4,0 m for the conglomerates. Additionally, some layers are normal faulted with an offset of $\approx$ 2 m. The deposits of this unit are interpreted to be sheet-like sand/ gravel-rich lobate deposits (Deptuck et al., 2008).

Stomio WX2-5, WX3, WX4
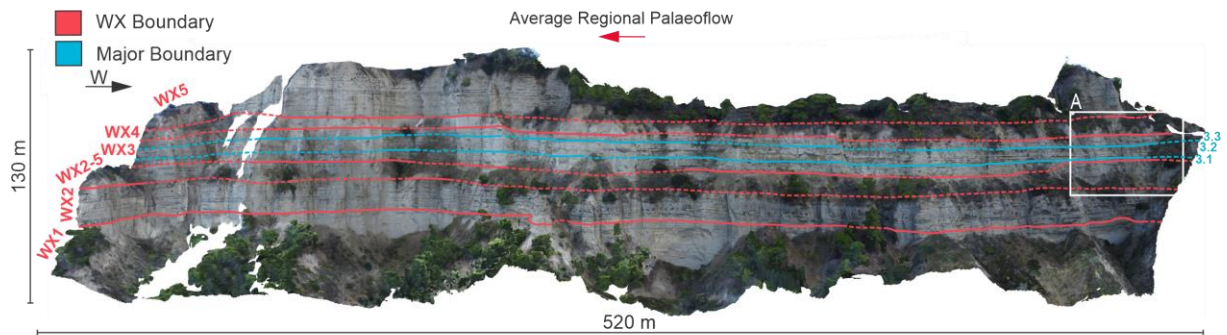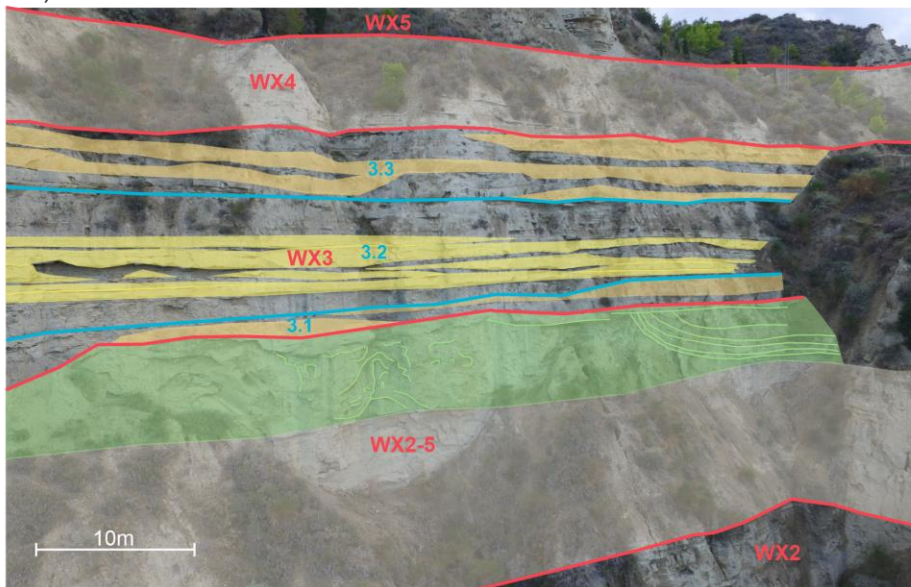
Figure 6. 12: Location of a is marked with a white box on the 'Stomio' outcrop model. The mudstone dominated WX2-5 and WX4 units are marked with transparent grey colour. The slump deposit within WX2-5 is marked with transparent green colour. Within the WX3 Uni, sandstone layers are marked with transparent yellow colour and conglomerate layers are marked with transparent orange colour.
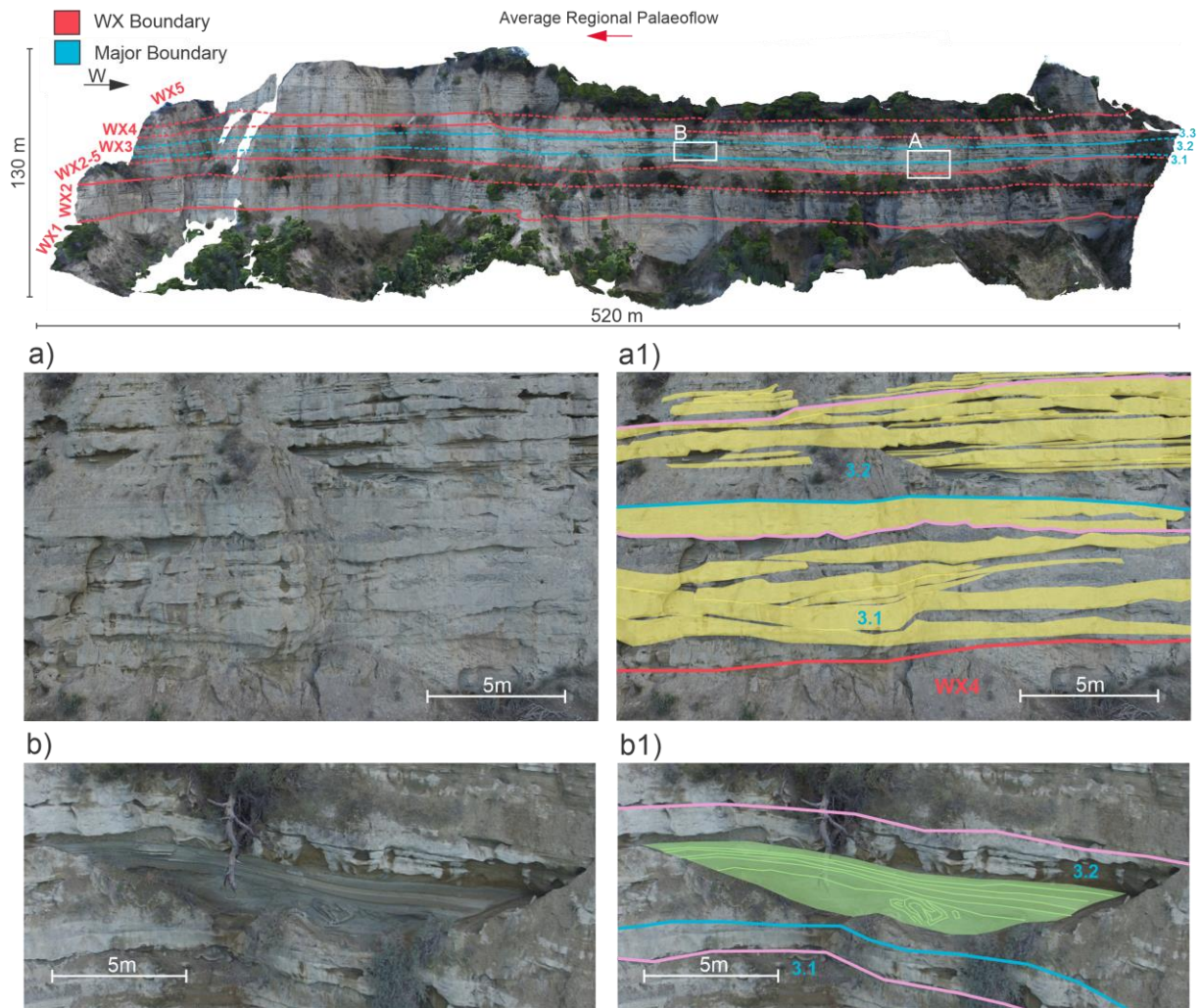
Figure 6. 13: a is marked with white box A on the 'Stomio' outcrop model. a) Complex sandstone layers within unit WX3 are mapped out with transparent yellow colour. b is marked with box B on the 'Stomio' outcrop model. b) Local mass-transport deposit within the WX3 unit is marked with transparent light green colour.

6.2 Seismic Modelling

The 2D synthetic seismic images were generated through the PSF-based convolution modelling method (described in Chapter 4) that provides the possibility of changing various geophysical parameters, including frequency content, illumination angle, and incident angle (Lecomte et al., 2015; Lecomte et al., 2016). By changing the properties of these geophysical parameters, it is possible to investigate their prominent effects on the generated seismic images, as well as the controls on the seismic signature of the architectural and lithological elements. The outcrop models used in this study are composed of features that would, in many instances, be considered to be below seismic resolution (i.e., below λ/4 or so), but it is still important to consider their effect on the generated seismic and to what degree they can or cannot be resolved. The following section outlines the seismic results obtained by changing the dominant frequency, illumination angle, and incident angle. In addition, the effect of adding various levels of noise to the seismic images has been investigated. Two property models were generated for each of the geomodels, i.e., for wells 6406/12-3 B and -S (further referred to as well B and well S). For the ease of comparison between the seismic images, all seismic sections have been amplitude-calibrated and are presented together with their respective PSF, reflectivity- and geomodel. The most representative seismic images that illustrate the effects of the various geophysical parameters are presented in this thesis.

6.2.1 Dominant Frequency

The frequency content controls the shape of a wavelet and affects the resolution of seismic images (Simm and Bacon, 2014). There is a span of idealised wavelets (e.g., Butterwoth, Ricker, Ormsby) used for seismic modelling approaches (Simm and Bacon, 2014); in the present work, the Ricker wavelet has been systematically used as done in most modelling studies and because of its simple relation between dominant frequency and wavelet breadth (c.f, Ryan, 1994). With depth, the high-frequency components of a wavelet are typically attenuated. The dominant frequencies used in this thesis are 20 Hz, 40 Hz, 60 Hz and 140 Hz. Where the 20 Hz and 40 Hz corresponds to resolution of conventional seismic, and 60 Hz are more typical of high-resolution seismic (Reiser et al., 2012). Additionally, the 140 Hz is the average dominant frequency of the shallow seismic acquired in the Gulf of Corinth, Greece (Beckers et al., 2018; R. Gawthorpe 2022, personal communication).

The geomodels modelled with the dominant frequencies mentioned above were the 'cross-sectional' and 'Stomio' models, while the 'Olive Grove' has only been modelled with the 140 Hz. The maximum illumination angle was in all cases set to 45°, which is a common seismic illumination (Simm and Bacon, 2014). The incident angle was set to an intermediate angle of 20°, representative for long-offset conventional seismic data (Faleide et al., 2021). Additionally, the average velocity used to generate the PSF is 4 km/s, which accounts for the selected velocities in the considered targets.

For both the 'cross-sectional' (Figure 6.14) and the 'Stomio' (Figure 6.15) models, the reflections have stronger amplitudes and more details are detected in the seismic images generated from well B than well S. All seismic images of the 'cross-section' geomodel are scaled with a vertical exaggeration (VE) of 5, and the corresponding PSFs are plotted accordingly. For the 'cross-section', all seismic images have relatively strong, negative, and continuous reflections in the transition of the upper thick mudstone unit to the underlying sandstone and conglomerate unit. For well S, this reflection gets weaker towards the right in the transition zone of the underlying layer from alternating sandstones and conglomerates to massive sandstones. Mudstone layers below the thick sandstone and conglomerate unit generate a strong reflection on both sides of the fault. For the 20-Hz scenario, only the most prominent layers can be detected and laterally extensive conglomerates in the uppermost sand-rich unit cannot be identified. The smaller features to the left generate variability in the seismic response in terms of discontinuous positive and negative reflections, but their geometries cannot be resolved. For the 40-Hz scenario more details are imaged in the seismic, and a higher amount of geometries can be identified. The contours of the lateral extensive conglomerates and some of the concave-up geometries to the left are resolved, but the latter one mainly accounts for well S. The heterolithic layers of mudstones, sandstones and conglomerates to the lower right are generating more reflections, but all the single beds cannot be distinguished from each other. The 60-Hz scenario resolves even more of the distinctive geometries, whereas the concave-up geometries to the left are resolved for well B. It is also possible to distinguish more of the single beds of the laterally extensive conglomerates and the heterolithic bedding to the lower right.

The much-smaller scale yet detailed 'Stomio' geomodel yields seismic images difficult to interpret. In the 20-Hz scenario only five strong laterally extensive reflections are generated for well B. For well S, five relatively weak, laterally extensive reflections are generated with a sudden increase in seismic-amplitude strength to the right where the slump deposit of unit WX2-5 is located. For the 40-Hz scenario an increase of continuous strong reflections is generated for well B, with some internal variations of amplitude strength of the individual reflections. For well S, the slump deposit within unit WX2-5 generates a structural fault feature. The strong negative reflection generated between the sand-rich WX-3 and the underlying slump deposit can be connected to the strong negative reflection generated between WX-3 and the mud-rich part of the WX2-5 unit. For the 60-Hz scenario, more laterally continuous reflections are generated for the Well B seismic image, but with even more lateral variations of amplitude strength within the individual reflections, which is especially prominent within the WX5 unit (Figure 6.15). For well S, there is a higher proportion of laterally continuous reflections with a higher amplitude strength, and the slump deposit generate an increase in amplitude strength.
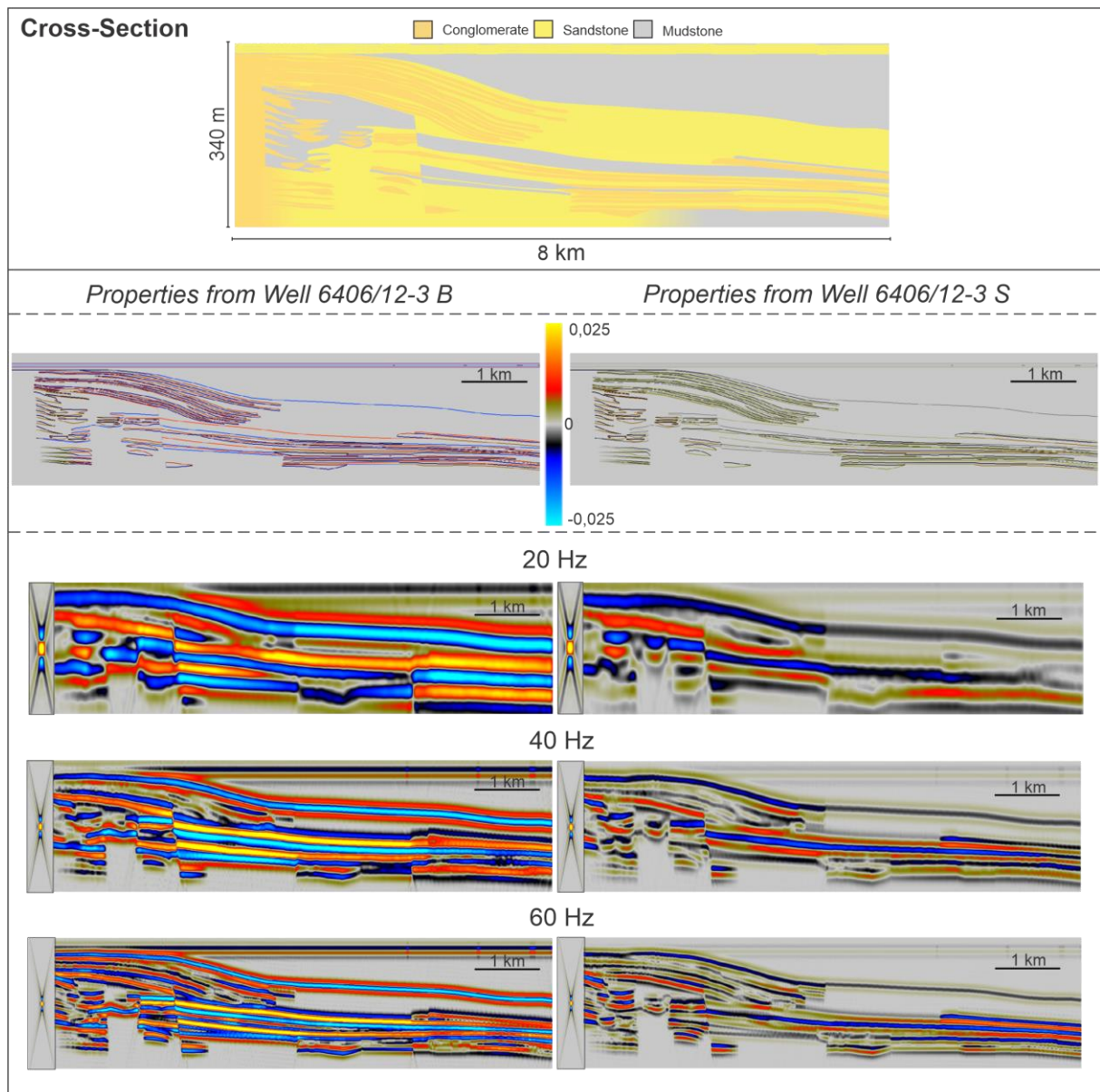
Figure 6. 14: Seismic images generated for the 20-Hz, 40-Hz, and 60-Hz scenarios from the 'cross-sectional' geomodel for both well B and -S. Respective reflectivity models are included, as well as PSFs are overlain on the seismic images.
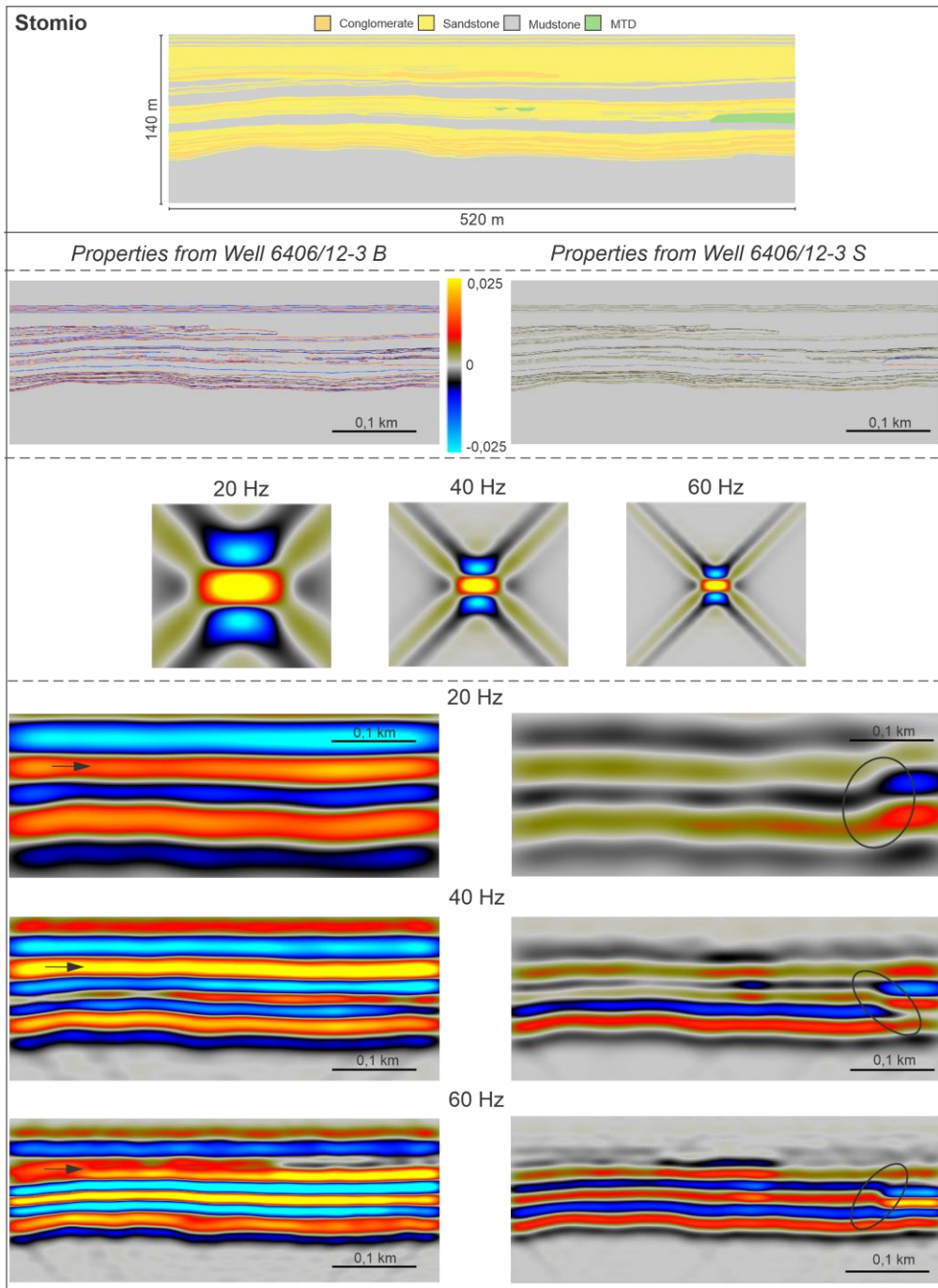
Figure 6. 15: Seismic images generated for the 20-Hz, 40-Hz, and 60-Hz scenarios from the 'Stomio' geomodel for both well B and -S. Respective reflectivity models are included, as well as PSFs are overlain on the seismic images. The lateral amplitude variations for the different scenarios of Well B are marked with black arrows. For well S, the black circle for 20 Hz marks the increase in amplitude, for 40 Hz it marks the generated structural fault feature, and for 60 Hz the circle marks the high amplitude generated by the slump deposit.

The 140-Hz scenario generally generates high amplitude reflections where several detailed geometrical features can be identified (Figure 6.16). For the 'cross-sectional' geomodel, both for well B and -S, virtually all the geological features can be identified. The seismic images generated for the smaller scale 'Stomio' and 'Olive Grove' geomodels expose more details, but not all geological features are resolved. Which features being resolved also varies for the different wells, especially for the 'Stomio' geomodel. The seismic image generated for well B of 'Stomio' displays more lateral variability, especially within the complex WX3 unit and the WX2 unit where the contours of the distinctive conglomeratic lobes can be identified. The mud-dominated WX2-5 unit still generates a continuous reflectivity with some lateral variability of amplitude strength. On the seismic image generated for well S of 'Stomio' the mass-transport deposits generate high-amplitude reflections compared to the surrounding seismic response. For the 'Olive Grove' model it is possible to identify the contours of the sandy lobate deposits within unit WX6 and the erosive lobate deposits within unit WX7. In the lower-left corner within the WX5 unit the thin mudstone layers cannot be detected, however, some amplitude variations are imaged in the seismic.

To summarize, higher frequencies increase the resolution of the seismic images, and a higher proportion of the geological features can be resolved, as expected. The scale of the geological features comprises a substantial impact. Considering the 140-Hz scenario, all features could be resolved for the 'cross-section', in contrast to the 'Stomio' and 'Geomodel' where some features still could not be resolved. This can be seen from the size of the PSFs overlain on the seismic images: that the larger the PSF is compared to the size of the geomodel the less features can be detected. However, even though some very small-scale features cannot be detected, they can still impact the amplitude strength within a seismic reflection. In addition, the properties of the various layers, yielding various reflectivity ranges, impact the seismic response, as exemplified here by the different seismic signatures between the images obtained when using properties from either well B or -S.

Figure 6. 16: Seismic images generated for the 140-Hz scenario from the 'cross-section', 'Stomio' and 'Olive Grove' geomodel for both well B and -S. Respective reflectivity models are included, as well as PSFs are overlain on the seismic images. 'Cross-section': Black arrows marks how well the concave up geometries are exposed for both Well B and -S. 'Stomio': Well B – black arrows mark lateral variations of the reflections within unit WX3, green arrow marks the strong continuous reflection generated by the mud-rich WX2-5 unit, and red arrow marks the conglomerate lobate deposits (negative reflections) within the WX2 unit. Well S: Black arrow marks strong reflection generated by small mass-transport deposits, and red arrow marks strong reflections generated by the slump deposit. Olive Grove: Green arrow marks reflections generated by conglomerate deposits within unit WX7, black arrow marks sandy lobate deposits within unit WX6, and red arrow marks the WX5 unit interbedded with mudstones generating amplitude variations in the seismic response. Note that the PSF is not vertically exaggerated for the 'cross-Section'.

6.2.2 Maximum Illumination Angle

The illumination angle controls the portion of seismic reflectors that can be recorded (illuminated) by a seismic survey (Herron, 2011), also affecting the lateral resolution of the seismic images; it is especially important for the direct imaging of steep features such as faults. In the PSF-based convolution modelling the illumination angle is controlled by the vector span (I_{SR}) described in Chapter 4. However, the geological features of the three geomodels used in this study generally have low dip-angle features. Hence, the main aim of investigating the impact of the maximum illumination angle in this study is to evaluate its effect on the lateral resolution.

The maximum illumination angles applied in this study are low to intermediate, including 10°, 20° and 45° for the 'cross-sectional' geomodel. The set associated parameters are a dominant frequency of 20 Hz and an incident angle of 20°. The illumination angle effect was chosen to be shown for the 'cross-sectional' model, since it had the same effects on all geomodels, but were better illustrated in this model due to its larger scale.

The results of the maximum illumination angle study are shown in Figure 6.17. In general, the various geological features are all being imaged for the 10°, 20° and 45° scenarios, but there is a lateral smoothness effect caused when decreasing the maximum illumination angle. The set angles for the maximum illumination angle are reflected in the shape of the PSF overlain on all the seismic images. All the distinct small-scale geological features to the right of the 'cross-section' geomodel are being imaged as more continuous reflections when the maximum illumination angle is set to 10° and 20°. In the 45° scenario, the distinctive geological features are imaged as more discontinuous reflections. Considering the seismic response of steep features, the minor intra-basinal fault within the 'cross-section' is also better resolved for the 45° scenario, compared to the 10° and 20° scenarios where the reflections are displayed more continuously.
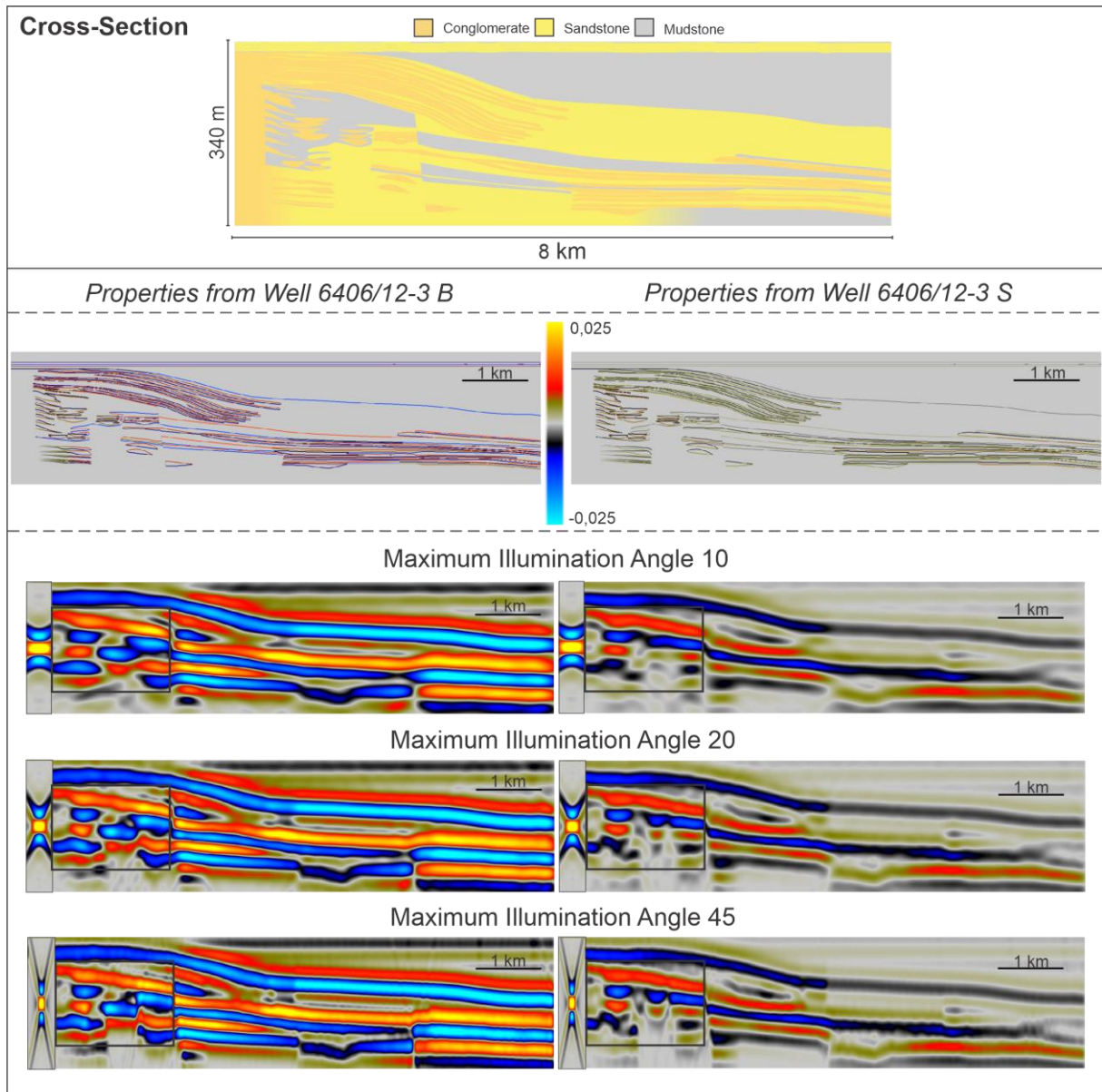
Figure 6. 17: Seismic images generated for the 10°, 20° and 45° maximum illumination angle scenarios from the 'cross-section' geomodel for both well B and -S. Respective reflectivity models are in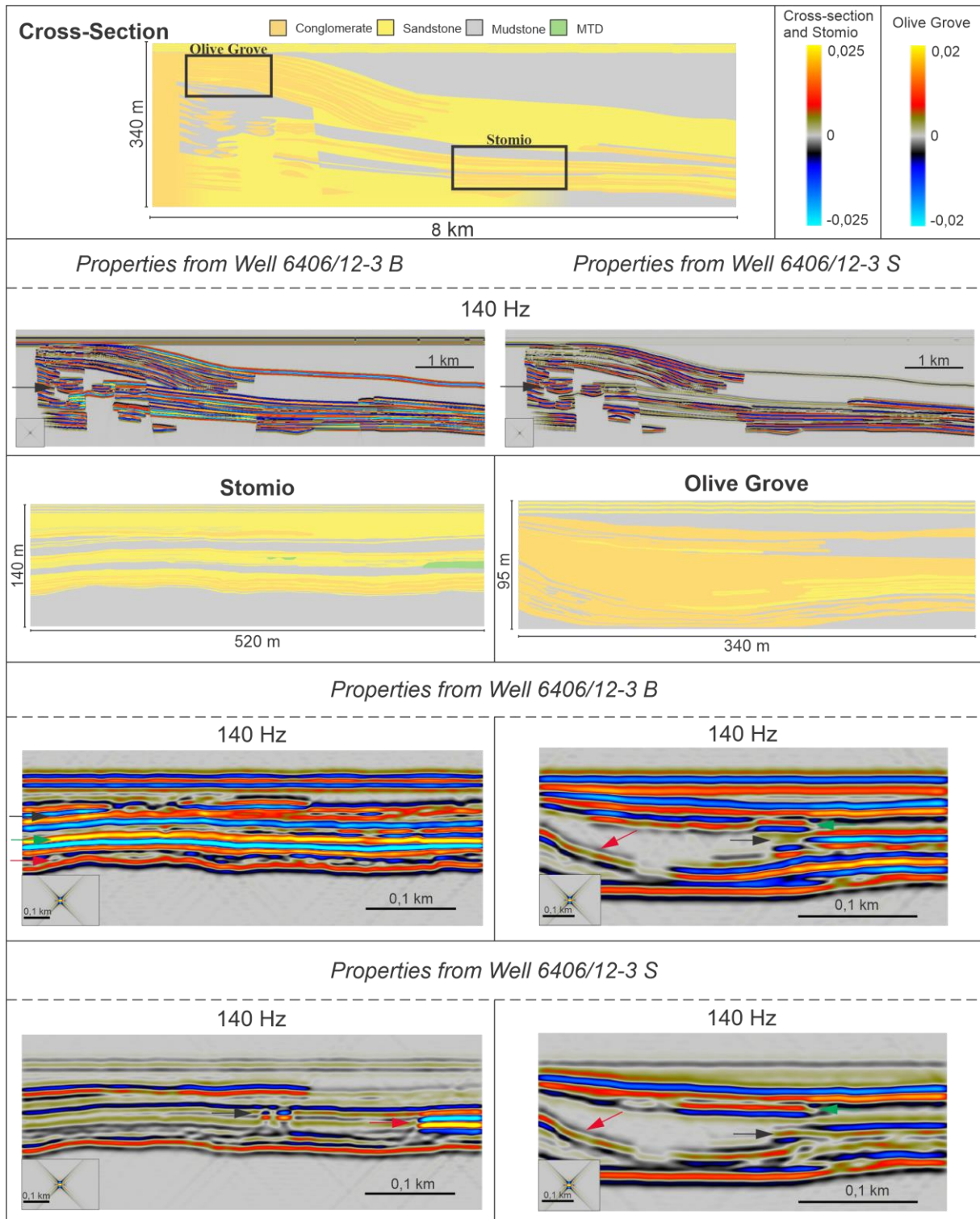cluded, as well as PSFs are overlain on the seismic images. The lateral smoothness effect of the smaller geological features is marked with the black box.

6.2.3 Incident Angle

The incident angle affects the reflectivity of a target and the resolution of seismic images. The incident angle is indeed one of the parameters that define the generic I_{SR} spans used in the seismic modelling approach to generate a PSF, directly affecting the length of each I_{SR} (Lecomte et al., 2016). In this thesis, the effects of incident angles of 0°, 10°, 20° and 30° are investigated for the 'Olive Grove' and 'cross-section' geomodels as simple proxies of "near-", "near-mid", "mid-" and "far-angle" stack in actual seismic, i.e., representing the offset variations in a seismic survey. The frequency was set to 40 Hz for the 'cross-section' and 20 Hz for 'Olive Grove', and the illumination angle was set to 45°. Below all the single incident-angle results, a seismic image generated from the sum of the various scenarios is included, potentially representative for a "full-stack" seismic image.

The reflectivity and resolution of the 'cross-section' and 'Olive Grove' geomodels are affected by changing the incident angle. For the 'cross-section', the geological features on the left side and the heterolithic beds on the lower right side were the most affected. With an increased incident angle, the reflectivity got stronger for well B (Figure 6.18). Generally, 0° and 10° are characterized by strong reflections and 20° and 30° are characterized by intermediate reflections. For well S, the reflectivity strength and resolution broadly decrease with increased incident angles (Figure 6.19). Generally, 0° and 10° are characterized by intermediate reflections and 20° and 30° are characterized by strong reflections. A zoomed in section of the left side for well S shows the effects on the geological features, where the amplitude strength decreases with higher incident angles (Figure 6.20).

The same trends for the 'Olive Grove' geomodel can be seen for the reflectors and reflectivity compared to the 'cross-section''. It is mainly the southern (left) WX5 unit, composed of conglomerates interbedded with mudstones, that is affected by the incident angle changes (Figure 6.21 and 6.22). Overall, the reflector strength increases with increased incident angle, except in the 30° incident angle for well S where the reflector strength decreases. The 'Olive Grove' model only generates two reflections when modelled with 20 Hz: a negative reflection with an underlying positive reflection. These reflections are highly affected by the changes of the incident angle. For well B, the reflections are almost absent with an incident angle of 0° and 10°, but strong reflections are generated with 20° and 30°. In the seismic images for well S, strong reflections are generated with 0° and 10°. The seismic images with 20° and 30° expose

intermediate reflections, but in the 30° scenario the positive reflection is overlying the negative. The reflectors generated from the lobate sandy deposits within the WX6 unit decrease with increased incident angles for well S, imaging strong reflections for 0° and very weak reflections for 30°. A zoomed-in section of the southern (left) WX5 unit is shown in Figure 6.23, illustrating how the reflector- and reflection strength decrease with increased incident angles.

To summarize, by changing the incident angle the reflectivity model and seismic resolution will get affected. Whether if the reflectivity strength increases or decreases with higher incident angles is dependent on the local elastic properties. The resolution itself decreases when the incident angle increases. The results from well B and -S illustrates how the velocity and density properties of a target will be important factors on how the incident angle affects the resulting seismic images.
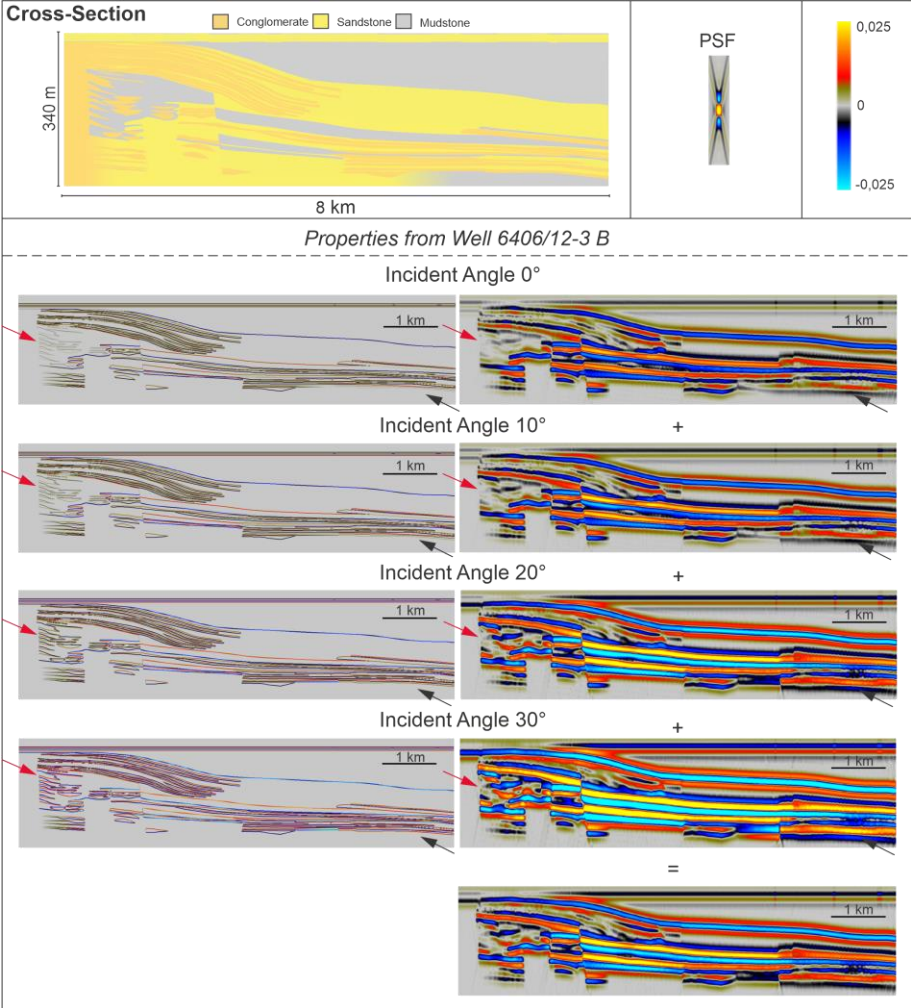
Figure 6. 18: Seismic images generated for the 0°, 10°, 20° and 30° incident angle scenarios from the 'cross-section' geomodel for well B. Respective reflectivity models and PSFs are included. The red arrow marks the area of where the seismic reflectivity and reflectivity strength increases for the geological features to the left with increased incident angle. The black arrow marks the same for the heterolithic layers to the right.
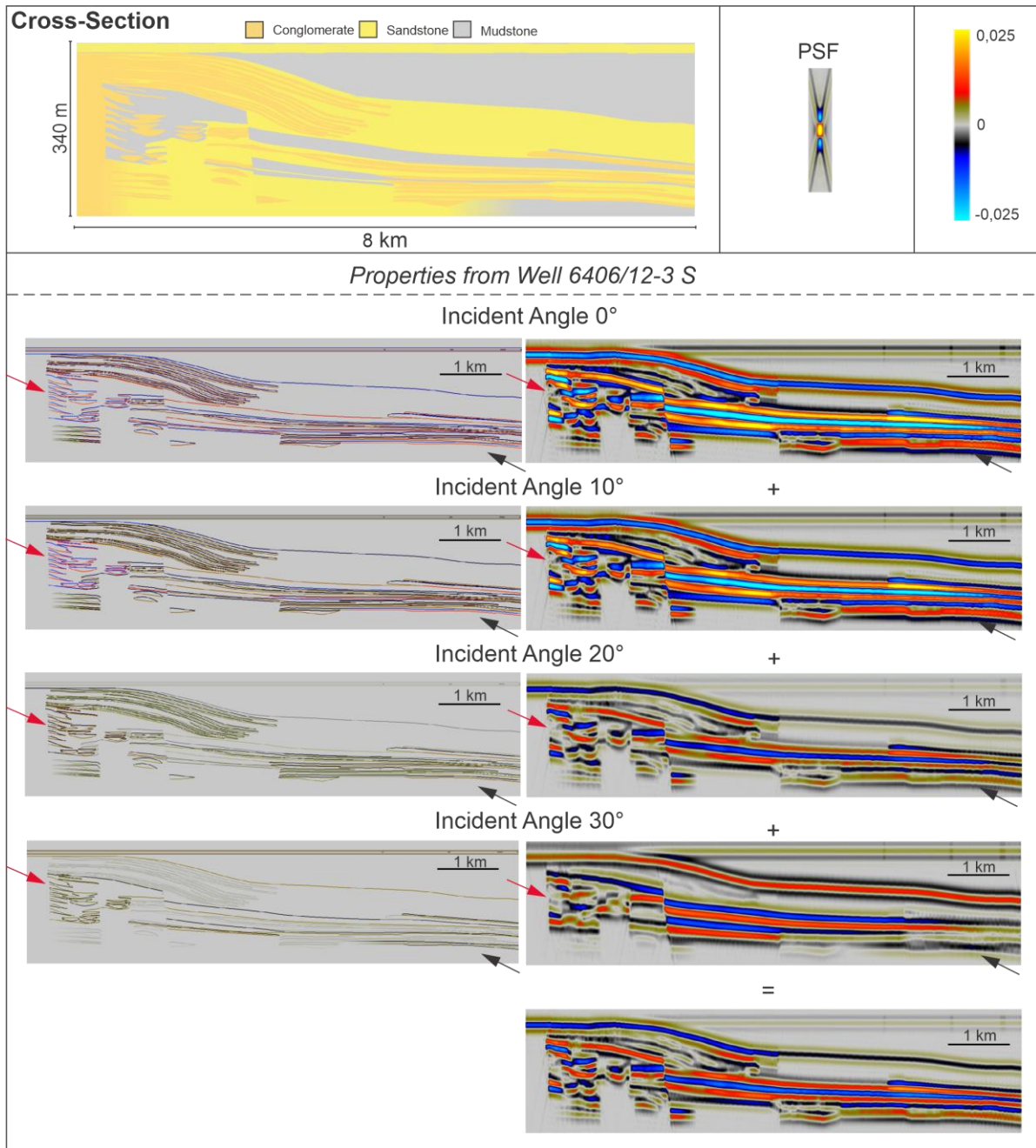
Figure 6. 19: Seismic images generated for the 0°, 10°, 20° and 30° incident angle scenarios from the 'cross-section' geomodel for well S. Respective reflectivity models and PSFs are included. The red arrows mark the area of where the seismic reflector and reflectivity strength decreases for the geological features to the left with increased incident angle. The black arrow marks the same for the heterolithic layers to the right.
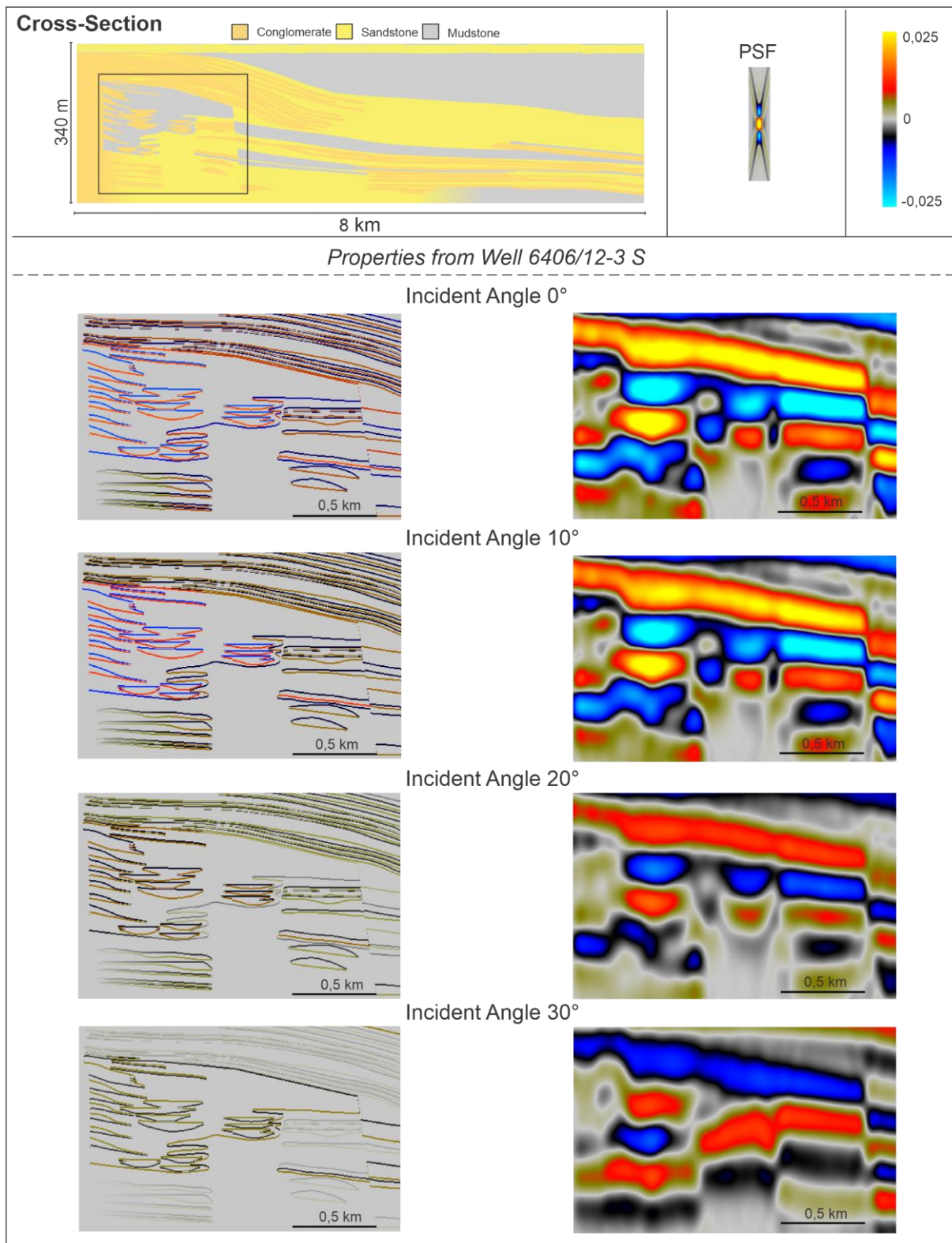
Figure 6. 20: Zoomed seismic images generated for the 0°, 10°, 20° and 30° incident angle scenarios from the 'cross-section' geomodel for well S, marked with a black box on the geomodel.
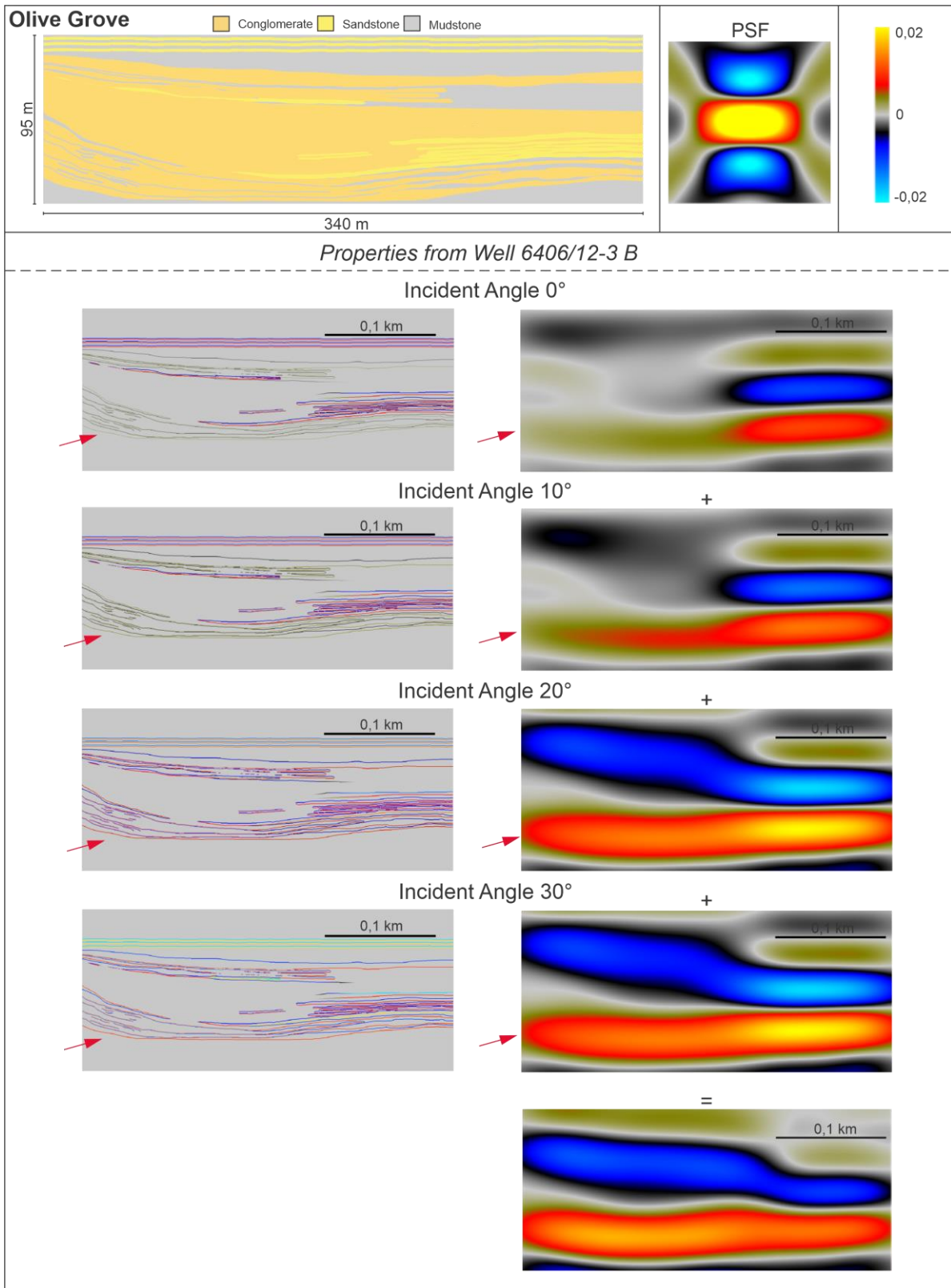
Figure 6. 21: Seismic images generated for the 0°, 10°, 20° and 30° incident angle scenarios from the 'Olive Grove' geomodel for well B. Respective reflectivity models and PSFs are included. The red arrow marks the area of where the reflector and reflectivity strength decrease for the geological features to the left within the WX5 unit.
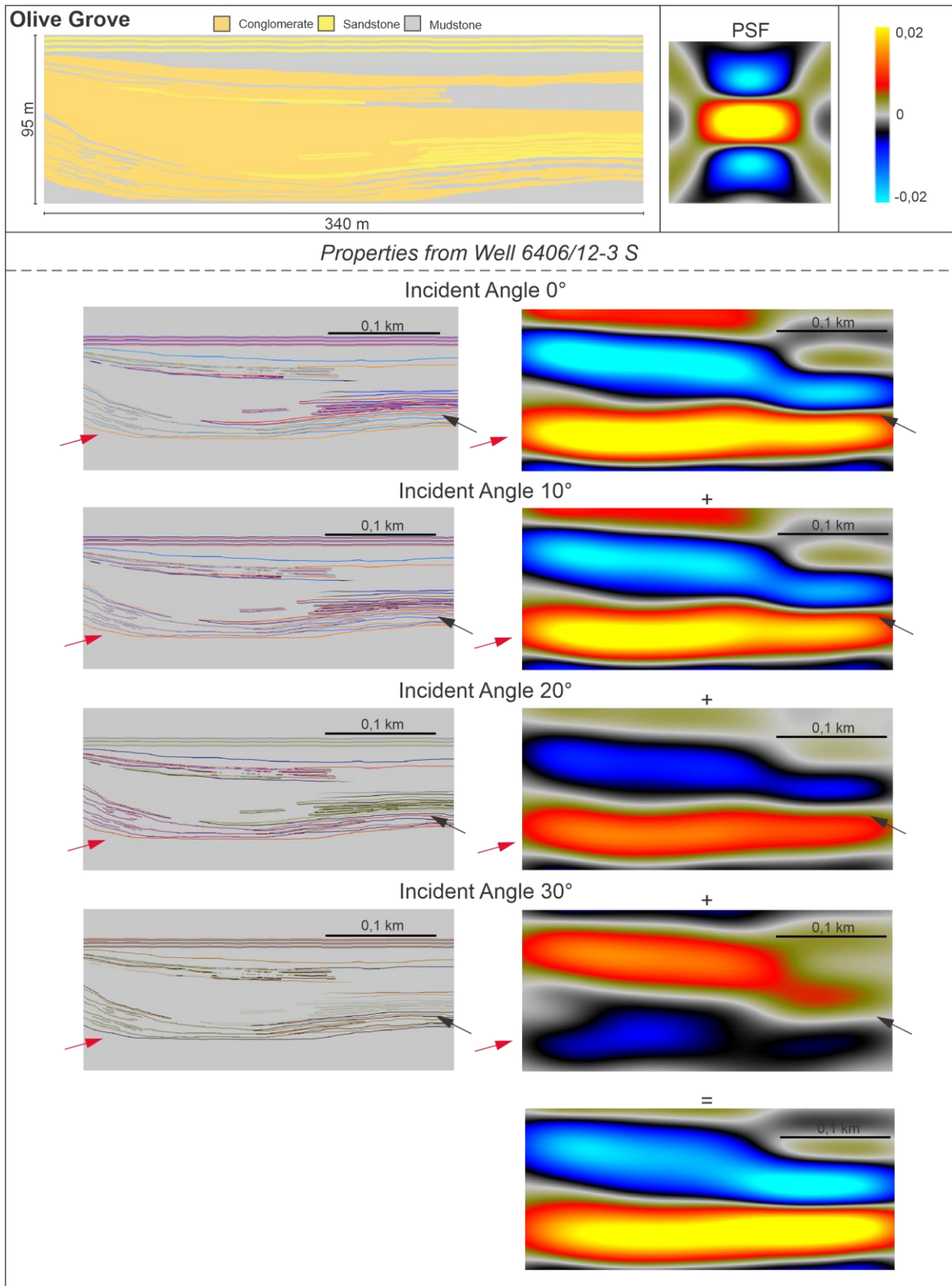
Figure 6. 22: Seismic images generated for the 0°, 10°, 20° and 30° incident angle scenarios from the 'Olive Grove' geomodel for well S. Respective reflectivity models and PSFs are included. The red arrow marks the area of where the reflector and reflectivity strength decrease for the geological features to the left of within the WX5 unit. The black arrow marks the area of where the reflector and reflectivity strength decreasefor the sandy lobate deposits within WX6 unit.
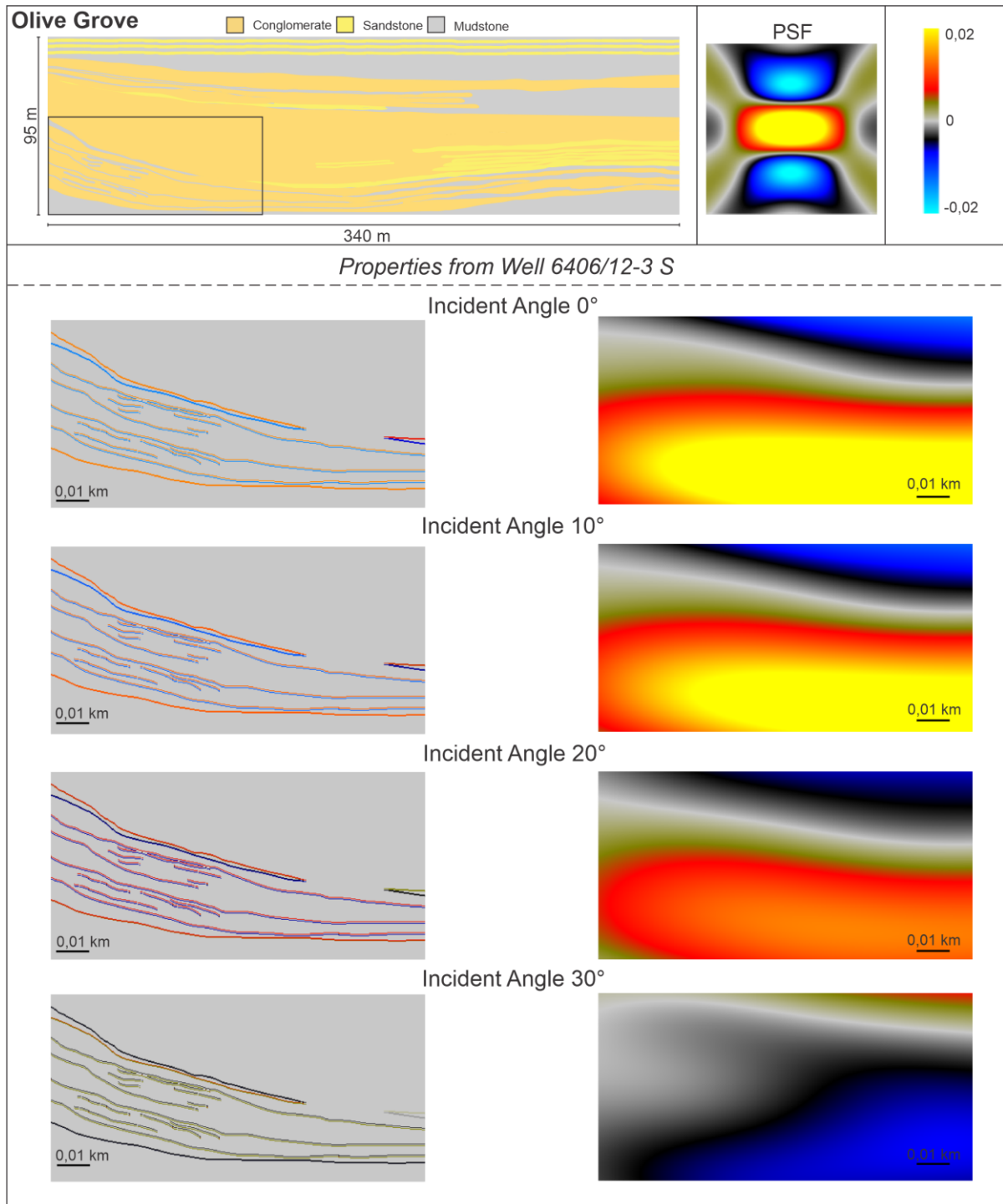
Figure 6. 23: Zoomed seismic images generated for the 0°, 10°, 20° and 30° incident angle scenarios from the 'Olive Grove' geomodel for well S, marked with a black box on the geomodel.

6.3.4 Noise

To generate more realistic seismic images, PSDM-coloured random noise (cf. Lubrano-Lavadera et al., 2019) was added to seismic sections for each of the three geomodels to investigate its impact on the seismic signature. Noise was added to the seismic images with frequencies of 20 Hz, illumination angles of 45° and incident angles of 20° for well B. The levels of noise added were 25%, 50% and 100%.

The results from adding noise to the seismic images are shown in figure 6.24. For all the geomodels the added noise breaks up the continuity of the reflections, and this effect increases with more noise added. The strongest reflections of the 'cross-sectional' geomodel are still possible to detect with 25% and 50% noise, but with 100% noise it is only the more laterally extensive reflections that can be detected. For both the 'Stomio' and 'Olive Grove' geomodels the strong laterally extensive reflections are detectable for all noise levels, but the continuity of the reflections gets disturbed with increased levels of noise.
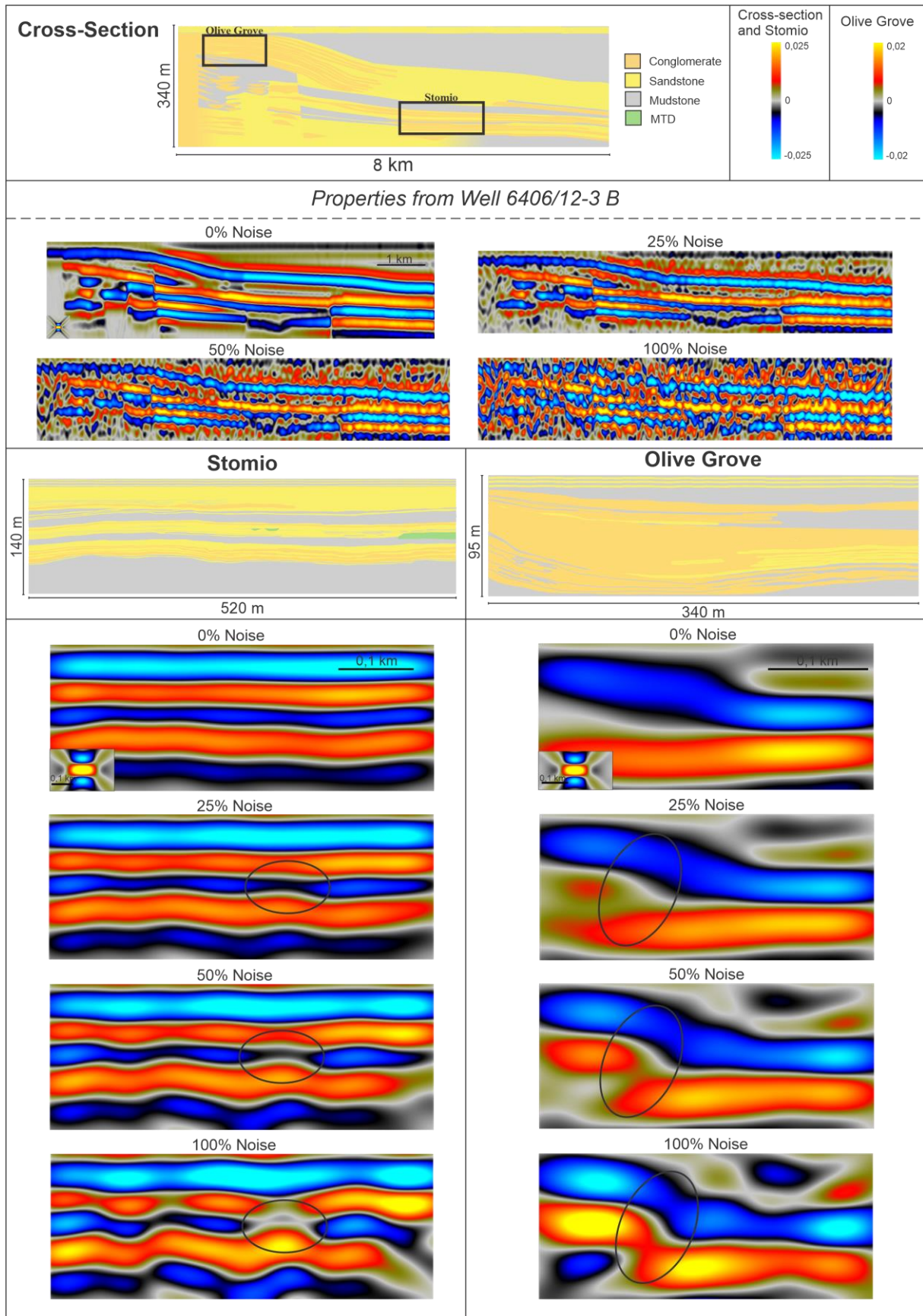
Figure 6. 24: Seismic images generated with 0%, 25 %, 50 and 100% noise for well B for the various geological models. Examples of areas affected by increased discontinuity of reflections with increased levels of noise are marked with a black circle on the 'Stomio' and 'Olive Grove' seismic. Note that the PSF is not vertically exaggerated for the 'cross-Section'.

6.3.5 Geological Uncertainty

To further investigate the impact of the small-scale features on the seismic images of 'Stomio' when modelled with elastic properties from well S, the seismic images from the original geomodel are compared to seismic generated from a geomodel where all mudstone, conglomerate and mass transport deposits are removed for the complex sandstone dominated WX3 unit (Figure 7.1). The negative reflectivity generated for WX3 has more lateral variation in amplitude strength when the mass-transport deposits, and conglomerate and mudstone layers are present. This indicates that even though the smaller scale features (e.g., mudstone layers < 1 m scale) are below seismic resolution, they will generate variations in the seismic expression in terms of lateral reflection heterogeneity.
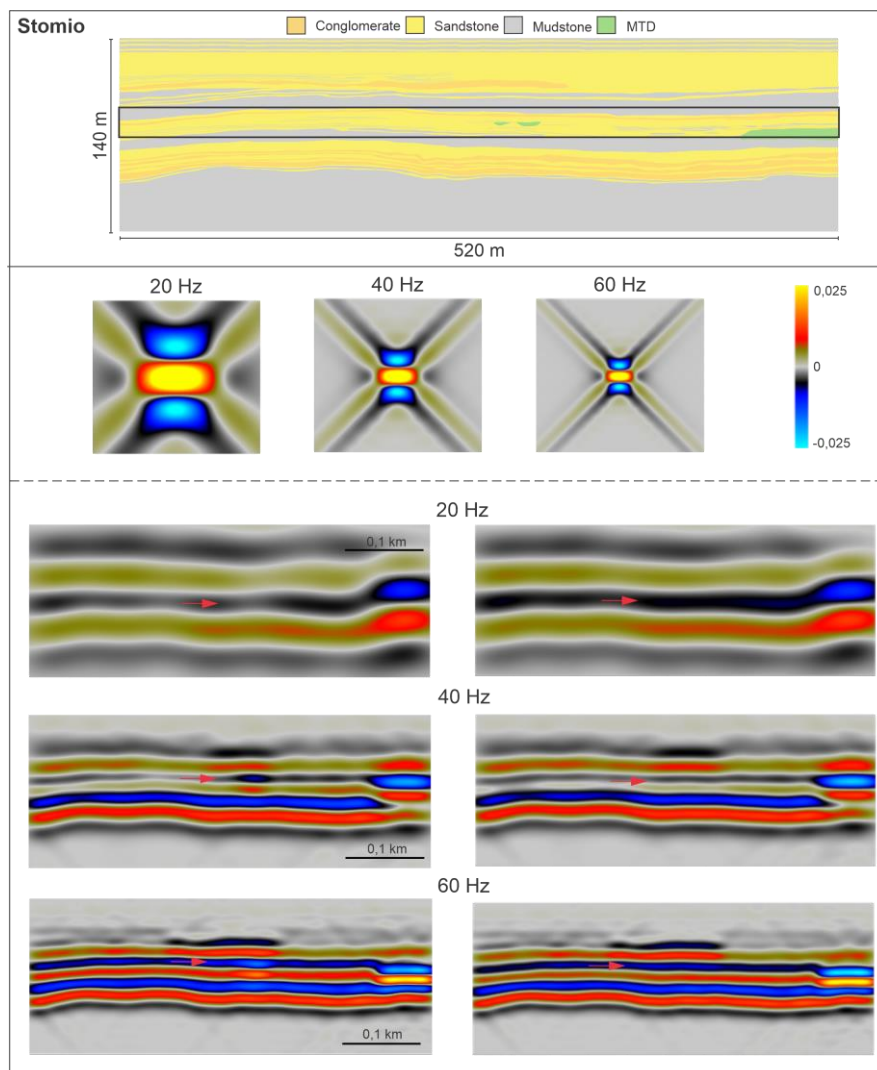
Figure 6. 25: Seismic generated with and without smaller scales features of the WX3 unit, which is marked with a black box on the geomodel, using properties from well S. The seismic images to the left are generated from the original geomodel, while the images to the right are generated from the pure sandstone WX3 unit. Red arrow marks the negative reflector generated for the WX3 unit. The amplitude effects from the mass-transport complexes are remarkable especially for 40 and 60 Hz. The pure sandstone scenario also has a lot less lateral variation in terms of amplitude strength within the reflector.

7 Discussion

This chapter discusses the results of the 2D synthetic seismic modelling generated from the outcrop-based geomodels from the West Xylokastro Fault Block presented in this thesis. The following sections will address the value of performing seismic modelling from 2D outcrops and the main outcomes from the 2D seismic modelling performed in this study. Further, the limitations related to the construction of the geomodels, and extractions of elastic properties are considered. Finally, the outcomes from this study will be compared to previous case studies of conventional seismic, shallow seismic and seismic modelling.

7.1 Application of Outcrop Analogues to Improve the Understanding of Deep-Water Syn-Rift Deposits

Virtual outcrop models provide important analogues for enhancing the understanding of the geology of subsurface hydrocarbon and carbon sequestration reservoirs by providing well-documented geobody geometry and dimensions within the scale gap between core and seismic observations (Howell et al., 2014). Syn-rift strata deposited in rift basins may host important hydrocarbon sites, but there is a lack of detailed studies considering submarine slope and basin floor sedimentary processes of coarse-grained deep-water syn-rift systems (Strachan et al., 2013). Syn-rift Jurassic strata in the North Sea comprise shallow-marine sandstones and turbidite plays (Myers et al., 2022). However, a case study investigating the failures of 98 exploration wells from the UK North Sea states that 56 % of the well failures targeted Jurassic deposits (Mathieu, 2018). This highlights the importance of improving the understanding of syn-rift deposits in order to drill successive exploration wells. By using outcrop analogues from the Onshore Corinth Rift, Greece the seismic expression of deposits in deep-water rift settings can be better understood. The 'Olive Grove' and 'Stomio' outcrop models expose proximal and distal Gilbert-type delta bottomset deposits, mainly composed of lobate architectural elements. These outcrops compose useful analogues to reveal the seismic expression, especially in terms of what level of scales the sedimentological and stratigraphic features can be resolved as changes in seismic stratigraphic architecture or subtle differences in seismic signature. The quality of the seismic images generated from such outcrop models is highly dependent on the level of interpretation and the chosen petrophysical properties.

7.2 Seismic Expression of the WXFB Outcrop Models

The results from the 2D seismic modelling images generated from the 'Olive Grove', 'Stomio', and 'cross-section' geomodels reveal the seismic expression of architectural elements in a fan system, mainly including lobate deposits. In terms of scales, the 'cross-section' geomodel is much larger than the individual outcrop models, and by comparing the seismic expression of the 'cross-section' to the outcrop-based geomodels it is possible to investigate what levels of detail that can be detected. Overall, the 2D seismic images of the 'cross-section' aims to give an idea of how syn-rift deep-water deposits may look like in seismic at a larger scale (e.g., "a prospect-scale), while the 2D seismic images of the outcrops provides a more detailed investigation of smaller scales (e.g., 'reservoir-scale).

Frequency

Frequency variability of the models reveal that this is the geophysical parameter having the most prominent effect on the resolution of the 2D seismic images, and thus the detectability of stratigraphic heterogeneity. For simplicity, the frequency band used throughout this study is the zero-phase, symmetrical Ricker wavelet which differs from conventional wavelets that tends to be asymmetrical, composing a source of error (Hosken, 1988; Simm and Bacon, 2014).

For the 20 and 40 Hz scenarios (Figure 6.14), which corresponds to frequencies of conventional seismic at typical depths of similar depositional systems on the Norwegian Continental Shelf (2500-4000 m TVDSS), the seismic expression of the 'cross-section' highlights that depositional units at scales of ~25 m within the WX-units in the Cullen et al (2020) stratigraphy of the RDF produce traceable reflectivity even where relatively minor impedance contrasts exists (e.g., between conglomerates and sandstones for well S). However, internal architecture within those units often remains unable to be imaged. The seismic character of the distal conglomerates within the WX5 unit could potentially lead to a pitfall when interpreting. Cullen et al (2021) interpreted the WX4 unit to be deposited during back-stepping of the delta feeding the RDF, and then the delta prograded back over itself displaying basinward downlapping deposits. The seismic reflections generated by the distal WX5 conglomerates located above the fault could be misinterpreted as deltaic foreset deposits. The WX5 unit also appears too thin to resolve the alternating layers of sandstones and conglomerates with low impedance contrasts. This can indicate that the seismic may not detect progradation/ retrogradation of deltas at that scale, composed of ~10 m thick beds.

In the seismic expression of the 'Stomio' model (Figure 6.15) with 20 and 40 Hz it is not possible to map out any single architectural elements within the WX-units. The reflectivity can mainly be connected to the reflectors generated between the WX-boundaries, as the dominant lithology changes, with laterally continuous high-amplitude reflections for well B and low-amplitude reflections for well S. For the 60 Hz scenario in the 'cross-section', single architectural elements above ~10 m scale is imaged in the seismic, e.g., small concave up features, where only some thinner heterolithic stratigraphy is merged together into single reflections. For the 'Stomio' model, at resolutions > 60 Hz it is possible to see the subtle internal geometry of the conglomeratic lobate deposits of WX5, and the conglomeratic debris flows within WX2 through lateral amplitude variability for well B properties. The seismic expression for well S has more limited impact to produce this amplitude variability throughout all frequency scenarios, where it is mainly the mass-transport deposits (MTD) that generates the strongest reflections. Whilst the edges of individual MTDs cannot be confidentially resolved they do present strong amplitude anomalies for 20 Hz and 60 Hz, however this geometry in 2D in the 40 Hz scenario could be misinterpreted as a structural fault feature.

As a result, the various scenarios reveal that units of several meters which are lithologically similar can be mapped out with relatively high confidence in the seismic images. However, given the simplistic appearance of these reflections compared to the complex heterogeneity observed in the outcrops, any depositional element interpretation would have to strongly rely on integration of well-based observations from core or wireline in the subsurface.

The seismic expression of the 140 Hz scenario (Figure 6.15) images a lot more detail compared to the other lower frequency scenarios. For the 'cross-section' geomodel, all levels of detail in the original model are exposed within the 2D seismic images for both well B and -S. For the 'Stomio' model individual bed-sets of lobate deposits are possible to map out, especially within WX2 and WX5, and the complex variations within WX3 are revealed for well B. For well S it is mainly the MTDs that generate stronger reflectivity, and it is possible to map the individual deposits out. In addition, it is also possible to recognise the laterally extensive lobate deposits of WX5. For 'Olive Grove', it is possible to map out the contours of the WX6 and WX7 lobate deposits. This indicates that high-resolution shallow seismic can identify and delineate stratigraphic heterogeneity within bottomset lobate deposits down to a few meters scale. High-resolution seismic in similar settings to models here, offer the potential for understanding the 3D architecture of sedimentary deposits at relatively fine spatial scales (meters-tens of meters)

and can be used to reliably interpret tectono-sedimentary reconstructions possibly at higher temporal resolutions where robust chronostratigraphy can add to seismic observations. Contrary to this, conventional seismic will likely merge similar deposits into larger reflectors as is commonly observed in deeper studies on deep marine lobes (e.g., Shanmugam, 2000) and will only be able to reconstruct teconto-sedimentary evolution at relatively coarse spatial and time-scales.

Illumination Angle

The maximum illumination angles of 10°, 20° and 45° generally produces a smoothing effect of the generated seismic images decreasing the lateral seismic resolution with lower maximum illumination angles. The effects of changing this geophysical parameter were not prominent for the 'Stomio' and 'Olive Grove' models, larger due to the sub-horizontal nature of the stratigraphy and relatively rare sharp edges to geobodies. The smoothing effect was best exposed for the 'cross-section' (Figure 6.17) when considering the seismic expression of the concave-up smaller-scale channel-fills, which were harder to distinguish from each other with lower illumination angles. Connectivity within reservoirs constitutes a decisive factor on the recovery from a petroleum reservoir (Larue and Hovadik, 2006). Some of the concave-up channel-fills appear as single storeys, but the lateral resolution issue with reduced illumination angles in seismic can image a false amalgamation of the channel deposits. The minor intra-basinal fault within the 'cross-section' was also better exposed with higher illumination angle. Illumination angle results are consistent with well documented trends for higher maximum illumination angles to resolve steeper dips (Lecomte et al., 2016). If the outcrop models either were of larger scale or had steeper dip of the layers, the effects of the illumination angle would probably be more prominent. With elastic properties from the Fenja wells, it demonstrated that depositional dips of up to 20 degrees, typical of the most up-dip part of the foreset-bottomset deposits can still be reliably images with the exception of highly extreme cases where angles beneath 10° are only imaged. The 2D seismic images of the 'cross-section' are all vertically exaggerated in a 1:5 scale, which is on the one hand side common when interpreting real seismic data, but when investigating the effect of the maximum illumination angle this could cover some of the effect from the lateral resolution issues (Faleide et al., 2022 *in press*). This means that the full lateral resolution effect from the maximum illumination angle might not be observed from the 2D seismic images presented in this study.

Incident Angle and Variability of Elastic Properties

Varying the incident angle of the modelled seismic sections produce variability in the amplitude of a reflectivity, however, these changes can be relatively local. For the 'Olive Grove' model (Figure 6.21-23) this was especially remarkable for the dipping layers of the WX5 and WX6 units for the 0°, 10°, 20° and 30° cases and highlights that shallow incident angles struggle to resolve the dip change between the lower part of the foreset and bottomset. The seismic images of well B and well S show slightly different trends in how an increase in incident angle affects the seismic expression. When interpreting real seismic a sum of the different angle stacks is typically used, referred to as a "conventional full stack', which typically composes the best quality data (Simm and Bacon, 2014). Considering the "full-stack" seismic images in this study, these are quite representative for the overall trend in the seismic. Despite this, the high variability between the angle stacks can indicate that it is worth for an interpreter to investigate the various angle stacks in order to identify potential details that can be lost in a "full-stack" seismic image. The concave-up channel-fill deposits within the 'cross-section' for well S (Figure 6.20) reveals that higher incidents angles creates an imaging problem of these architectural elements which could potentially display a false connectivity, as discussed in the 'Illumination Angle' section.

The seismic images generated with elastic properties from well B and well S display different characteristics. Well B represents a more deeply buried strata within the centre along the strike of the Vingleia Fault in the Fenja field and well S is located closer to the flank near the fault tip (Figure 5.2) (Jones et al., 2021), hence well B is more likely harder, and more compacted. This may mean that there is substantial variability on the seismic response of for example similar sedimentary systems on the basis of their elastic properties, so that similar sedimentological deposits may be imaged differently based on their respective location within a basin. Additionally, the impedance contrast is an important factor when imaging smaller scale features, e.g., the mass-transport deposit (MTD) within WX3 which is much more prominent when modelled with elastic properties from well S than well B. Figure 7.1 shows a plot for the reflector coefficient between an overlying sandstone package and underlying MTD, illustrating that well S has a higher reflection coefficient up to a 30° incident angle, and with an incident angle of 40° or higher they appear similar. Both reflection coefficients are also remarkably low, indicating that the surrounding stratigraphy also must be characterized by low reflection coefficients within well S due to the prominent effect of the MTDs in the seismic images.
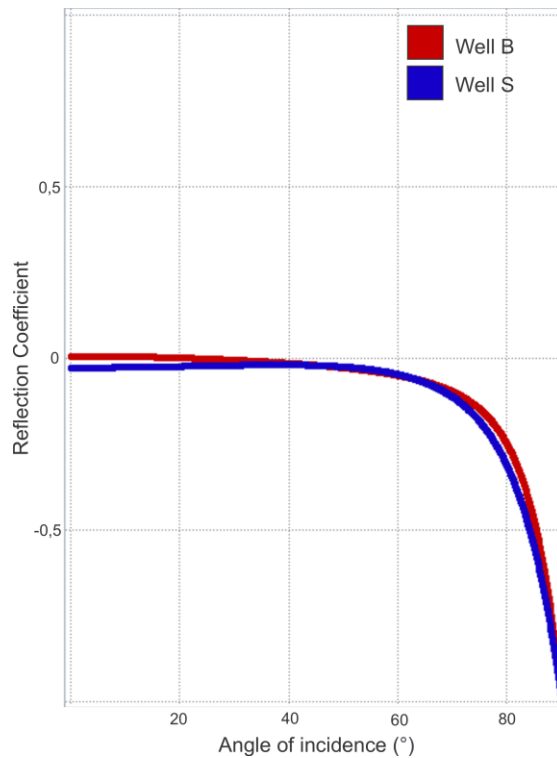
Figure 7. 1: Plot for the reflectivity coefficient between an overlying sandstone package and an underlying mass-transport-deposit for both well B and -S.

Noise

The quality of real seismic data is affected by noise, where the signal-to-noise ratio ideally should be as low as possible after processing a seismic dataset (Simm and Bacon, 2014). The results of adding noise levels of 25 %, 50% and 100% illustrates that the uncertainty of interpreting seismic data increases with increased level of noise. The continuity of reflectors gets disturbed when levels of noise are added to the seismic images. When adding 25 % noise some of the heterogeneities are lost in the seismic images, this is especially prominent for the smaller-scale features within the 'cross-section'. Adding 50 % noise makes it hard to interpret seismic reflections confidentially, which is most remarkable for 'Olive Grove' and the 'cross-section'. Overall, it is the characteristics of the most prominent laterally continuous reflectors that is preserved when adding noise. Additionally, it is important to consider that the seismic images generated for the frequency, illumination angle and incident angle are results corresponding to ideal seismic without noise, which is not the case when interpreting real seismic data.

7.2 Limitations and Uncertainties

In terms of evaluating the results from this study and comparing them to other case studies it is essential to keep the related limitations and uncertainties in mind. How the final geomodels used as input for the seismic modelling are constructed controls the value of the resulting 2D seismic images. Firstly, the geomodels have been interpreted in a stratigraphical and architectural sense by observations of an interpreter and their interpretation of published work in some cases. Additionally, as with any model, the final geomodel represents simplified versions of the outcrop models from the WXFB limited by resolution, modelling capacity and interpreter bias. Interpretations of outcrop models should ideally be done with a combination of field work to exploit the model to its full potential, which were not possible to conduct due to Covid travel restrictions. Despite this, previous field work including photographs and field logs were provided which aided the more process-based interpretations, particularly for the 'Olive Grove' outcrop. The resolution of the outcrop also varies, e.g., some parts are obscured by vegetation or mudwash which increases the uncertainty, but overall, the outcrop models used in this study have high enough resolution to make relatively detailed geomodels which are able to suitably characterise down to the bed and bed-set scale. However, the variability of this resolution means that for consistency, the distinction between stratigraphic units is purely lithological, including mudstones, sandstones, conglomerates, and mass-transport deposits, with no complex facies analysis e.g pebbly sandstones, sandy-conglomerates, clay-rich sandstones etc. Additionally, the resulting seismic images are highly dependent on the elastic properties of the input model, hence, collecting reliable elastic properties are crucial. The elastic properties extracted from the core- and well-data for wells 6406/12-3 B and -S were collected from the Fenja field which is a similar setting to the WXFB, since no petrophysical properties were obtained/ available for the respective outcrops. On the other hand, relatively short intervals were chosen for some lithologies (Figure 5.2) due to the restricted area below the free-water level. The values from the wireline logs may differ for the chosen core depths, which is even more uncertain for shorter intervals. The stratigraphy in the Gulf of Corinth was never buried as deeply as the depths the elastic properties are extracted from, this means equivalent layers of the ones exposed in the outcrop may have undergone substantial burial and compaction (e.g., equivalent mudstone units may be thinner) (Cullen et al., 2020; Gawthorpe et al., 2018).

7.3 Comparison to Other Case Studies

An important aspect of generating the 2D seismic images was to see how applicable these results are in comparison to real seismic data and how the findings of this study correspond to other seismic modelling studies. The following subsections compare the results from this study to other case studies of conventional seismic, shallow seismic and seismic modelling.

Conventional Seismic

The Jones et al (2022) paper considers a case study of a small, confined syn-rift basin from offshore Mid-Norway. The seismic dataset collected from this study area is generally characterized with a low frequency and the reflections are typically > 50 m in thickness. The main seismic surfaces within this dataset targets early-rift, peak-rift, and late-rift deposits. In similarity to the 'Olive Grove' and 'Stomio' outcrops the deposits are relatively coarse-grained fan deposits, deposited by turbidiy currents, debris flows and mass-transport deposits (Jones et al., 2021). Considering the fact that the seismic images from this field exposes reflectors above 50 m scale, is relatively consistent with the 20Hz scenarios modelled for the outcrop models, especially 'Olive Grove'. 'Olive Grove' which is only 85 m thick generates seismic images characterized with two reflections, while the 'Stomio' model images reflections down to ≈ 30 m scale. Compared to the results in this study, it is hard to map out features down to the sub-unit scale observed in the low resolution seismic.

Shallow Seismic

Seismic datasets in shallow seismic investigations commonly have vertical resolutions below 1m scale, with frequencies between 900 and 7000 Hz, e.g., small late Pleistocene fans in East Corcica (Deptuck et al., 2008; Sømme et al., 2011). The lobate deposits within this basin comprises two endmembers: small bodies deposited in a proximal setting with poorly developed levees, and larger, architecturally complex bodies deposited in a distal setting with composite mid-fan lobes. In the proximal basin floor, seismic lens-shaped deposits with various size could be separated by continuous reflectors (Deptuck et al., 2008). Compared to the lens-shaped conglomerates within the WX5 unit in 'Olive Grove' that were modelled with 140 Hz, these were not possible to recognise as individual architectural elements and fell below seismic resolution. From Deptuck et al (2008) it is possible to map out single lens-shaped shaped deposits, but frequencies of 140 Hz is still not enough to image lens-shaped deposits with peak-frequencies of 2,5 m. In the Basin floor seismic from the East Corcia case study individual stacked sedimentary lobes were imaged. Compared to the 2D seismic images from this study

with 140 Hz some single lobate deposits only reaching a few m are possible to map out, but not to the same extent. In 'Stomio' the WX5 lobate forms, interference within the lobate deposits of WX3, and contours of the conglomeratic lobes within WX2 were possible to map out. For 'Olive Grove' the lobate forms of WX7 and WX6 were possible to map out. This indicates for shallow high-resolution seismic it is possible to map out lobate deposits with high enough frequencies, but single lobate forms usually fall below seismic resolution of 140 Hz, and require substantially higher frequencies typical of the Golo studies (e.g., Deptuck et al., 2008).

Seismic Modelling

The Bakke et al (2008) considers a seismic modelling study of a turbidite system of the St. Vicente Formation in the Southern Pyrenees, Spain. The unit is mainly composed of five clastic turbidite units bounded by erosional surfaces. The petrophysical properties were extracted the same way as for the outcrop models used in this study, from offshore well-data from an analogues subsurface setting, and the seismic images were generated with a frequency of 45 Hz. The seismic imaging from this study revealed that distinctive amalgamated beds within larger units are hard to distinguish in seismic, especially if they have similar petrophysical properties (Bakke et al., 2008). This is also similar to the imaging of the Olive grove model for the Southern WX5 unit composed of amalgamated conglomerates interbedded with thinner mudstone layers, where it is not possible to map out the internal characterization of the amalgamated conglomerate beds. The finding of the seismic expression of the mass-transport deposits within the 'Stomio' outcrop model indicates that if small-scale features compose a high impedance contrast, they will appear either as distinct features or affect the seismic characteristics depending on the frequency of the seismic. This was very prominent when comparing the seismic expression of these deposits in the images from well B and -S.

8 Conclusions

The main aim of this study was to improve the understanding of the seismic expression of coarse-grained syn-rift deep-water depositional systems. This was achieved by outlining realistic geological models from the 'Olive Grove' and 'Stomio' virtual outcrop models from the Gulf of Corinth, Greece, and assign them models elastic properties. Further, 2D seismic images were generated from the respective geomodels through the 2(3)D PSF convolution approach, with various geophysical parameters assigned.

4. **What is the seismic signature of coarse-grained deep-water syn-rift deposits in proximal and distal domains, and can difference in their architecture be reliably determined from seismic?**

- The 'Olive Grove' outcrop represents proximal deep-water syn-rift deposits, while the 'Stomio' outcrop model represents more distal deep-water syn-rift deposits. The seismic expression of these outcrops is highly dependent on the resolution of the seismic images. Based on the 2D seismic images generated in this study it is not possible to confidently map out architectural elements from these systems, and overall, the seismic expression of these outcrops is highly simplified.

- The seismic images reveal that even though the architectural elements are not very well imaged the complex heterogeneity of these deposits will generate subtle amplitude variabilities. One must be careful when interpreting to avoid potential interpretational pitfals, e.g, structural features generated by mass transport deposits.

- Considering the simplistic appearance of the reflections in the seismic images, any depositional element interpretation would require integration of well-based observations from core or wireline in the subsurface.

5. **Which scales of heterogeneity produce reflectivity within low resolution (e.g., deep or explorations seismic) and high resolution (e.g., shallow/near surface seismic) seismic datasets?**

- Low resolution (20 Hz) seismic reveals that only major changes in the dominant lithologies can be resolved e.g, units at scales corresponding to the WX-units (10s of metres).

- In high-resolution (140 Hz) more heterogeneity can be resolved down to a few meters scale. Even though a higher amount of individual architectural elements can be resolved, e.g., lobate deposits, there are still internal heterogeneity that cannot be imaged in the seismic.

6. **Which geophysical parameters have the strongest influence upon the detectability of complex stratigraphy architectures in seismic datasets in deep-water syn-rift systems?**

- The geophysical parameter having the strongest influence upon the detectability of stratigraphic architecture is the dominant frequency. A higher frequency allows for detectability of architectural elements at a lower scale.

- The illumination angle affects the lateral resolution of the seismic images, e.g., creating false connectivity between architectural elements.

- The variability of the seismic imaging effects by changing incident angles suggests that "full-stack" images is the most representative, but it is important to be aware of the details within individual angle stacks that can be lost.

- The elastic properties of the geomodels also composes a decisive factor in the seismic expression of various depositional elements. This is especially prominent for smaller scale features, e.g., the mass-transport deposits, revealing that the imaging of these features is highly dependent on the impedance contrasts to the surrounding stratigraphy.

- The 2D seismic images represents ideal seismic without noise, and in real seismic data there will always be noise present. The 2D seismic images generated with random noise reveals that a higher level of noise will disturb the continuity of the reflections, hence less confident interpretations can be performed.

8.1 Further Work

This study contributes to the improvement of the understanding of the seismic expression of syn-rift deep-water depositional systems. Regardless of this, there are still many uncertainties related to complexity of these systems.

- Regarding the geomodels outlined in this thesis, it would be useful to investigate these outcrop models in the field to assign more complexity to these geomodels. This improves the level of bedscale details added to the models as well as an improvement in the complexity of the assigned elastic properties.

- Further, by both improving this particular study and also preforming detailed studies of other analogues it could improve the broader understanding of these complex systems. Additionally, an even more detailed comparison to similar environment in the subsea, e.g., the Fenja field, would also contribute to strengthen the current understanding.

References

AMY, L., TALLING, P., PEAKALL, J., WYNN, R. & THYNNE, R. A. 2005. Bed geometry used to test recognition criteria of turbidites and (sandy) debrites. *Sedimentary Geology,* 179**,** 163-174.

ANDERSEN, I. G. 2020. *Effects of geophysical parameters on the seismic expression of the Maghlaq Fault, Malta: insights from outcrop-based 2D seismic modeling.* The University of Bergen.

ARMIJO, R., MEYER, B., KING, G., RIGO, A. & PAPANASTASSIOU, D. 1996. Quaternary evolution of the Corinth Rift and its implications for the Late Cenozoic evolution of the Aegean. *Geophysical Journal International,* 126**,** 11-53.

BAKKE, K., GJELBERG, J. & PETERSEN, S. A. 2008. Compound seismic modelling of the Ainsa II turbidite system, Spain: Application to deep-water channel systems offshore Angola. *Marine and Petroleum Geology,* 25**,** 1058-1073.

BECKERS, A., HUBERT-FERRARI, A., BECK, C., PAPATHEODOROU, G., DE BATIST, M., SAKELLARIOU, D., TRIPSANAS, E. & DEMOULIN, A. 2018. Characteristics and frequency of large submarine landslides at the western tip of the Gulf of Corinth. *Natural Hazards and Earth System Sciences,* 18**,** 1411-1425.

BEMIS, S. P., MICKLETHWAITE, S., TURNER, D., JAMES, M. R., AKCIZ, S., THIELE, S. T. & BANGASH, H. A. 2014. Ground-based and UAV-Based photogrammetry: A multi-scale, high-resolution mapping tool for structural geology and paleoseismology. *Journal of Structural Geology,* 69**,** 163-178.

BILMES, A., D'ELIA, L., LOPEZ, L., RICHIANO, S., VARELA, A., DEL PILAR ALVAREZ, M., BUCHER, J., EYMARD, I., MURAVCHIK, M. & FRANZESE, J. 2019. Digital outcrop modelling using "structure-from-motion" photogrammetry: Acquisition strategies, validation and interpretations to different sedimentary environments. *Journal of South American Earth Sciences,* 96**,** 102325.

BOGGS, S. 2014. *Principles of sedimentology and stratigraphy,* Harlow, Essex, Pearson.

BOULESTEIX, K., POYATOS-MORÉ, M., FLINT, S. S., TAYLOR, K. G., HODGSON, D. M. & HASIOTIS, S. T. 2019. Transport and deposition of mud in deep-water environments: Processes and stratigraphic implications. *Sedimentology,* 66**,** 2894-2925.

BOUMA, A. H. 1962. Sedimentology of some flysch deposits. *Agraphic approach to facies interpretation,* 168.

BUCKLEY, S. J., RINGDAL, K., NAUMANN, N., DOLVA, B., KURZ, T. H., HOWELL, J. A. & DEWEZ, T. J. 2019. LIME: Software for 3-D visualization, interpretation, and communication of virtual geoscience models. *Geosphere,* 15**,** 222-235.

BULL, S., CARTWRIGHT, J. & HUUSE, M. 2009. A subsurface evacuation model for submarine slope failure. *Basin Research,* 21**,** 433-443.

BURNHAM, B. S. & HODGETTS, D. 2019. Quantifying spatial and architectural relationships from fluvial outcrops. *Geosphere,* 15**,** 236-253.

BAAS, J. H., BEST, J. L., PEAKALL, J. & WANG, M. 2009. A phase diagram for turbulent, transitional, and laminar clay suspension flows. *Journal of Sedimentary Research,* 79**,** 162-183.

CICCONETO, F., VIEIRA, L. V., ABEL, M., DOS SANTOS ALVARENGA, R., CARBONERA, J. L. & GARCIA, L. F. 2022. GeoReservoir: An ontology for deep-marine depositional system geometry description. *Computers & Geosciences,* 159**,** 105005.

CULLEN, T. M. 2020. *Controls on the Evolution and Character of Siliciclastic Deep-Water Syn-Rift Depositional Systems.* University of Leeds.

CULLEN, T. M., COLLIER, R. E. L., GAWTHORPE, R. L., HODGSON, D. M. & BARRETT, B. J. 2020. Axial and transverse deep-water sediment supply to syn-rift fault terraces: Insights from the West Xylokastro Fault Block, Gulf of Corinth, Greece. *Basin Research,* 32**,** 1105-1139.

CULLEN, T. M., COLLIER, R. E. L., HODGSON, D. M., GAWTHORPE, R., KOULI, K., MAFFIONE, M., KRANIS, H. & ELIASSEN, G. T. 2021. Deep-water syn-rift stratigraphy as archives of Early-Mid Pleistocene palaeoenvironmental signals and controls on sediment delivery.

CULLIS, S., COLOMBERA, L., PATACCI, M. & MCCAFFREY, W. D. 2018. Hierarchical classifications of the sedimentary architecture of deep-marine depositional systems. *Earth-Science Reviews,* 179**,** 38-71.

DEPTUCK, M. E., PIPER, D. J., SAVOYE, B. & GERVAIS, A. 2008. Dimensions and architecture of late Pleistocene submarine lobes off the northern margin of East Corsica. *Sedimentology,* 55**,** 869-898.

DI CELMA, C., CANTALAMESSA, G. & DIDASKALOU, P. 2013. Stratigraphic organization and predictability of mixed coarse-grained and fine-grained successions in an upper slope Pleistocene turbidite system of the Peri-Adriatic basin. *Sedimentology,* 60**,** 763-799.

DODD, T. J., MCCARTHY, D. J. & RICHARDS, P. C. 2019. A depositional model for deep-lacustrine, partially confined, turbidite fans: Early Cretaceous, North Falkland Basin. *Sedimentology,* 66**,** 53-80.

FALEIDE, T. S., BRAATHEN, A., LECOMTE, I. & ANELL, I. 2022. Exploring seismic detection and resolution thresholds of fault zones and gas seeps in the shallow subsurface using seismic modelling. In press.

FALEIDE, T. S., BRAATHEN, A., LECOMTE, I., MULROONEY, M. J., MIDTKANDAL, I., BUGGE, A. J. & PLANKE, S. 2021. Impacts of seismic resolution on fault interpretation: Insights from seismic modelling. *Tectonophysics,* 816**,** 229008.

FALIVENE, O., ARBUÉS, P., LEDO, J., BENJUMEA, B., MUÑOZ, J. A., FERNÁNDEZ, O. & MARTÍNEZ, S. 2010. Synthetic seismic models from outcrop-derived reservoir-scale three-dimensional facies models: The Eocene Ainsa turbidite system (southern Pyrenees). *AAPG bulletin,* 94**,** 317-343.

FELIX, M. & PEAKALL, J. 2006. Transformation of debris flows into turbidity currents: mechanisms inferred from laboratory experiments. *Sedimentology,* 53**,** 107-123.

FORD, M., HEMELSDAËL, R., MANCINI, M. & PALYVOS, N. 2017. Rift migration and lateral propagation: evolution of normal faults and sediment-routing systems of the western Corinth rift (Greece). *Geological Society, London, Special Publications,* 439**,** 131-168.

GALLOWAY, W. E. 1998. Siliciclastic slope and base-of-slope depositional systems: component facies, stratigraphic architecture, and classification. *AAPG bulletin,* 82**,** 569-595.

GARCIA, M., ERCILLA, G., ALONSO, B., ESTRADA, F., JANE, G., MENA, A., ALVES, T. & JUAN, C. 2015. Deep-water turbidite systems: a review of their elements, sedimentary processes and depositional models. Their characteristics on the Iberian margins-Sistemas turbidíticos de aguas profundas: revisión de sus elementos, procesos sedimentarios y modelos deposicionales. Sus características en los márgenes Ibéricos. *Boletín geológico y minero,* 126**,** 189-218.

GARLAND, C., HAUGHTON, P., KING, R. & MOULDS, T. Capturing reservoir heterogeneity in a sand-rich submarine fan, Miller Field. Geological Society, London, Petroleum Geology Conference series, 1999. Geological Society of London, 1199-1208.

GAWTHORPE, R. L., ANDREWS, J. E., COLLIER, R. E., FORD, M., HENSTRA, G. A., KRANIS, H., LEEDER, M. R., MURAVCHIK, M. & SKOURTSOS, E. 2017. Building up or out? Disparate sequence architectures along an active rift margin—Corinth rift, Greece. *Geology,* 45**,** 1111-1114.

GAWTHORPE, R. L., FABREGAS, N., PECHLIVANIDOU, S., FORD, M., COLLIER, R. E. L., CARTER, G. D., MCNEILL, L. C. & SHILLINGTON, D. J. 2022. Late Quaternary mud-dominated, basin-floor sedimentation of the Gulf of Corinth, Greece: Implications for deep-water depositional processes and controls on syn-rift sedimentation. *Basin Research*.

GAWTHORPE, R. L., LEEDER, M. R., KRANIS, H., SKOURTSOS, E., ANDREWS, J. E., HENSTRA, G. A., MACK, G. H., MURAVCHIK, M., TURNER, J. A. & STAMATAKIS, M. 2018. Tectono-sedimentary evolution of the Plio-Pleistocene Corinth rift, Greece. *Basin Research,* 30**,** 448-479.

GOBO, K., GHINASSI, M. & NEMEC, W. 2014. Reciprocal changes in foreset to bottomset facies in a Gilbert-type delta: response to short-term changes in base level. *Journal of Sedimentary Research,* 84**,** 1079-1095.

GOBO, K., GHINASSI, M. & NEMEC, W. 2015. Gilbert-type deltas recording short-term base-level changes: Delta-brink morphodynamics and related foreset facies. *Sedimentology,* 62**,** 1923-1949.

HARRIS, P. T. & WHITEWAY, T. 2011. Global distribution of large submarine canyons: Geomorphic differences between active and passive continental margins. *Marine Geology,* 285**,** 69-86.

HAUGHTON, P., DAVIS, C., MCCAFFREY, W. & BARKER, S. 2009. Hybrid sediment gravity flow deposits–classification, origin and significance. *Marine and Petroleum Geology,* 26**,** 1900-1918.

HENSTRA, G. A., GRUNDVÅG, S.-A., JOHANNESSEN, E. P., KRISTENSEN, T. B., MIDTKANDAL, I., NYSTUEN, J. P., ROTEVATN, A., SURLYK, F., SÆTHER, T. & WINDELSTAD, J. 2016. Depositional processes and stratigraphic architecture within a coarse-grained rift-margin turbidite system: The Wollaston Forland Group, east Greenland. *Marine and Petroleum Geology,* 76**,** 187-209.

HERRON, D. A. 2011. *First steps in seismic interpretation*, Society of Exploration Geophysicists.

HODGSON, D., DI CELMA, C., BRUNT, R. & FLINT, S. 2011. Submarine slope degradation and aggradation and the stratigraphic evolution of channel–levee systems. *Journal of the Geological Society,* 168**,** 625-628.

HODGSON, D. M., KANE, I. A., FLINT, S. S., BRUNT, R. L. & ORTIZ-KARPF, A. 2016. Time-transgressive confinement on the slope and the progradation of basin-floor fans: Implications for the sequence stratigraphy of deep-water deposits. *Journal of Sedimentary Research,* 86**,** 73-86.

HOSKEN, J. 1988. Ricker wavelets in their various guises. *First Break,* 6.

HOWELL, J. A., MARTINIUS, A. W. & GOOD, T. R. 2014. The application of outcrop analogues in geological modelling: a review, present status and future outlook. *Geological Society, London, Special Publications,* 387**,** 1-25.

IVERSON, R. M. 1997. The physics of debris flows. *Reviews of geophysics,* 35**,** 245-296.

JACKSON, C. A., MCANDREW, A. E., HODGSON, D. M. & DREYER, T. 2021. Repeated degradation and progradation of a submarine slope over geological timescales. *Journal of Sedimentary Research,* 91**,** 116-145.

JOBE, Z. R., LOWE, D. R. & MORRIS, W. R. 2012. Climbing-ripple successions in turbidite systems: depositional environments, sedimentation rates and accumulation times. *Sedimentology,* 59**,** 867-898.

JONES, G. E., WELBON, A. I., MOHAMMADLOU, H., SAKHAROV, A., FORD, J., NEEDHAM, T. & OTTESEN, C. 2021. Complex stratigraphic fill of a small, confined syn-rift basins: an Upper Jurassic example from offshore mid-Norway. *Geological Society, London, Special Publications,* 495.

KANE, I. A., KNELLER, B. C., DYKSTRA, M., KASSEM, A. & MCCAFFREY, W. D. 2007. Anatomy of a submarine channel–levee: an example from Upper Cretaceous slope sediments, Rosario Formation, Baja California, Mexico. *Marine and Petroleum Geology,* 24**,** 540-563.

KANE, I. A., PONTÉN, A. S., VANGDAL, B., EGGENHUISEN, J. T., HODGSON, D. M. & SPYCHALA, Y. T. 2017. The stratigraphic record and processes of turbidity current transformation across deep-marine lobes. *Sedimentology,* 64**,** 1236-1273.

KNELLER, B. C. & BRANNEY, M. J. 1995. Sustained high-density turbidity currents and the deposition of thick massive sands. *Sedimentology,* 42**,** 607-616.

LARUE, D. K. & HOVADIK, J. 2006. Connectivity of channelized reservoirs: a modelling approach. *Petroleum Geoscience,* 12**,** 291-308.

LECOMTE, I., LAVADERA, P. L., ANELL, I., BUCKLEY, S. J., SCHMID, D. W. & HEEREMANS, M. 2015. Ray-based seismic modeling of geologic models: Understanding and analyzing seismic images efficiently. *Interpretation,* 3**,** SAC71-SAC89.

LECOMTE, I., LAVADERA, P. L., BOTTER, C., ANELL, I., BUCKLEY, S. J., EIDE, C. H., GRIPPA, A., MASCOLO, V. & KJOBERG, S. 2016. 2 (3) D convolution modelling of complex geological targets beyond–1D convolution. *First Break,* 34.

LEEDER, M., MARK, D., GAWTHORPE, R., KRANIS, H., LOVELESS, S., PEDENTCHOUK, N., SKOURTSOS, E., TURNER, J., ANDREWS, J. & STAMATAKIS, M. 2012. A "Great Deepening": chronology of rift climax, Corinth rift, Greece. *Geology,* 40**,** 999-1002.

LOWE, D. R. 1982. Sediment gravity flows; II, Depositional models with special reference to the deposits of high-density turbidity currents. *Journal of sedimentary research,* 52**,** 279-297.

LUBRANO-LAVADERA, P., SENGER, K., LECOMTE, I., MULROONEY, M. J. & KÜHN, D. 2019. Seismic modelling of metre-scale normal faults at a reservoir-cap rock interface in Central Spitsbergen, Svalbard: implications for CO_2 storage. *Norwegian Journal of Geology,* 99**,** 329-347.

MACDONALD, H. A., PEAKALL, J., WIGNALL, P. B. & BEST, J. 2011. Sedimentation in deep-sea lobe-elements: implications for the origin of thickening-upward sequences. *Journal of the Geological Society,* 168**,** 319-332.

MAIER, K. L., JOHNSON, S. Y. & HART, P. 2018. Controls on submarine canyon head evolution: Monterey Canyon, offshore central California. *Marine Geology,* 404**,** 24-40.

MAJOR, J. J. & IVERSON, R. M. 1999. Debris-flow deposition: Effects of pore-fluid pressure and friction concentrated at flow margins. *Geological Society of America Bulletin,* 111**,** 1424-1434.

MANZOCCHI, T., CARTER, J. N., SKORSTAD, A., FJELLVOLL, B., STEPHEN, K. D., HOWELL, J., MATTHEWS, J. D., WALSH, J. J., NEPVEU, M. & BOS, C. 2008. Sensitivity of the impact

of geological uncertainty on production from faulted and unfaulted shallow-marine oil reservoirs: objectives and methods. *Petroleum Geoscience,* 14**,** 3-15.

MATHIEU, C. J. Exploration well failures from the UK North Sea. Geological Society, London, Petroleum Geology Conference Series, 2018. Geological Society of London, 267-272.

MAYALL, M., LONERGAN, L., BOWMAN, A., JAMES, S., MILLS, K., PRIMMER, T., POPE, D., ROGERS, L. & SKEENE, R. 2010. The response of turbidite slope channels to growth-induced seabed topography. *AAPG bulletin,* 94**,** 1011-1030.

MCHARGUE, T. R., HODGSON, D. M. & SHELEF, E. 2021. Architectural Diversity of Submarine Lobate Deposits. *Frontiers in Earth Science***,** 632.

MCNEILL, L. C., SHILLINGTON, D. J., CARTER, G., EVEREST, J. D., GAWTHORPE, R. L., MILLER, C., PHILLIPS, M. P., COLLIER, R. E. L., CVETKOSKA, A. & DE GELDER, G. 2019. High-resolution record reveals climate-driven environmental and sedimentary changes in an active rift. *Scientific reports,* 9**,** 1-11.

MITCHUM JR, R. M. 1985. Seismic stratigraphic expression of submarine fans: chapter 7.

MULDER, T. 2011. Gravity processes and deposits on continental slope, rise and abyssal plains. *Developments in Sedimentology.* Elsevier.

MULDER, T. & ALEXANDER, J. 2001. The physical character of subaqueous sedimentary density flows and their deposits. *Sedimentology,* 48**,** 269-299.

MURAVCHIK, M., HENSTRA, G. A., ELIASSEN, G. T., GAWTHORPE, R. L., LEEDER, M., KRANIS, H., SKOURTSOS, E. & ANDREWS, J. 2020. Deep-water sediment transport patterns and basin floor topography in early rift basins: Plio-Pleistocene syn-rift of the Corinth Rift, Greece. *Basin Research,* 32**,** 1184-1212.

MUTTI, E., REMACHA, E., SGAVETTI, M., ROSELL, J., VALLONI, R. & ZAMORANO, M. Stratigraphy and facies characteristics of the Eocene Hecho Group turbidite systems, south-central Pyrenees. Excursion Guidebook of the 6th European Regional Meeting, International Association of Sedimentologists, Lleida, Spain, 1985. 519-576.

MYERS, K., ROUILLARD, P. & ZANELLA, E. 2022. Exploration performance in the UK and Norwegian North Sea. *Geological Society, London, Special Publications,* 494**,** 187-196.

NEMEC, W. 1990. Aspects of sediment movement on steep delta slopes. *Coarse-grained deltas,* 10**,** 29-73.

PAPANIKOLAOU, D. J. & ROYDEN, L. H. 2007. Disruption of the Hellenic arc: Late Miocene extensional detachment faults and steep Pliocene-Quaternary normal faults—Or what happened at Corinth? *Tectonics,* 26.

PATACCI, M., HAUGHTON, P. D. & MCCAFFREY, W. D. 2014. Rheological complexity in sediment gravity flows forced to decelerate against a confining slope, Braux, SE France. *Journal of Sedimentary Research,* 84**,** 270-277.

PIPER, D. J. & NORMARK, W. R. 2009. Processes that initiate turbidity currents and their influence on turbidites: a marine geology perspective. *Journal of Sedimentary Research,* 79**,** 347-362.

POSAMENTIER, H. W. & KOLLA, V. 2003. Seismic geomorphology and stratigraphy of depositional elements in deep-water settings. *Journal of sedimentary research,* 73**,** 367-388.

POSAMENTIER, H. W., MARTINSEN, O. J. & SHIPP, R. 2011. The character and genesis of submarine mass-transport deposits: insights from outcrop and 3D seismic data. *Mass-transport deposits in deepwater settings. Tulsa: SEPM, Special Publication,* 96**,** 7-38.

POSAMENTIER, H. W. & WALKER, R. G. 2006. Deep-water turbidites and submarine fans.

POSTMA, G. 1984. Slumps and their deposits in fan delta front and slope. *Geology,* 12**,** 27-30.

POSTMA, G., NEMEC, W. & KLEINSPEHN, K. L. 1988. Large floating clasts in turbidites: a mechanism for their emplacement. *Sedimentary geology,* 58**,** 47-61.

READING, H. G. & RICHARDS, M. 1994. Turbidite systems in deep-water basin margins classified by grain size and feeder system. *AAPG bulletin,* 78**,** 792-822.

REISER, C., BIRD, T., ENGELMARK, F., ANDERSON, E. & BALABEKOV, Y. 2012. Value of broadband seismic for interpretation, reservoir characterization and quantitative interpretation workflows. *First Break,* 30.

RICKER, N. 1940. The form and nature of seismic waves and the structure of seismograms. *Geophysics,* 5**,** 348-366.

RIDER, M. H. & KENNEDY, M. 2011. *The geological interpretation of well logs,* Aberdeen?, Rider-French.

ROHAIS, S., ESCHARD, R. & GUILLOCHEAU, F. 2008. Depositional model and stratigraphic architecture of rift climax Gilbert-type fan deltas (Gulf of Corinth, Greece). *Sedimentary Geology,* 210**,** 132-145.

ROHAIS, S., JOANNIN, S., COLIN, J.-P., SUC, J.-P., GUILLOCHEAU, F. & ESCHARD, R. 2007. Age and environmental evolution of the syn-rift fill of the southern coast of the Gulf of Corinth (Akrata-Derveni region, Greece). *Bulletin de la Société géologique de France,* 178**,** 231-243.

RUBI, R., ROHAIS, S., BOURQUIN, S., MORETTI, I. & DESAUBLIAUX, G. 2018. Processes and typology in Gilbert-type delta bottomset deposits based on outcrop examples in the Corinth Rift. *Marine and Petroleum Geology,* 92**,** 193-212.

RYAN, H. 1994. Ricker, Ormsby; Klander, Bntterwo-A Choice of Wavelets. CSEG Recorder Calgary, AB, Canada.

SHANMUGAM, G. 2000. 50 years of the turbidite paradigm (1950s—1990s): deep-water processes and facies models—a critical perspective. *Marine and petroleum Geology,* 17**,** 285-342.

SHANMUGAM, G. 2016. Submarine fans: a critical retrospective (1950–2015). *Journal of Palaeogeography,* 5**,** 110-184.

SHANMUGAM, G. & MOIOLA, R. 1988. Submarine fans: characteristics, models, classification, and reservoir potential. *Earth-Science Reviews,* 24**,** 383-428.

SIMM, R. & BACON, M. 2014. *Seismic Amplitude: An interpreter's handbook*, Cambridge University Press.

SOHN, Y. K. 2000. Depositional processes of submarine debris flows in the Miocene fan deltas, Pohang Basin, SE Korea with special reference to flow transformation. *Journal of Sedimentary Research,* 70**,** 491-503.

SOUTTER, E. L., KANE, I. A., FUHRMANN, A., CUMBERPATCH, Z. A. & HUUSE, M. 2019. The stratigraphic evolution of onlap in siliciclastic deep-water systems: Autogenic modulation of allogenic signals. *Journal of Sedimentary Research,* 89**,** 890-917.

SOUTTER, E. L., KANE, I. A., HODGSON, D. M. & FLINT, S. 2021. The concavity of submarine canyon longitudinal profiles. *Journal of Geophysical Research: Earth Surface,* 126**,** e2021JF006185.

SPRAGUE, A., GARFIELD, T., GOULDING, F., BEAUBOUEF, R., SULLIVAN, M., ROSSEN, C., CAMPION, K., SICKAFOOSE, D., ABREU, V. & SCHELLPEPER, M. 2005. Integrated slope channel depositional models: the key to successful prediction of reservoir presence and quality in offshore West Africa. *Veracruz, Mexico, Colegio de Ingenenieros Petroleros de México***,** 1-13.

SPYCHALA, Y. T., HODGSON, D. M., FLINT, S. & MOUNTNEY, N. 2015. Constraining the sedimentology and stratigraphy of submarine intraslope lobe deposits using exhumed examples from the Karoo Basin, South Africa. *Sedimentary Geology,* 322**,** 67-81.

STEVENSON, C. J., JACKSON, C. A.-L., HODGSON, D. M., HUBBARD, S. M. & EGGENHUISEN, J. T. 2015. Deep-water sediment bypass. *Journal of Sedimentary Research,* 85**,** 1058-1081.

STOW, D. & SMILLIE, Z. 2020. Distinguishing between deep-water sediment facies: Turbidites, contourites and hemipelagites. *Geosciences,* 10**,** 68.

STRACHAN, L. J. 2008. Flow transformations in slumps: a case study from the Waitemata Basin, New Zealand. *Sedimentology,* 55**,** 1311-1332.

STRACHAN, L. J., RARITY, F., GAWTHORPE, R. L., WILSON, P., SHARP, I. & HODGETTS, D. 2013. Submarine slope processes in rift-margin basins, Miocene Suez Rift, Egypt. *Bulletin,* 125**,** 109-127.

SØMME, T. O., PIPER, D. J., DEPTUCK, M. E. & HELLAND-HANSEN, W. 2011. Linking onshore–offshore sediment dispersal in the Golo source-to-sink system (Corsica, France) during the late Quaternary. *Journal of Sedimentary Research,* 81**,** 118-137.

TALLING, P. J., MASSON, D. G., SUMNER, E. J. & MALGESINI, G. 2012. Subaqueous sediment density flows: Depositional processes and deposit types. *Sedimentology,* 59**,** 1937-2003.

TEK, D. E., MCARTHUR, A. D., POYATOS-MORÉ, M., COLOMBERA, L., ALLEN, C., PATACCI, M. & MCCAFFREY, W. D. 2022. Controls on the architectural evolution of deep-water channel overbank sediment wave fields: insights from the Hikurangi Channel, offshore New Zealand. *New Zealand Journal of Geology and Geophysics,* 65**,** 141-178.

TEK, D. E., MCARTHUR, A. D., POYATOS-MORÉ, M., COLOMBERA, L., PATACCI, M., CRAVEN, B. & MCCAFFREY, W. D. 2021. Relating seafloor geomorphology to subsurface architecture: how mass-transport deposits and knickpoint-zones build the stratigraphy of the deep-water Hikurangi Channel. *Sedimentology,* 68**,** 3141-3190.

TILLMANS, F., GAWTHORPE, R. L., JACKSON, C. A. L. & ROTEVATN, A. 2021. Syn-rift sediment gravity flow deposition on a Late Jurassic fault-terraced slope, northern North Sea. *Basin Research,* 33**,** 1844-1879.

WALKER, R. G. 1978. Deep-water sandstone facies and ancient submarine fans: models for exploration for stratigraphic traps. *AAPG Bulletin,* 62**,** 932-966.

WEIMER, P. & LINK, M. H. 1991. *Seismic facies and sedimentary processes of submarine fans and turbidite systems,* New York, Springer-Verlag.

WU, L., THORSEN, R., OTTESEN, S., MENEGUOLO, R., HARTVEDT, K., RINGROSE, P. & NAZARIAN, B. 2021. Significance of fault seal in assessing CO2 storage capacity and containment risks–an example from the Horda Platform, northern North Sea. *Petroleum Geoscience,* 27**,** petgeo2020-102.

Appendix

Appendix 1

Appendix 1: This section contains a table with the observations for the 'Olive Grove' outcrop model, where names of the different units are marked on the overview image on this page. A high-resolution figure with the ability to zoom can be found within the following dropbox under filename 'OLIVE GROVE', additionally the outcrop to geomodel figure can be found under the filename 'Olive:_Grove_Overview' :

https://www.dropbox.com/scl/fo/5k4963jc16hvu8vv75eht/h?dl=0&rlkey=oc77qge2i3u5u00v8cdjtjr5y
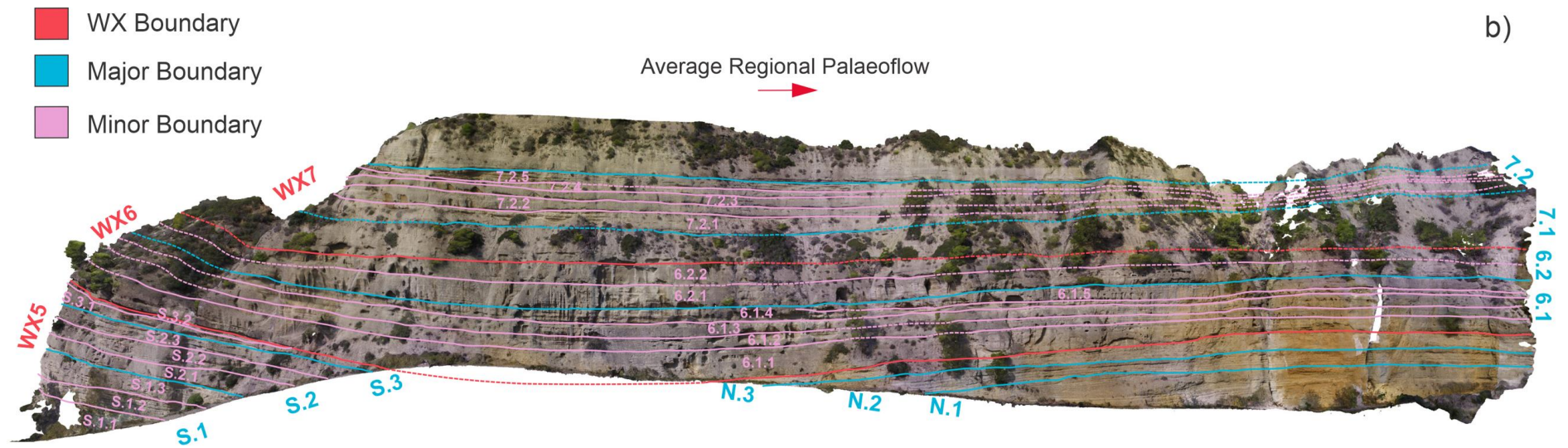
OLIVE GROVE OBSERVATIONS

WX5 - South

Boundary S.1 – Marks change in lithology: Unit S.1 has a higher proportion of thin mudstone intervals and is more stratified than unit S.2.

Unit S1 - Dips towards north and is mainly composed of massive and amalgamated conglomerates interbedded with mudstones. Bed thicknesses increases upwards.

Package name	Lithology	Dip and dip direction.	Bed geometries	Other comments
S.1.1	Massive coarse-grained sandstones and conglomerates interbedded with mudstones.	≈ 14° North	Broadly continuous layering, where some merges into each other. Typical bed thicknesses < 1m. Mudstone layers reaches 0,3 m in thickness.	Poor resolution due to vegetation, mud wash, and some "missing parts".
S.1.2	Amalgamated conglomerates interbedded with fine sandstones and mudstones.	≈ 11° North	Varying continuity of undulating bed-boundaries, merging into each other up-dip. Top layers are "erosionally truncated" by unit 1.3. Conglomerate bed thicknesses vary from 0,2 m to 1,5 m. Finer grained beds reaches 0,2 m in thickness.	Poor resolution due to vegetation, mud wash and some "missing parts".
S.1.3	Amalgamated conglomerates interbedded with fine sandstones and mudstones.	≈ 13° North	Undulating boundaries, merging into each other. Conglomerate bed thicknesses vary from 0,2 m to 2 m. Finer grained layers reaches up to 0,2 m in thickness.	Poor resolution in areas obscured by vegetation.

| **Boundary S.2** – Marks change in bed geometry: Beds in unit 2 have consistent thicknesses, while beds in unit 3 thins out towards north due to erosion. |

<table>
<tr><td colspan="5">Boundary S.2 – Marks change in bed geometry: Beds in unit 2 have consistent thicknesses, while beds in unit 3 thins out towards north due to erosion.

Unit S.2 – Dips towards north and mainly composed of amalgamated conglomerates. Layers are thinner and more stratified upwards.</td></tr>
<tr><td>Bed name</td><td>Lithology</td><td>Dip and dip direction.</td><td>Bed geometries</td><td>Other comments</td></tr>
<tr><td>S.2.1</td><td>Massive conglomerate.</td><td>≈ 13° North</td><td>No distinctive internal layering.

Bed thickness ≈ 3,5m</td><td></td></tr>
<tr><td>S.2.2</td><td>Massive conglomerate. Thinner conglomeratic layers in lower part of the unit, interbedded with mudstone.</td><td>≈ 12° North</td><td>Internal layers are broadly discontinuous and parallel. Unit becomes massive up-dip (southwards).

Typical conglomerate bed thicknesses are 1-2 m. Typical thickness of mudstone layers ≈ 0, 1 m.</td><td></td></tr>
<tr><td>S.2.3</td><td>Amalgamated conglomerates, interbedded with thin mudstone layers.</td><td>≈ 14,5° North</td><td>Internal layering is irregular and discontinuous. Unit becomes less stratified up-dip.

Typical conglomerate bed thicknesses are 0,5 - 1,5 m. Typical thickness of mudstone layers ≈ 0, 1 m.</td><td></td></tr>
</table>

Major Boundary				

Major Boundary WX5/ WX6 (South) – Erosive boundary marking a change in dip between Unit S (≈ 14° North) and Unit 3 (≈ 10° North).

Unit S.3 - Dips towards the North. The lower part is composed of conglomerates, and the upper part is more mudstone rich with thin-coarse grained beds.

Bed name	Lithology	Dip and dip direction.	Bed geometries	Other comments
S..3.1	Massive conglomerate thinning towards the North, interbedded with a few mudstone layers.	≈ 13° North	Displays little internal layering. Becomes massive up-dip. Unit is eroded towards the North by Unit WX6. Bed thickness ≈ 5,0 m in south and ≈ 1,0 m in north. Mudstones ≈ 0,1 m thick.	
S.3.2	Mudstone rich unit, with thin coarse-sandstone and gravelly layers.	≈ 14° North	Internal layering are discontinuous and parallel. Eroded towards North by Unit WX6. Typical bed thicknesses are < 0,5 m.	

Major Boundary WX5/ WX6 (North) - Erosive boundary marking a major change in lithology and bed geometries: Unit N has a higher proportion of mudstone beds and internal layering than Unit WX6.

Unit N - Dips gently towards the South and is mainly composed of alternating layers of conglomerates and mudstones. Beds become finer grained upwards (increase in mud content).

Bed name	Lithology	Dip and dip direction.	Bed geometries	Other comments
N.1	Alternating layers of conglomerates and mudstones. Mudclasts are present within some conglomerates.	≈ 7° South Dip becomes a bit steeper towards the south.	Lens-shaped conglomerates, with both pinch and swell, and pinch out geometries. Layers become more parallel towards the North. The thicknesses of conglomerates ranges from 0,1 m to 2,0 m. Mudstone layers are 0,1 m to 0,4 m.	Some normal faulted layers. Southern fault– offset is ≈ 0,5 m. Northern fault – offset is ≈ 0,6 m.
N.2	Alternating layers of conglomerates and mudstones	≈ 4° South	Lens-shaped conglomerates with both pinch and swell and pinch out geometries. Layers become more parallel towards the North. Typical conglomerate bed thicknesses ≈ 0,5 m. Mudstones thicknesses ≈ 0,3 m.	
N.3	Mud-rich unit with thin layers of coarse-grained sandstones and gravelly layers.	≈ 5° South	Bed continuities are highly variable. Typical bed thicknesses are < 1 m.	Some thrust faulted layers. Offset ≈ 1,0 m

WX6

Boundary 6.1 –Marks change in lithology and bed geometries: Unit 6.2 consists of thicker and more continuous massive conglomerate beds becoming more sandstone or mudstone rich towards the North.

Unit 6.1 – Massive conglomerates becoming more sandstone-rich towards the North.

Bed name	Lithology	Dip and dip direction.	Bed geometries	Other comments
6.1.1	South: Massive conglomerate North: Alternating layers of conglomerates and sandstones. Mudstone layers are sporadically present within the unit.	Broadly horizontal. The southernmost part has a dip of ≈ 10° towards the North	Massive conglomerates in the south are amalgamated with crude boundaries. Thickness of the massive conglomerate package is ≈ 5,5 m. Alternating conglomerates and sandstones are broadly parallel, with a few dipping layers towards the South. Typical bed thicknesses < 1,0 m.	Poor resolution towards the South due to vegetation.
6.1.2	South: Massive conglomerate North: Alternating layers of conglomerates and sandstones. Some discontinuous thin (<0,5 m) mudstone layers are present in the unit.	Broadly horizontal. The southernmost part has a dip of ≈ 10° towards the North	Massive conglomerates in the south are amalgamated with crude boundaries. Thickness of the massive conglomerate package is ≈ 3,0 m. Boundaries of alternating conglomerates and sandstones are merging into each-other both up- and down-dip- Typical bed thicknesses are< 1,0 m.	Poor resolution towards the South due to vegetation.

6.1.3	South: Massive conglomerate North: Amalgamated conglomerates with sandstone in upper part Some discontinuous thin (<0,5 m) mudstone layers are present in the unit.	Broadly horizontal. The southernmost part has a dip of ≈ 10° towards the North	Massive conglomerates in the south are amalgamated with crude boundaries. Thickness of the massive conglomerate package is ≈ 4,0 m. Conglomerate layers display little internal layering. Upper sandstone package follows underlying stratigraphy. Typical bed thicknesses are 0,5 m to 2 m.	Poor resolution towards the South due to vegetation.
6.1.4	South: Massive conglomerate North: Alternating layers of mudstones and conglomerates. Mainly sandstone dominated.	Broadly horizontal. The southernmost part has a dip of ≈ 10° towards the North	Massive conglomerates in the south are amalgamated with crude boundaries. Massive conglomerate thickness ≈ 1,0 m. Alternating layers of sandstones and conglomerates have typical bed thicknesses of < 1 m.	Poor resolution towards the South due to vegetation.
6.1.5	Amalgamated conglomerates, partly interbedded by finer-grained layers.	Broadly horizontal.	Unit is only present in the northern part of the outcrop. Typical bed thicknesses < 1,0 m.	

Boundary WX6/WX7 – Marks change in lithology and bed geometries: Unit WX6 are more sand-rich and exposes less internal erosive boundaries than Unit WX7.

Unit 6.2 – Broadly horizontal unit with a dip towards north in southernmost part, with beds of massive conglomerates and pebbly sandstones, becoming more mudstone rich towards north.

Bed name	Lithology	Dip and dip direction.	Bed geometries	Other comments
6.2.1	Massive conglomerate becoming sandstone dominated towards the north.	Broadly horizontal. The southernmost part has a dip of $\approx 10°$ towards the North	Conglomerates have internal crude boundaries. Thickness of package is $\approx 5,5$ m.	Poor resolution and highly vegetated towards the North.
6.2.2	Massive conglomerate unit becoming mudstone dominated towards the north.	Broadly horizontal	Conglomerates in south have parallel layering with crude boundaries. Thickness of package is $\approx 6,0$ m.	Poor resolution and highly vegetated towards north.

WX7

Boundary 7.1 – Marks change in lithology and bed geometries: Unit 7.2 is more stratified than Unit 7.1

Unit 7.1 – Broadly horizontal unit, composed of massive conglomerates becoming mudstone dominated towards the North.

Bed name	Lithology	Dip and dip direction.	Bed geometries	Other comments
7.1	Massive conglomerate becoming mudstone rich towards the North.	$\approx$ Horizontal	Display little internal layering. Thickness of package is $\approx 10,0$ m.	Unit is highly obscured by vegetation.

Boundary 7.2 – Marks the upper limit of interpretations.				

Boundary 7.2 – Marks the upper limit of interpretations.

Unit 7.2– Broadly horizontal unit, composed of sheet-like conglomerates with mudstone caps on top. All layers become mudstone dominated towards the North.

Bed name	Lithology	Dip and dip direction.	Bed geometries	Other comments
7.2.1	Amalgamated conglomerates and coarse-grained sandstones interbedded with mudstone layers.	≈ Horizontal	Beds display little internal layering. Mud-caps follow underlying stratigraphy. Typical bed thicknesses ≈ 1,0 m.	Unit is highly obscured by vegetation towards the North, and stratification in this part is uncertain.
7.2.2	Massive, sheet-like conglomerate, with laterally discontinuous (≈ 1,5 m), thin (< 0,5 m), mud-caps on top.	≈ Horizontal	Unit has an erosive boundary. Mud-caps follow underlying stratigraphy. Thickness of package ≈ 2,0 m.	Unit is highly obscured by vegetation towards the North, and stratification in this part is uncertain.
7.2.3	Massive, sheet-like conglomerate, with laterally discontinuous (≈ 1,0 m), thin (< 0,5 m), mud-caps on top.	≈ Horizontal	Unit has an erosive boundary. Mud-caps follow underlying stratigraphy. Thickness of package ≈ 2,0 m.	Unit is highly obscured by vegetation towards the North, and stratification in this part is uncertain.
7.2.4	Massive, sheet-like conglomerate.	≈ Horizontal	Unit has an erosive boundary. Mud-caps follow underlying stratigraphy. Thickness of package ≈ 1,5 m.	Unit is highly obscured by vegetation towards the North, and stratification in this part is uncertain.

7.2.5	Massive, sheet-like and amalgamated conglomerates, with laterally discontinuous (≈ 1,5 m), thin (< 0,5 m), mud-caps on top.	≈ Horizontal	Unit has an erosive boundary. Typical bed thicknesses = 1,0 m	Unit is highly obscured by vegetation towards the North, and stratification in this part is uncertain.

Appendix 2

Appendix 2: This section contains a table with the observations for the 'Stomio' outcrop model, where names of the different units are marked on the overview image on this page. A high-resolution figure with the ability to zoom can be found within the following dropbox under filename 'STOMIO' additionally the outcrop to geomodel figure can be found under the filename 'Stomio_Overview' :

https://www.dropbox.com/scl/fo/5k4963jc16hvu8vv75eht/h?dl=0&rlkey=oc77qge2i3u5u00v8cdjtjr5y
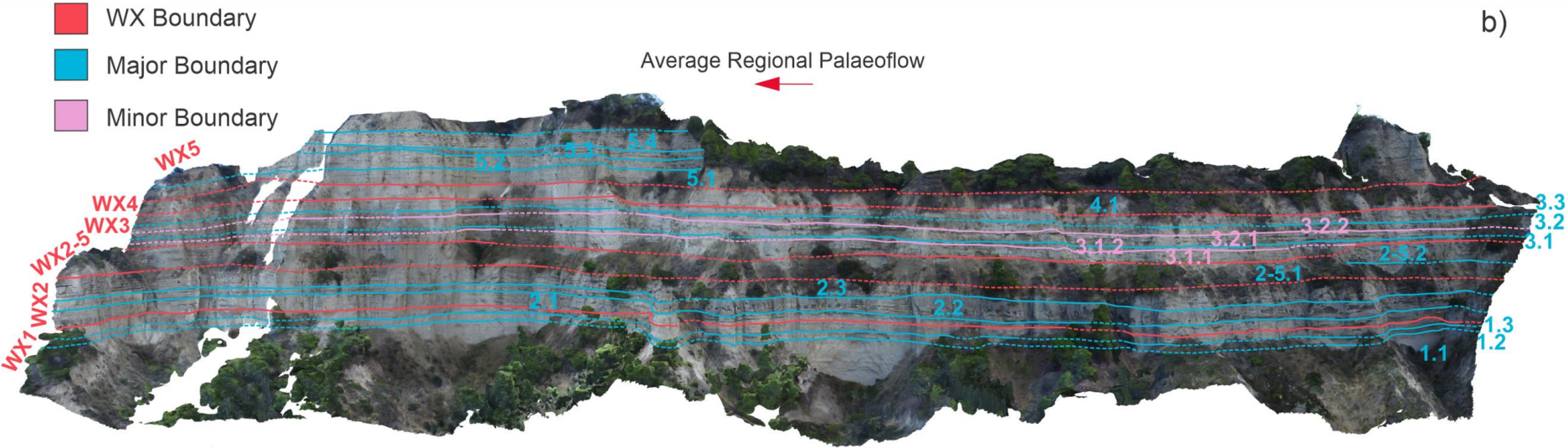
STOMIO OBSERVATIONS
WX1

Boundary WX1/ WX2 – Boundary marks change in lithology. Unit WX1 is a highly mudstone dominated unit, whilst Unit WX2 is a heterolithic unit composed of mudstones, sandstones and conglomerates.
Unit WX1 – Mudstone dominated unit, with conglomerate layers on top (WX2 1.2-3). Conglomeratic packages become more mud-rich towards the south. Large parts of the unit are covered by vegetation.

Package name	Lithology	Dip, dip direction and bed thicknesses	Bed geometries	Other comments
1.1	Mudstone	Dip: Horizontal Mudstone package is ≈ 15 m.	Broadly discontinuous parallel layering.	Package is highly obscured by vegetation and mud-wash.
1.2	Coarse-sandstones interbedded with mudstones. Becomes more mud-rich northwards.	Dip: Horizontal Typical bed thicknesses ≈ 1,0 m	Broadly discontinuous, parallel layering.	Some areas are obscured by vegetation and mud-wash.
1.3	Amalgamated conglomerates interbedded with mudstones. Becomes more mud-rich northwards.	Dip: Horizontal Bed thicknesses vary from 0,2 m to 3,0 m.	Broadly discontinuous, planar, non-parallel. Amalgamation occurs both north- and southwards.	Some areas are obscured by vegetation and mud-wash.

WX2

Boundary WX2/ WX2-5 – Boundary marks change in lithology. Unit WX2 is coarser-grained than Unit WX2-5.
Unit WX2 – Composed of conglomerates, sandstones, and mudstones. Mainly sandstones in the upper and lower part (WX2.1 and WX2.3) and thicker conglomeratic layers in the mid part (WX2.2)

Package name	Lithology	Dip, dip direction and bed thicknesses	Bed geometries	Other comments
2.1	Amalgamated sandstones, interbedded with mudstones.	Dip: Horizontal Typical bed thicknesses 0,2/ 0,5 m to 1,5 m.	Irregular, discontinuous boundaries. Amalgamation mainly occurs southwards.	
2.2	Massive conglomerate layers in the upper and lower part. Heterolithic layers of gravelly sandstones and mudstones in between the massive conglomerates.	Dip: Horizontal Upper and lower conglomerate bed thicknesses vary from 0,5 m to 5,0 m. Typical bed thicknesses for thinner layers < 1 m.	Irregular, both continuous and discontinuous boundaries. Some amalgamation of conglomerates southwards.	
2.3	Amalgamated sandstones and conglomerates, interbedded with mudstones.	Dip: Broadly horizontal. Laterally variable bed thicknesses, from 0,2 m to 2,5 m.	Irregular, discontinuous layering	Partly covered by vegetation.

WX2-5

Boundary WX2-5/ WX3 – Boundary marks a change in lithology. Unit WX2-5 is more mudstone dominated than Unit WX3.				
Unit WX2-5 – Mudstone dominated unit, with deformed mudstone and sandstone package in the southern part. Large parts of the unit are covered by vegetation.				
Package name	**Lithology**	**Dip, dip direction and bed thicknesses**	**Bed geometries**	**Other comments**
2-5.1	Mudstone	Dip: Horizontal The package is ≈ 10 m.		The package is highly obscured by vegetation.
2-5.2	Mudstones and sandstones.	Thickness of package with deformed layering ≈ 5 m. Typical bed thicknesses of convex up layering ≈ 0,5 m.	In the northern part layers are chaotic with little internal layering due to deformation. In the southern part layers are convex up.	The package is only present in the southernmost 55 m of the outcrop.

WX3

	Boundary WX3/ WX4 – Marks change in lithology. Unit WX3 is coarser grained than Unit WX4. **Unit WX3** – Complex mix of conglomerates, sandstones, and mudstones. Some layers are normal faulted, with an offset ≈ 1,0m. The thicknesses of layers are laterally variable.			
Package name	**Lithology**	**Dip, dip direction and bed thicknesses**	**Bed geometries**	**Other comments**
3.1.1	Sandstones and mudstones	Dip: Horizontal Typical bed thickness < 1,5 m. Bed thicknesses vary laterally.	Both laterally extensive beds and irregular, discontinuous, amalgamated beds.	Some areas are obscured by vegetation.
3.1.2	Sandstones and mudstones. Few conglomerates.	Dip: Horizontal Thickness of the package is ≈ 1 m.	Both laterally extensive beds and irregular, discontinuous, amalgamated beds.	
3.2.1	Amalgamated sandstones interbedded with mudstones.	Dip: Horizontal The thicknesses of conglomerates are typically 0,5 m to 1,0 m. Interbedded sandstones and mudstones typically < 0,5 m.	Both laterally extensive beds and irregular, discontinuous, amalgamated beds.	
3.2.2	Sandstones interbedded with mudstones. Mass-transport deposits.	Dip: Horizontal Sandstone thicknesses typically < 1 m.	Both laterally extensive beds and irregular, discontinuous, amalgamated beds.	

		Mudstones thicknesses typically < 0,5 m.		
3.3	Massive conglomerates and sandstones interbedded with mudstones.

Some conglomerates pinch out towards the east | Dip: Horizontal

Thicknesses of conglomerates vary laterally, typically 0,5 m to 1,0 m.

Thicknesses of sandstones and mudstones typically < 0,5 m. | Both laterally extensive beds and irregular, discontinuous, amalgamated beds. | |

WX4

Boundary WX4/ WX5 – Boundary marks a change in lithology. Unit WX4 is more mudstone dominated than Unit WX5.
Unit WX4 – Mudstone dominated unit.

Package name	Lithology	Dip, dip direction and bed thicknesses	Bed geometries	Other comments
4.1	Mudstone	Dip: Horizontal

The package is ≈ 10 m. | | The package is highly obscured by vegetation. |

WX5

<table>
<tr><td colspan="5"><u>Top Boundary</u> – Boundary marks the upper limit of interpretations.
<u>Unit WX5</u> – Composed of conglomerates, sandstones, and mudstones. Layers are normal faulted in the southern part, with an offset ≈ 2,0 m. Unit is only present in the northernmost 240 m of the outcrop.</td></tr>
<tr><td>Package name</td><td>Lithology</td><td>Dip and dip direction.</td><td>Bed geometries</td><td>Other comments</td></tr>
<tr><td>5.1</td><td>Mudstones with thin sandstone layers.</td><td>Dip: Horizontal

Mudstone thicknesses typically 1,0 m to 2,0 m. Sandstone thicknesses typically ≈ 0,5 m.</td><td>Both laterally extensive, and irregular, discontinuous boundaries</td><td></td></tr>
<tr><td>5.2</td><td>Conglomerates, sandstones, and mudstones.</td><td>Dip: Horizontal

Bed thicknesses vary a lot from 0,2 m to 2,5 m.</td><td>Both laterally extensive, and irregular, discontinuous boundaries</td><td></td></tr>
<tr><td>5.3</td><td>Amalgamated conglomerates interbedded with mudstones.</td><td>Dip: Horizontal

Typical thicknesses of conglomerates 1,0 m to 4,0 m. Typical thicknesses of interbedded layers are ≈ 0,5.</td><td>Laterally extensive, amalgamated conglomerates. Amalgamation occurs eastwards.</td><td></td></tr>
<tr><td>5.4</td><td>Heterolithic beds of conglomerates, sandstones, and mudstones.</td><td>Dip: Horizontal

Highly variable bed thicknesses. Broadly 0,5 m to 1,0 m.</td><td>Both laterally extensive, and irregular, discontinuous boundaries</td><td></td></tr>
</table>

Appendix 3

Appendix 3: This section contains both field- and pseudologs made for the 'Olive Grove' outcrop model. High-resolution figure with the ability to zoom can be found within the following dropbox and the filenames of the particular logs are listed beside them on the following pages:

https://www.dropbox.com/scl/fo/5k4963jc16hvu8vv75eht/h?dl=0&rlkey=oc77qge2i3u5u00v8cdjtjr5y

Filename: OG-A

Filename: OGA-PL

Pseudolog OG-A

LEGEND

Lithotypes
- Mudstone
- Sandstone
- Conglomerate
- Mass Transport Deposit

62.0

61.0 — Massive conglomerate. Highly vegetated and poor outcrop conditions

60.0

59.0

58.0

57.0

56.0

55.0

54.0

53.0 — WX6

52.0

51.0

50.0

49.0 — Massive conglomerate

48.0

47.0 — WX6.1.1

— Vegetated in top

46.0 — Massive conglomerate. Some internal layers with more consolidated clasts.

45.0 — 6.1

44.0 — Massive conglomerate

43.0 — 6.1.3

42.0

41.0 — Massive conglomerate. Some internal layers with more consolidated clasts.

40.0

39.0 — 6.1.2

38.0

37.0 — Massive conglomerate. Some internal layers with more consolidated clasts.

36.0 — 6.1.1

35.0

34.0 — Massive conglomerate. Some internal layers with more consolidated clasts.

33.0

32.0

31.0 — WX5 — Erosive base.

30.0 — WX5.1.1 — Thin gravelly layers interbedded with mudstones

29.0

28.0 — Stacked and amalgamated conglomerates interbedded with mudstones.

27.0 — 5.2

26.0

25.0

24.0

23.0

22.0 — 5.2.2 — Thin conglomerate layers following the underlying stratigraphy, interbedded with mudstones.

21.0

20.0 — Massive conglomerate

19.0

18.0 — 5.2.1

17.0

16.0

15.0 — Stacked and amalgamated conglomerates interbedded with thin mudstone layers

14.0 — 5.1 — Conglomerates are both matrix supported and clast supported with various grain sizes.

13.0

12.0

11.0

10.0

9.0

8.0

7.0

6.0

5.0

4.0

3.0

2.0

1.0

0.0

120

Filename: OG-B

Scale: 1:10
Height (m)

OG-B

LEGEND

Lithologies

Mudstone
Sandstone
Conglomerate

Sedimentary Features

Current ripples
Climbing ripples
Intraclasts
Imbrication

Matrix supported with pebblee to cobble sized clasts.
Mudwash.

Matrix supported with pebble to cobble sized clasts.
Mudwash.

Some gravel to pebble sized clasts.
Mudwash

Some gravel to pebble sized clasts in layer.

Gravelly layer with pebble sized clasts.

Low angle fabric.

Low angle fabric.

Low angle fabric.

Matrix supported with pebble to cobble sized clasts.

Low angle fabric.

Matrix supported with pebble to cobble sized clasts.

Mudwash

clay silt vf f m c vc Gravel Pebbles Cobbles Boulders
Sand

121

Filename: OGB-PL

Scale: 1:50
Height (m)

Pseudolog OG-B

LEGEND
Lithologies
Mudstone
Sandstone
Conglomerates
Mass-Transport Deposit

7.2

46.0

45.0   Amalgamated
             conglomerates with erosive
             boundaries and mudstone
             caps on top.

44.0   7.2.4

43.0

42.0

41.0

40.0   7.2.3

39.0

38.0

37.0   7.2.2

36.0   Heterogeneous layers of
             gravelly sandstones and
             laminated mudstones.

35.0

34.0   7.2.1

33.0

32.0

31.0

30.0   Massive conglomerate.

29.0   Vegetated layer

28.0

27.0

26.0

25.0   Massive conglomerate.

24.0

23.0   7.1

22.0

21.0   Massive conglomerate.

20.0

19.0   WX6

18.0

17.0   Massive conglomerate.
             Some internal layers
             with more concentrated
16.0   clasts.

15.0   6.2.1

14.0   Few larger clasts in the
             middle of the layer

             Amalgamated
13.0   conglomerates.

12.0

11.0   6.1

10.0   Amalgamated
             conglomerates.

9.0

8.0   6.1.3

7.0

6.0   Amalgamated
             conglomerates.

5.0   6.1.2

4.0   Amalgamated
             conglomerates.
                                        6.1.1
3.0

2.0

1.0

0.0

Clay Silt   Sand   Gravel Pebbles Cobbles Boulders

Filename: OG-C

Scale: 1:10
Height (m)

OG-C

LEGEND

Lithologies

Mudstone
Sandstone
Conglomerate

Sedimentary Features

Current ripples
Climbing ripples
Intraclasts
Imbrication

Gravelly layer with pebble sized clasts.

Matrix supported layer with pebble to cobble sized clasts.
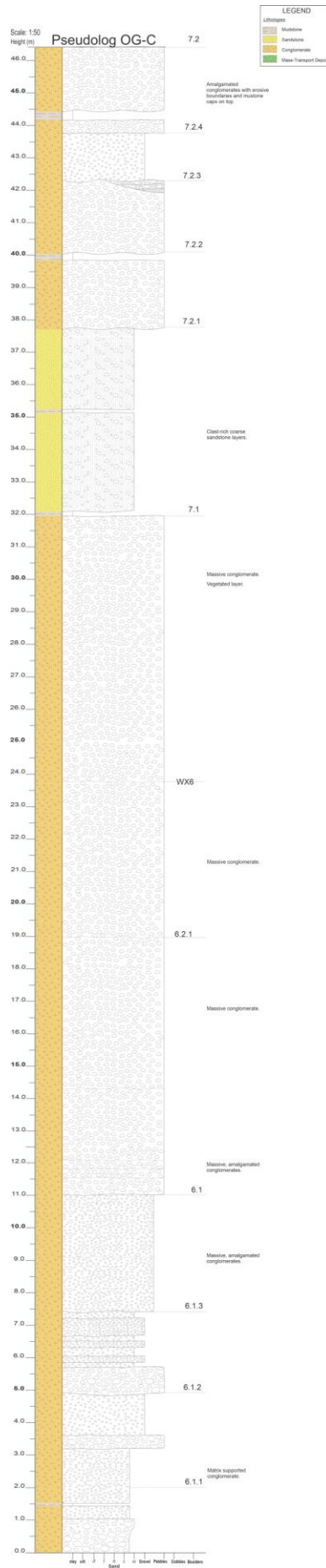
0-1 m: Poor outcrop conditions due to mud-wash.

Gravelly layer
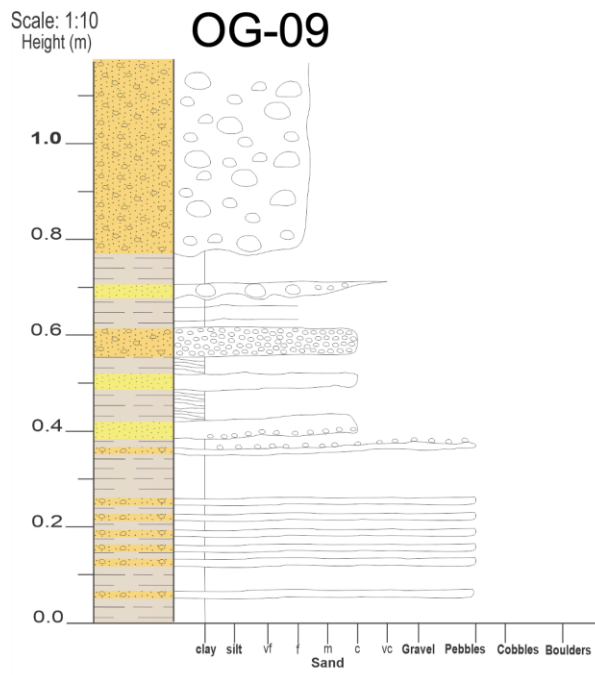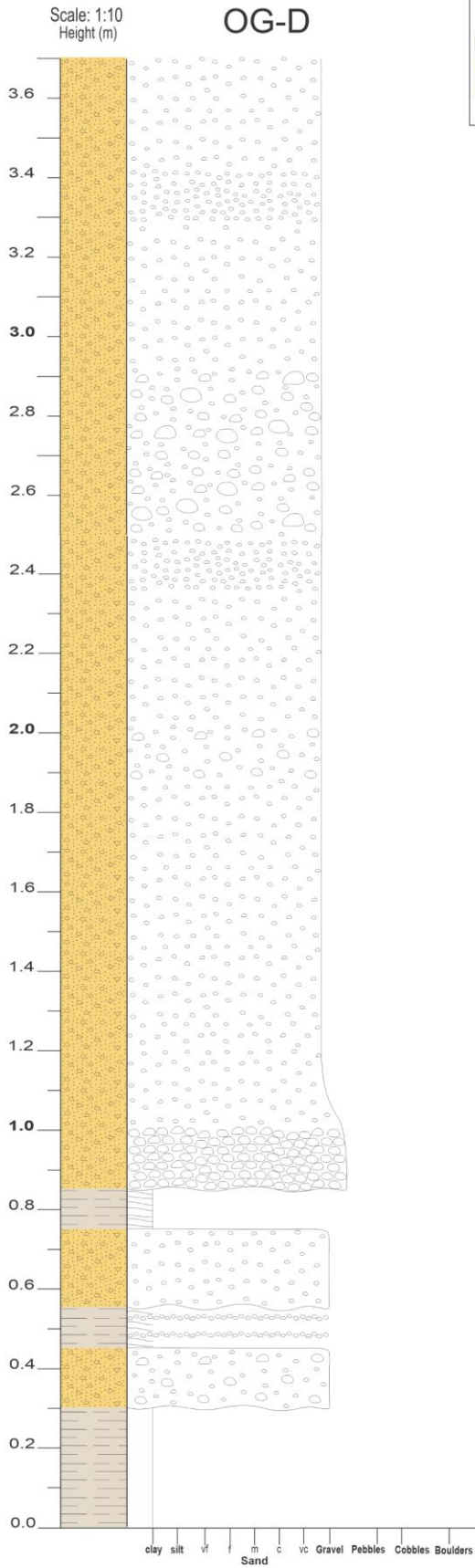
Layer becomes more gravelly at top.

Matrix supported layer with pebble to cobble sized clasts.

clay silt vf f m c vc Gravel Pebbles Cobbles Boulders
Sand

Pseudolog OG-C

Scale: 1:50
Height (m)

Scale: 1:10
Height (m)

OG-09

Cobble and large pebble grade conglomerate with coarse sand matrix. Largely matrix supported at base but poorly exposed. Too thick to log enitrely/ goes off section.

Thrust faults.
Shallowing angle upwards with partly ramp-flat ramp geometry.

LEGEND

Lithologies

Mudstone
Sandstone
Conglomerate

Sedimentary Features

Current ripples
Climbing ripples
Intraclasts
Imbrication

clay silt vf f m c vc Gravel Pebbles Cobbles Boulders
Sand

Filename: OG-D

Scale: 1:10
Height (m)

OG-D

LEGEND

Lithologies

Mudstone
Sandstone
Conglomerate

Sedimentary Features

Current ripples
Climbing ripples
Intraclasts
Imbrication

Layer with higher amount of gravel to small-pebble sized clasts.

Pebble to cobble sized clasts. Matrix supported.

Layer with higher amount of gravel to small-pebble sized clasts.

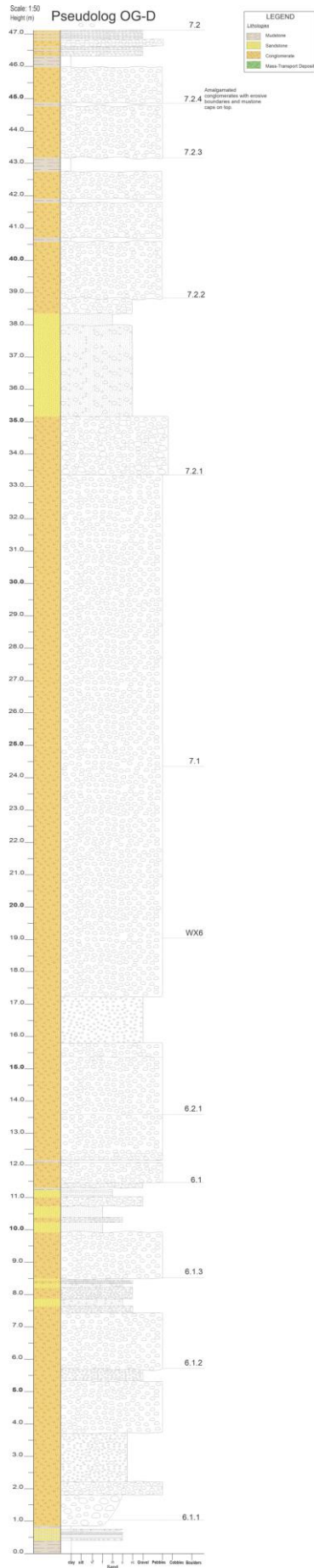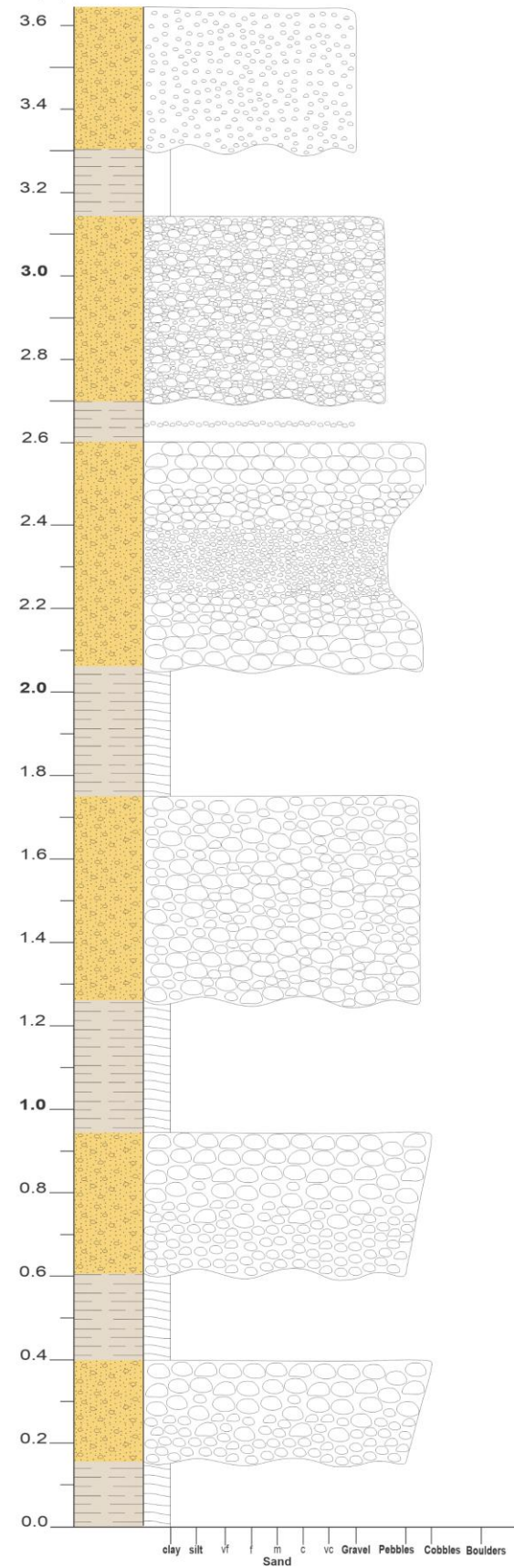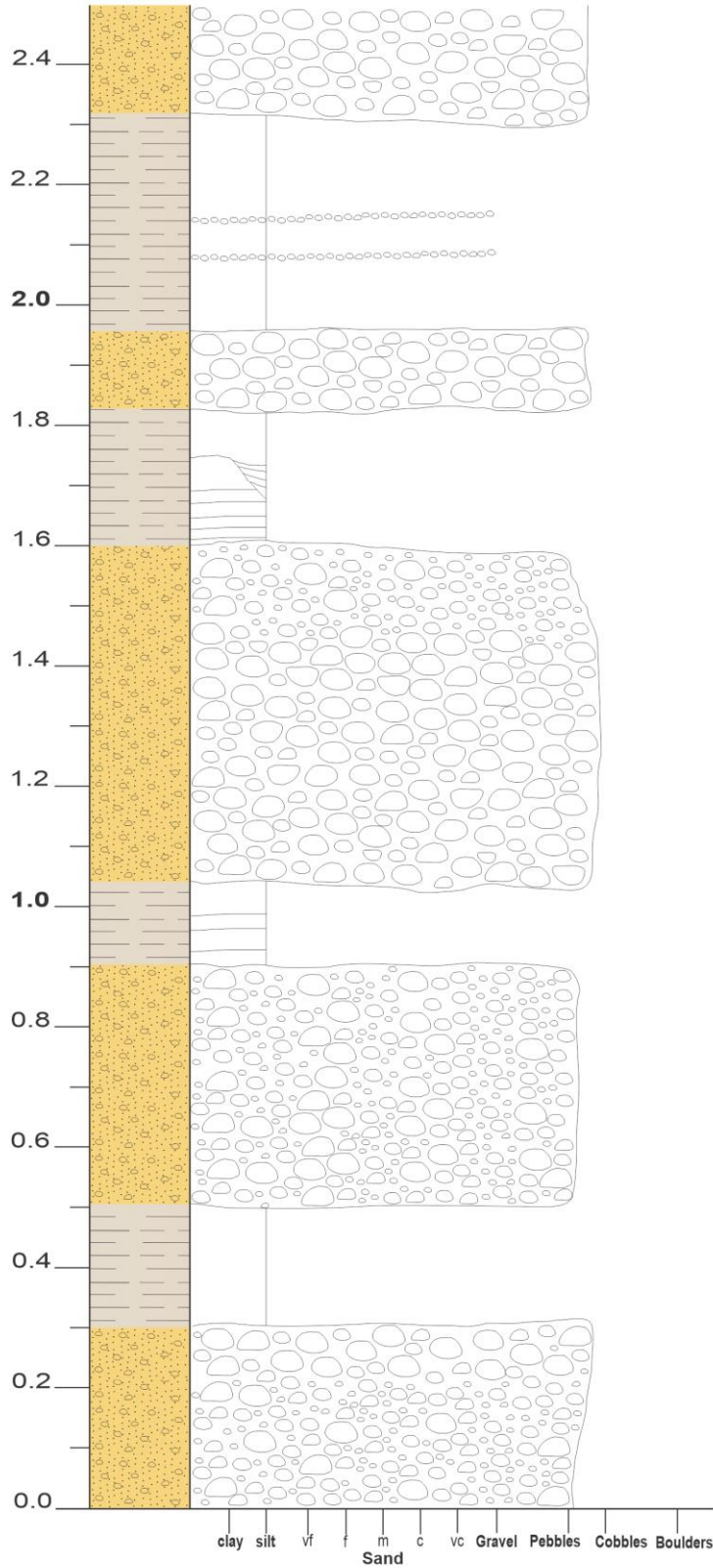Layer with pebble to cobble sized clasts.

Poor outcrop conditions due to mud-wash.

Larger clasts at base, broadly pebble sized.

Gravelly layer

Gravelly layer. Some pebble sized clasts.

Layer with higher amount of

clay silt vf f m c vc Gravel Pebbles Cobbles Boulders
Sand

Filename: OGD_09-PL

Scale: 1:10
Height (m)

OG-E

Gravelly layer.

Clast supported
No grain size trend.

Clast supported.
Normal grading in lower
part, and inverse grading
in upper part.

Clast supported
No grain size trend.

Clast supported
Inverse grading.

Clast supported
Inverse grading.

LEGEND

Lithologies

Mudstone

Sandstone

Conglomerate

Sedimentary Features

Current ripples

Climbing ripples

Intraclasts

Imbrication

clay silt vf f m c vc Gravel Pebbles Cobbles Boulders
Sand
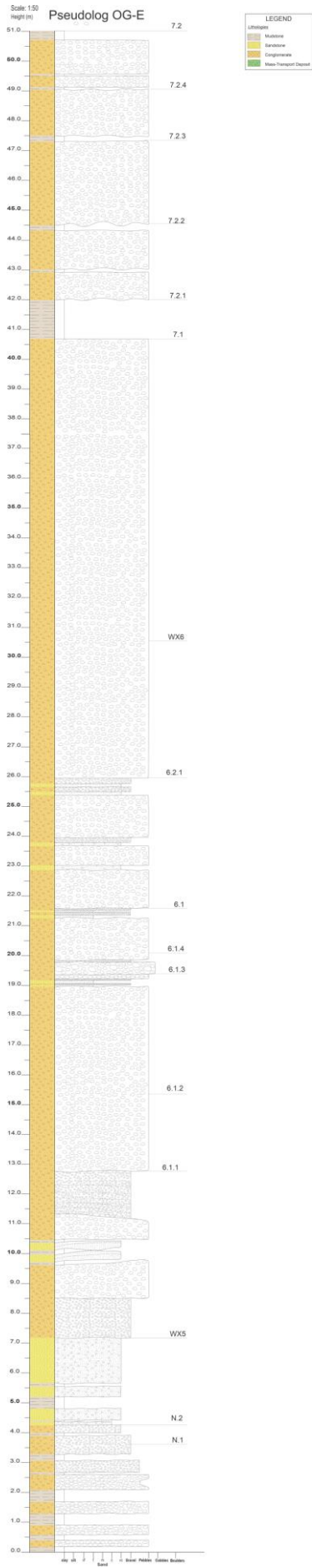
Filename: OGE_PL

Filename: OG-10

Scale: 1:10
Height (m)

OG-10

LEGEND

Lithologies

Mudstone
Sandstone
Conglomerate

Sedimentary Features

Current ripples
Climbing ripples
Intraclasts
Imbrication

Clast supported conglomerate,
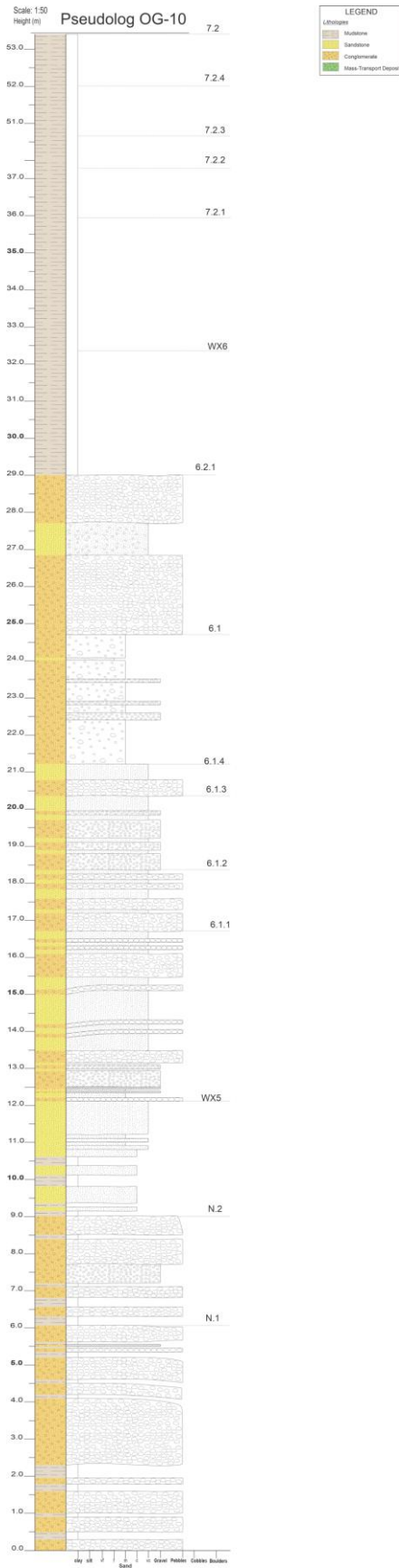with medium-large pebbles.
No alignment or fabric.

Fewer large pebbles at top.

Clast supported.

Variable clast support and
chaotic.
Small-large pebbles and no
real grainsize trend.
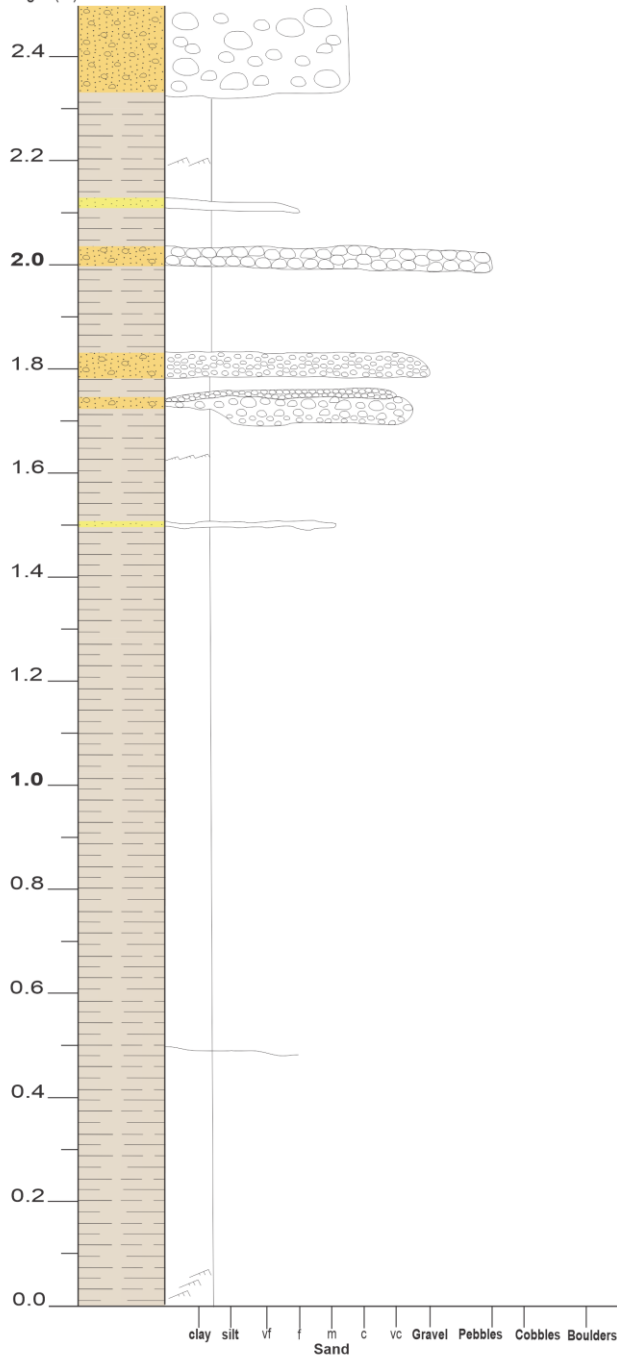
Thins and thickens with
underlying topography.

clay silt vf f m c vc Gravel Pebbles Cobbles Boulders
Sand

130

Filename: OG10-PL

Scale: 1:50
Height (m)

Pseudolog OG-10

7.2
7.2.4
7.2.3
7.2.2
7.2.1

WX6

6.2.1

6.1
6.1.4
6.1.3
6.1.2
6.1.1

WX5

N.2

N.1

LEGEND
Lithologies
Mudstone
Sandstone
Conglomerate
Mass-Transport Deposit

Filename: OG-04

Scale: 1:10
Height (m)

OG-04

Matrix supported, very thick conglomerate (goes off section too high to completely log). Pebble to cobble sized intraclasts (rounded - subrounded).

Upper part: clast supported. Matrix is polydisperse and compises silt-very coarse sand.

Lower part: matrix supported with upward increase in clast size.

Aggradational climbing ripples

Inter-laminated clays and silts in pale grey marlstones with occasionally silt and vfs stringers

Climbing ripples - some partly fluidised

clay silt vf f m c vc Gravel Pebbles Cobbles Boulders
Sand

LEGEND

Lithologies   Sedimentary Features

Mudstone   Current ripples

Sandstone   Climbing ripples

Conglomerate   Intraclasts
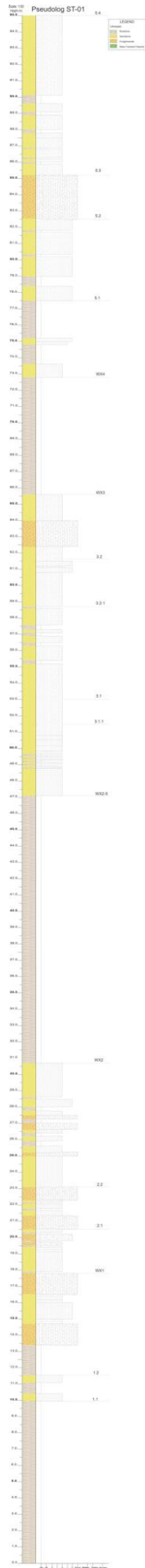
                           Imbrication

Filename: OG4-PL
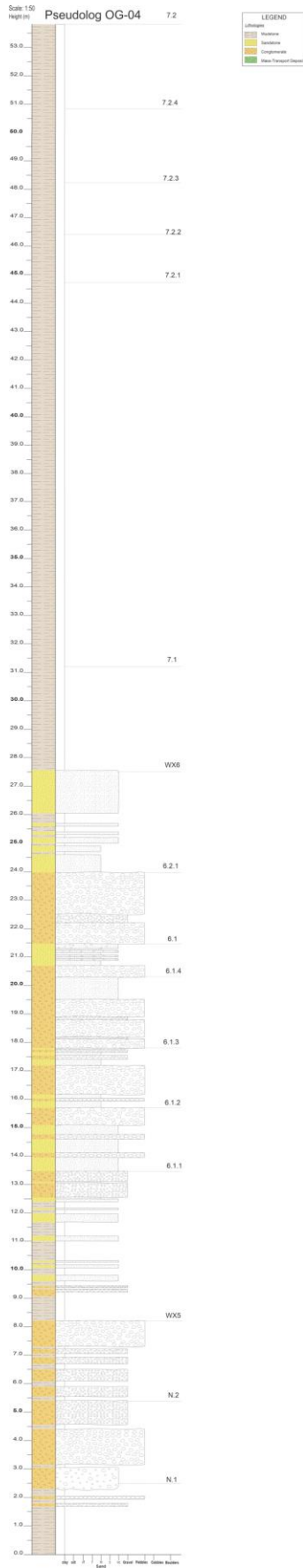
Appendix 4

Appendix 3: This section contains the pseudologs made for the 'Stomio' outcrop model. High-resolution figure with the ability to zoom can be found within the following dropbox and the filenames of the particular logs are listed beside them on the following pages:
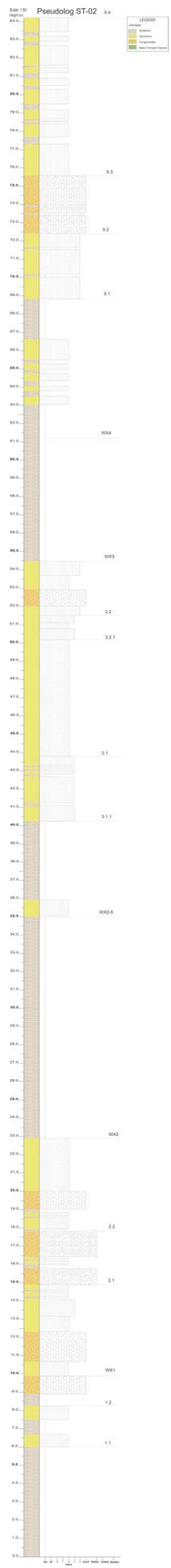
https://www.dropbox.com/scl/fo/5k4963jc16hvu8vv75eht/h?dl=0&rlkey=oc77qge2i3u5u00v8cdjtjr5y
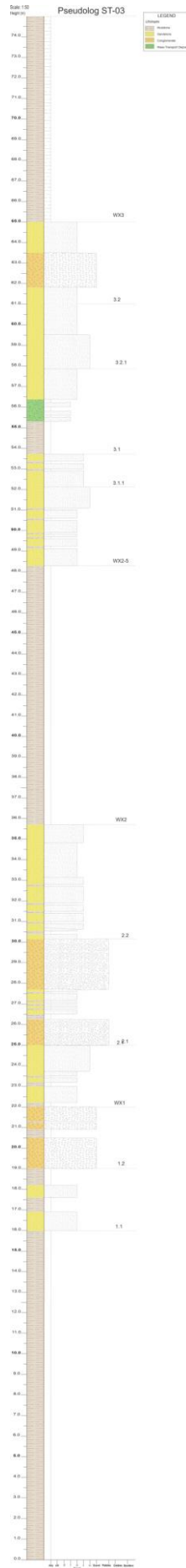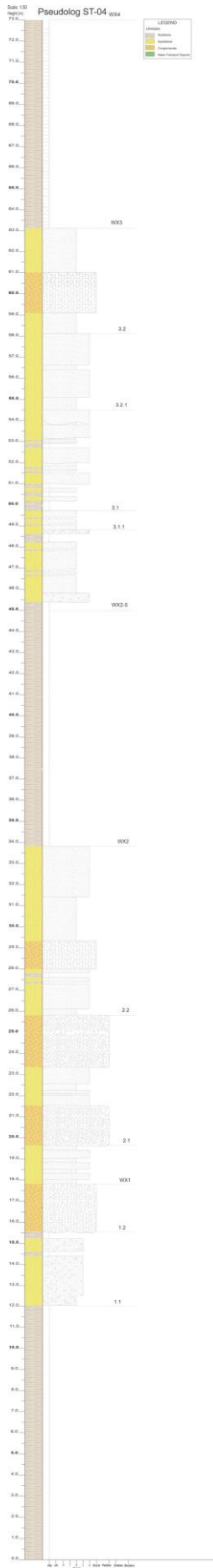
Filename: ST01

Pseudolog ST-01

Filename: ST02

Filename: ST03

Pseudolog ST-03

Filename: ST04

Filename: ST05

Pseudolog ST-05